Hardin, R.A., and Beckermann, C., "Prediction of Fatigue Life of Cast Steel in the Presence of Porosity," in Proceedings of the 61st SFSA Technical and Operating Conference, Paper No. 5.8, Steel Founders' Society of America, Chicago, IL, 2007.

Prediction of Fatigue Life of Cast Steel in the Presence of Porosity

Richard A. Hardin and Christoph Beckermann

Department of Mechanical and Industrial Engineering
The University of Iowa, Iowa City, IA 52242

Abstract

A methodology to simulate the fatigue life of cast steel with porosity using existing commercial software has been developed and validated through comparison with measurements. X-ray tomography is used to reconstruct the porosity distribution in test specimens so that its effects can be accurately simulated. The porosity is incorporated into finite element analysis (ABAQUS) to determine the complex stress field resulting from the porosity distribution where elastic mechanical properties are dependent on the locally varying porosity. Then a multi-axial strain-life analysis is performed using the durability simulation software *fe-safe* to determine the fatigue life. The fatigue modeling approach is incorporated within the constraints of using the commercial software, and it uses an adaptive subgrid technique to improve the model's ability to predict the detrimental effects of porosity which a coarse computational grid cannot resolve. The model has been verified by comparing the predicted results to measured fatigue life for specimens with average porosity ranging from 8% to 22%. Measured and predicted fatigue lives for nearly all 25 test specimens were found to fall within one decade; three were only slightly outside this range. This is taken in fatigue predictions as very good agreement. The fatigue life prediction method is then applied to an example case study part, and the reader is led through an entire integrated part performance analysis process, from casting through to fatigue life prediction.

I. INTRODUCTION

This work extends the method of modeling the effects of porosity on steel stiffness and stress redistribution presented at last year's Technical and Operating Conference [1] to the prediction of fatigue life in steel containing porosity. Existing commercial software is used for stress analysis and fatigue life prediction to give part designers a new approach to design castings with greater certainty in their performance. Since inhomogeneities in cast metal due to porosity or inclusions are not considered currently in part design, ad-hoc safety factors are currently used to address a designer's uncertainty in how the casting will perform. These safety factors are based on the assumption that castings perform unpredictably, if not poorly. Applying such safety factors to the entire cast material might do little for the robustness of the design other than increasing casting weight. Many part designers become frustrated by castings designed with very large safety factors that fail in service, and are hesitant to use castings. Such frustrations could be avoided if the quality of the cast metal throughout the casting could be know ahead of time and incorporated into the design.

In the approach presented here local variations in the cast steel properties are considered in the design. The resulting part design will be conservative and safe by assuring that the best

possible quality of metal in the casting process is produced at highly stressed hot-spots. Should unavoidable inclusions and porosity form, the casting process must be designed so that they will not effect the overall part performance. Furthermore, if designers wish to use lighter-weight and thinner-sectioned steel castings, predicting if and where microporosity forms and its effect on strength and fatigue behavior will be critical to produce designs that are tolerant of its presence. An integrated design process is emerging [2] where casting process modeling that predicts the location, amount, and size characteristics of micro- and macro- porosity allows designers to simulate the possible effects of casting production processing on part service performance. It is anticipated that such a design process will help guide and improve inspection criteria in the future by linking it with expected performance.

There has been considerable and increasing interest in developing the engineering knowledgebase of the effects of porosity on casting performance in recent years for a wide range of metals [3-15]. Also, there has been a considerable body of work done on the effect of inclusions on metal fatigue, which is well summarized in the book by Murakami [16]. In our 2003 T&O paper [17] a thorough overview of fatigue analysis methods is given that will not be repeated here. To briefly introduce the topic for the purposes of this work, fatigue life analysis is divided into two parts: 1) the stage of life of a component up to crack initiation, and 2) the stage of life of the component undergoing the growth of a crack and its propagation to failure. The combination of the two gives the total life of a component. Perhaps the most often used method to predict crack initiation in a part is the strain-life method [15, 17-19]. Here fatigue life test data (to failure) is fitted to the strain-life curve for specimens, which it should be noted are generally small compared with most components. The point of failure or "life" of the specimen from testing is taken at the point of fracture (i.e. the total life). This can be confusing, since strain-life methods are said to predict crack initiation. However, since the fatigue strength decreases rapidly and cracks propagate quickly in smooth test specimens after crack initiation, the total life from strain-life testing of smooth specimens is taken as the crack initiation life, since the second stage of life is extremely short relative to the first for those test conditions. On the other hand, in notched *sound* specimens, cracks initiate at the notch root relatively soon during testing and the total life of the test piece in such cases comprises mostly the crack growth stage. There is no standard to follow in fatigue testing of cast metal with porosity, but since our test specimens are smoothly machined with internal porosity, it is assumed that crack initiation will be the dominant stage of total life. Once a crack (or cracks) nucleate in the discontinuous porous metal structure, its is assume they will propagate even more quickly than if the metal were sound. Hence strain-life methods of testing and analysis will be used here.

In previous work fatigue life analysis of cast metal specimens containing porosity have involved modeling pores as equivalent notches or cracks [13,14]. This modeling of pores as three-dimensional notches uses the strain-life approach to calculate the fatigue lives of components. Applying only a strain-life model for life prediction assumes that crack nucleation encompasses the majority of the life of the component and that the life-time for fatigue crack propagation to fracture will be insignificant relative to crack initiation. Past use of strain-life fatigue modeling in castings [14-17] has required that pore geometry information, primarily the minimum notch radius and the major axes of the ellipsoidal notch, be known or determined from the fracture surfaces of tested specimens to determine a stress concentration factor K_t. For the second stage of component life (crack growth) linear elastic fracture mechanics LEFM is used to

model pores as pre-existing cracks within the component, and assumes that crack propagation will consume the majority of the fatigue life. Crack propagation is generally assumed to follow the Paris equation. Failure of the component is commonly taken when the remaining net section area stress of the component is at or greater than the yield strength [13,14]. Use of LEFM is often referred to as damage tolerant design.

Here the goal is to validate a methodology to simulate the fatigue life of specimens with porosity using existing commercial software. Finite element analysis (ABAQUS) is used to determine the complex stress field resulting from the porosity distribution, and multi-axial strain-life analysis in *fe-safe* uses those results to determine the fatigue life. Even though prediction of fatigue life and durability analysis from finite element results is relatively new, there are numerous commercial packages other than *fe-safe* available; such as DesignLife, MSC Fatigue, FE-Fatigue, and FatigueWizard to name a few. These use multiaxial strain-life algorithms. In the current work, the complex stress fields due to tomographically reconstructed porosity for 25 specimens are simulated, and a method to predict the resulting fatigue life for these specimens is presented.

II. PROCEDURES

Cast Specimens and Fatigue Testing

For completeness, a summary description of the production and fatigue testing of the cast steel specimens containing porosity is presented below. They were discussed in more detail in our 2003 T&O paper [17] where the fatigue testing was first presented. The as-cast blanks were designed using computer modeling [2, 15] to produce a range of shrinkage porosity levels. The cast blanks were 152 mm long cylinders having a nominal 14.3 mm diameter. To produce a hot spot at the mid-length of the castings, a cylindrical disk of 25.5 mm diameter was positioned at the mid-length of the as-cast specimen as shown in Figure 1. The severity of the hot spot, and resulting porosity, was manipulated by changing the disk thickness (dimension along the casting length); disk thicknesses of 5, 7.5 and 10 mm were cast to provide a range of porosity levels. Generally, a smaller disk thickness resulted in a lower porosity level, but there was overlap of volumetric average porosity level between the three disk thickness groups. Cut-surfaces of specimens from castings having disk thicknesses of 5, 7.5 and 10 mm are shown in Figures 2*(a)*, 2*(b)* and 2*(c)*, respectively. One can see that the porosity level ranges between dispersed macroporosity to holes and gross section loss. Radiographs are shown to the right of each cut specimen surface with a white mark indicating the approximate location of the cut along the length of the machined specimen. Comparing the these radiographs visually, one can make only a qualitative evaluation that the porosity appears to be increasingly severe proceeding from Figures 2*(a)*, to 2*(b)* and to 2*(c)*.

The design of the as-cast blanks concentrated porosity at the centerline and mid-length of the castings so that the porosity could be located in the gage section of the test specimens. Specimens were machined to the dimensions shown in Figure 3*(a)*. The as-cast blanks were machined without visible macroporosity on the specimen surface when viewed without magnification, but on closer inspection using 5x magnification discontinuities from porosity at the surface could be observed in some specimens. The cast steel composition was AISI 8630, and the material was quenched and tempered. All cast blanks received identical heat treatment;

normalized at 900° C, austenized at 885° C, water quenched, and finally tempered for one and one half hours at 510° C. This heat treatment resulted in a tempered martensitic structure with a Rockwell C hardness of 34. The test specimen geometry, preparation and fatigue testing was performed according to the ASTM E606 standard [18]. All fatigue tests were performed under fully reversed, R = -1, loading conditions. Results of the fatigue testing, first given in [17], are presented here for completeness as they will be compared with our current modeling of fatigue.

During fatigue testing the mechanical behavior of the specimens was found to be elastic, so load-controlled testing at 10-20 Hz was used. This allowed for accurate strain amplitude measurements while using the faster testing capability of load control. An extensometer with ends at 6 mm above and below the mid-point of the specimen length was used to measure strain amplitude. The effective (or apparent) elastic modulus E was determined from the extensometer and load data, using the "sound" specimen gage section area A_0 and load to determine the nominal stress and the strain from the extensometer. The measurements for the twenty-five specimens simulated in this paper are given in Table I and reference will be made to individual specimens in the table using the specimen numbers. Four nominal stress levels σ_a were applied and held constant during testing of the specimens; 126, 96, 66 and 53 MPa. The first stress level, 126 MPa, was chosen since this was the run-out stress amplitude for radiographically sound specimens produced from the same heat. The lower stress levels were selected to obtain lives on the order of 10^6 cycles without run-outs occurring. All fatigue tests were performed until fracture of the specimen occurred, or a run-out life was achieved at $5x10^6$ cycles.

The applied load, combined with the individual porosity distribution in a given specimen, resulted in a range of measured modulus of elasticity E and fatigue life data. The range of loads randomized any systematic errors of the effect of applied load on measuring E. In many cases, larger strains were measured in specimens at lower stress levels due to more severe porosity present. The measured modulus of elasticity E was determined from the stable cycle hysteresis loop data for the unloading portion of the loop by taking the average of the data for a large number of cycles. The elastic modulus of 8630 steel without porosity E_0 is taken to be 207 GPa as measured from keel block data [19]. From the measured modulus of elasticity E, an effective specimen area A_e was calculated from $A_e = A_0 \frac{E}{E_0}$. The effective specimen area A_e is the cross-sectional area that a completely sound specimen (with E_0) would have in order to produce the measured strain for the applied test force. The difference between the nominal section area A_0 and A_e could be thought of as an effective porosity area A_{pore}.

Radiographic Measurement, Analysis and Tomography

Results of the radiographic analysis (no tomography) were presented in our 2004 T&O paper [20], and the x-ray tomography results were used in last year's paper [1]. However, the complete procedure used to perform the x-ray tomography has never been written into a T&O paper, and so that procedure is given here for completeness. Film radiography of the fatigue test specimens was performed at Alloy Weld Inspection Co. (Bensenville, IL) using a sensitivity of 2% of the gage section diameter (0.1 mm). Two orthogonal radiographic views of each specimen were shot using marks and a 90 degree gage angle to align the specimens. The film radiographs were digitized using an x-ray scanner resulting in 8-bit gray level, 1200 dpi images. An example radiograph is shown in Figure 3*(b)*. Quantitative analysis of the radiographs was

performed using *ImageJ* [21] to extract gray level and coordinate position data from the radiographs, and software written by the authors to perform the analysis and computed tomography. The radiographs were used to measure and reconstruct the porosity in the test specimen gage sections. Indications on radiographs are typically thought of as "point density" indications, and are directly related here to the thickness of the material. The gray level intensity on the radiographs depends primarily on the total thickness (or effective density) of material through which the x-ray passes, if scattering and spreading of the x-rays is negligible. A gray level versus steel thickness calibration was performed for each radiograph image analyzed using sound selections of the specimen gage sections such as those indicated in Figure 3*(b)*. Since the cross-section of steel through which the x-rays pass is circular, the x-ray paths trace parallel chords of the circle for each radiographic view. The thickness of steel corresponding to these chord lengths is known from the coordinate position data in the planar view of the specimen. The centerline of the specimen is used as the position reference where the maximum steel thickness is the gage section diameter. Moving radially outward from the centerline, additional gray level versus thickness calibration data is generated. Performing this calibration for each radiograph removes the uncertainties of image-to-image variability due to the original x-ray and scanning processes. Radiographic analysis and tomography is performed in the specimen gage section only.

Once a calibration curve for a given radiograph's gray level versus steel thickness for a specimen's image is determined, a mapping between the coordinates on the radiograph and the known nominal specimen geometry is performed. From the specimen geometry, the thickness of steel can be calculated at any point in the radiograph, assuming the specimen is entirely sound. Finally, a calculation of the cumulative steel thickness absent at any point in the radiograph due to porosity can be made by taking the difference between *what the thickness would be if sound* (from the sound geometry to radiograph mapping) and *what the thickness actually is* (from the radiograph gray level and the calibration curve). In terms of a quantitative porosity measure at a given point in a radiographic view, the total porosity along the x-ray path is the ratio between the steel thickness determined to be missing due to porosity and the thickness at that point if the specimen were sound. Since the calibration process is performed for each specimen image, the uncertainty and accuracy of each measurement varies; typically the accuracy of the method to determine total material loss due to porosity is no worse than 300 μm (6% of the gage section diameter) based on the calibration errors and repeatability of the process. However, for two specimens' sectioned surfaces investigated under a scanning electron microscope, the authors have found by measuring total porosity dimensions that the method is capable of identifying individual features as small as 200 μm (4% of the gage section diameter) and determining cumulative material absent due to porosity of the same resolution. More details of the radiographic analysis are given in the 2004 T&O paper [20].

Digitized radiographs for two orthogonal radiographic views of Specimen 3 are provided in Figure 4. At any position along the specimen length, the section thickness from the radiographic analysis can be summed across the specimen diameter to determine the cross-sectional area present in the specimen. Also, by subtracting this from the specimen's nominal section area, the porosity area in a longitudinal section can be determined. The porosity fraction (and percentage) in a longitudinal section area is determined from the ratio of porosity area to nominal section area. In Figure 4, darker indications denote steel that is less dense, having

greater total void dimension in the specimen, as shown by the scale provided. The longitudinal position of the maximum cross-section porosity percentage at +3.2 mm above the mid-length of the specimen is indicated for both views in Figures 4*(a)* and 4*(b)*. A plot of the cross-sectional porosity variation along the specimen length is shown in Figure 5 for the two views shown in Figures 4*(a)* and 4*(b)*. The cross-sectional porosity data for these two views agree with each other quite well in Figure 5, and appear to have a relatively constant offset bias error. There is an excellent correspondence between the longitudinal positions of the maximum cross-sectional porosity in the two views. A horizontal line on the ordinate axis at 5.4 mm^2 in Figure 5 indicates the effective porosity area determined from the measured modulus for this specimen, $A_{pore} = A_0 - A_e$. Good agreement is observed between the maximum value of the section porosity area from the radiographic analysis and A_{pore} from the measured modulus. On the other hand, the horizontal line on the ordinate axis at ~2 mm^2 indicating the average porosity area over the entire gage length does not agree with A_{pore} from the measured modulus. This observation can be generalized for all specimens tested as discussed in last year's T&O paper [1]. In our 2004 paper [20], we had not yet developed the tomography capability and this point was the limit of our abilities to analyze the radiographs for comparison with the fatigue testing results.

Tomography was required to take the analysis further and to reconstruct a realistic three-dimensional porosity field within the specimens so that they could be realistically simulated using finite element stress analysis. A tomography algorithm was developed by the authors based on algebraic reconstruction principles [22]. In the method, a Cartesian grid formed by the x-ray paths of the two orthogonal radiographic views is created over the cross-section of the specimen at lengthwise positions. The dimensions of the grid in the cross-section, and the length increments are defined by the pixel dimensions in the digitized radiograph (1200 dpi or ~21 μm side length). This defines the voxels in which porosity is reconstructed. In each cross-sectional plane, the porosity is determined such that the error between the total void dimension of porosity determined from the radiograph and the total void dimension resulting from the tomographic reconstruction is minimized for both views. The algorithm is iterative and marches by cross-section along the specimen length determining the porosity field. At a given lengthwise position, iterations begin by assuming that a uniform level of porosity produces the total void dimension indicated by the first radiographic view. Next, porosity values in the voxels aligned with the second radiographic view (along x-ray traces orthogonal to the first) are summed to determine a total porosity dimension for this view. After summing, the total dimension is compared with the actual value from the second view, and all values of porosity in the summation are corrected so the total void dimensions agree. Returning to the first view the summation process is repeated; summation along x-ray trace paths followed by a correction to achieve agreement between the total porosity dimensions from the radiograph and that from the summation of voxel porosity values. Typically, about 30 iterations between the two views are required to achieve a minimized error between the densities on the radiographic views and the reconstructed porosity distribution.

In the end, a three-dimensional porosity field is reconstructed such that at each position along the specimen length, the distribution of total void thickness across the specimen diameter for the two x-ray views agree with those determined from the reconstructed distribution. This concept is illustrated in Figure 6 where the total void dimensions from the tomography distribution are compared with measurements from the radiographic analysis at one cross-section position along the length of a specimen. As shown in Figures 6*(a)* and 6*(b)*, the tomography

provides a reconstructed porosity field having dimensional characteristics that agree very well with the porosity void dimensions measured in the two radiographic views across the specimen diameter at a lengthwise position. These results are typical for any lengthwise position, and essentially represent the converged solution for the tomography algorithm for a single cross-sectional slice.

Comparisons between cross-sections of the reconstructed porosity field and selected cut/polished sections of specimen surfaces examined under a scanning electron microscope assisted the determination of parameters used in the algebraic reconstruction algorithm. For instance, the minimum value of porosity allowed in a voxel was 5%, based on detectability limits and the ability to resolve the interfaces of larger cavities as shown in Figure 7 for Specimen 22. Here the tomographic distribution is compared with an image of the cut surface from the specimen at the same lengthwise position examined after mechanical testing. The porosity amount and features of the reconstructed field compare well with the cut section considering only two x-ray views were used. Figure 7 shows the three-dimensional nature of the distributions generated by the tomography technique via the iso-surfaces of porosity ϕ = 0.75 distributed along the specimen length. The tomography results were found to be a good representation of the porosity field for the purposes of this study. Certainly, using more radiographic views and additional algorithm development will improve the fidelity of the reconstruction. Even so, results from this tomography algorithm were adequate for quantitative comparative analysis of the differences in porosity distributions. Using these tomography results we have found that the stiffness response of the specimens can be predicted within ±10% using a relationship between the local elastic modulus and porosity

$$E(\phi) = E_0 \left(1 - \phi/0.5\right)^{2.5} \tag{1}$$

where E_0 is the elastic modulus of the sound material and ϕ is the porosity volume fraction [1].

Simulation Procedures

The porosity data determined by tomography in the cylindrical specimen gage section was mapped to the nodal locations of a finite element analysis (FEA) mesh used to simulate the stress-strain fields in the specimen. The three-dimensional quadratic interpolation subroutine QD3VL from the IMSL Math Library was used to map the porosity data onto the FEA mesh [23]. Ten-node quadratic tetrahedral elements were used to perform the stress analysis. Elastic mechanical properties are defined as a function of porosity, and the elastic behavior of each specimen is simulated using porosity dependent properties that vary locally with its porosity field. Details for this are given in last year's T&O paper [1]. Equ. 1 was used the define elastic modulus and a function of the local porosity at a node in the finite element mesh, and the Poisson ratio ν depends on porosity ϕ at nodes using a relationship from Roberts and Garboczi [24]

$$\nu(\phi) = \nu_S + \frac{\phi}{\phi_\infty}\left(\nu_\infty - \nu_S\right) \tag{2}$$

with ν_∞ = 0.14, ϕ_∞ = 0.472 and ν_S = 0.3. Significant plasticity was not detected during testing of the specimens so plastic effects were ignored in the FEA simulations. Mechanical simulation

of the specimens with porosity was performed using the commercial FEA package ABAQUS/Standard version 6.6.1 [25].

FEA simulation boundary conditions were prescribed to closely match the test conditions. During testing, specimens were held fixed at their upper grip, and the loading was applied to the lower (ram) end which was free to move vertically placing the specimen in tension and compression during fatigue testing. The simulated specimen geometry considered only the initial 5 mm of the length of the grips in the FEA mesh. This was a more than sufficient distance away from the fillet and test section to produce stress-strain results which were insensitive to where the boundary and loading conditions were applied. The only difference from simulations using more of the grip length was longer execution times. At the upper grip face, a clamped boundary condition was applied (having no translations or rotations), and at the lower grip translations were allowed only in the axial direction with no axial rotation allowed. A uniform distributed loading was applied over the face at the lower grip end to produce the total load corresponding to the testing conditions.

After running ABAQUS, the resulting stress fields corresponding to the tension and compression steps of the fully reversed loading (R = -1) are imported into the *fe-safe* as an ABAQUS results file (termed a .fil file). A loading definition is configured in *fe-safe* defining the cycle of loading. The porosity field can be imported in the same file. The strain-life fatigue properties for the sound material [19] are entered into the *fe-safe* model, and *fe-safe*'s multi-axial Brown-Miller algorithm with Morrow mean stress correction is used to calculate the fatigue life as cycles to failure. For steel, *fe-safe* recommends using the multi-axial Brown-Miller algorithm for ductile steel and the Principle Strain algorithm for brittle steels, both with Morrow mean stress correction. Brow-Miller is said to be a more conservative method that Principle Strain. The properties and equations will be presented in the RESULTS section. Average nodal stress tensors are used from the ABAQUS simulations and converted the strains within the *fe-safe* software using an elastic modulus of 207 GPa. As long as this elastic modulus is used throughout the calculations, use of a variable E is not necessary since the alternating strain amplitude and the elastic term in the strain-life equation scale with whatever modulus is used. Using a sound modulus E_0 in *fe-safe* and strains determined using a sound modulus E_0 from the ABAQUS stresses in *fe-safe* give the same results as using a variable E in *fe-safe* and strains directly from the ABAQUS results produced using the variable E. In other words, the same life results if one calculates the strain-life by either of the two methods below:

1. Using the strains from the ABAQUS simulations using E dependent on the local porosity and the same variable E in the *fe-safe* strain-life calculations.

2. Using the stress field from the ABAQUS simulations run using E dependent on the local porosity and to generate the strains within *fe-safe* using the sound modulus E_0 to perform the conversion and then using the sound modulus E_0 throughout in the *fe-safe* strain-life calculations.

The authors use method 2 because of its relative simplicity. The validity of the method has been checked using uni-axial strain-life test calculations in *fe-safe* and by the authors' own solution to the strain-life equations.

Fatigue life predictions from FEA results using multi-axial strain-life algorithms, such as those in *fe-safe*, are very sensitive to local stresses. The peak local stress will be shown to depend in some cases more than others on the degree of grid refinement in the FEA simulations. It is beyond the scope of the present study to directly resolve the geometry of the pores on a microscopic scale in the FEA simulations. This would require a FEA mesh (and a tomographic reconstruction) with a resolution of the order of 1 μm over a specimen gage length of approximately 20 mm, which is not possible given present-day computing resources. Instead, a porosity volume fraction ϕ is defined for a representative elemental volume that is large compared to the pore microstructure but much smaller than the specimen itself. The effect of the pore geometry on stiffness is accounted for by Eq. 1 in an average sense. The FEA node spacings used in the present study were chosen to be between one and two orders of magnitude larger than the size of the voxels in the tomographic porosity reconstruction (~21 μm), i.e., between 100 μm and 1 mm. Such FEA node spacings are large enough to allow for a meaningful calculation of porosity volume fractions from the tomographic data, but small enough to resolve variations in the porosity over the entire specimen volume. A detailed investigation of the sensitivity of the simulation results to the choice of the node spacing is presented in the RESULTS section.

III. RESULTS

Results of Fatigue Testing

Monotonic, cyclic and fatigue material properties for sound 8630 steel are shown in Tables II and III. These properties are used in the *fe-safe* simulations along with the stress field from the FEA analysis using the locally reduced elastic properties from Equs. 1 and 2. The cyclic stress-strain curve is used to determine the material properties which relate the nominal true stress and true strain ranges as given by Equ. 3

$$\Delta e = \frac{\Delta S}{E} + 2\left(\frac{\Delta S}{2K'}\right)^{\frac{1}{n'}} \tag{3}$$

where the symbols ΔS and Δe are the nominal true axial stress and true axial strain, respectively, E is Young's modulus, K' is the cyclic strength coefficient, and n' is the cyclic strain hardening exponent. Values for these properties are given in Table III. The value of cyclic yield strength, S_y', was found to be 661 MPa, which is less than S_y (comparing Tables II and III), indicating that the material cyclic softened. Cyclic softening commonly occurs with high strength materials and results in softening of the material as the cyclic loading progresses. When using finite element analysis results to perform fatigue life analysis, the cyclic properties in Equ. 3 should be used in the modeling an elastic-plastic analysis if there is significant plasticity [27].

A strain versus cycles to failure ε-$2N_f$ curve shown in red in Figure 8 for the sound material is taken from [19] and compared with the specimens with porosity. This **strain-life curve** is

$$\frac{\Delta \varepsilon}{2} = \frac{\Delta \varepsilon_e}{2} + \frac{\Delta \varepsilon_p}{2} = \frac{\sigma_f'}{E}\left(2N_f\right)^b + \varepsilon_f'\left(2N_f\right)^c \tag{4}$$

where $\Delta\varepsilon/2$ is the total strain amplitude, $\Delta\varepsilon_e/2$ is the elastic strain amplitude, $\Delta\varepsilon_p/2$ is the plastic strain amplitude, σ_f' is the fatigue strength coefficient, b is the fatigue strength exponent, ε_f' is the fatigue ductility coefficient, and c is the fatigue ductility exponent. The values for σ_f', b, ε_f', and c for sound 8630 steel are given Table III and were determined by a curve fitting test data [19]. Fatigue and durability prediction software use this uniaxial data in multiaxial fatigue algorithms, and the values in Table IIII were used in the *fe-safe* predictions for sound 8630 steel.

The fatigue lives of the porous specimens are shown in Figure 8 and are seen to fall far below the sound material curve. The lives of the specimens are seen to range from 160 to a runout ($> 5 \cdot 10^6$ cycles), and when the porous data is examine in detail (see Figure 9) observe that both the 160 cycle and runout specimens occur at the highest test stress amplitude, 126 MPa. Examining these results for all stress levels in Figure 9 (126, 96, 66 and 53 MPa) there is considerable scatter at any given level, but a general trend that longer lives occur at lower stress levels. From Table I, note that the average porosity in the specimens is between 8% and 21% and our earlier work [20] showed that there was little correlation between average porosity and life (or E for that matter). However, a decent correlation between the back-calculated fatigue notch factor K_f from the test results and the maximum cross-section porosity measured from the specimen radiographs was shown in past work [20]. Unfortunately, these results showed the K_f (not applied locally but to the entire specimen) might vary by a factor of 2 or more at a given maximum section porosity. These results demonstrated that each specimen has a unique porosity field, which in combination with loading results in a complex stress field that must be accurately simulated in order to predict the fatigue life of a given specimen, as is done now in the current work.

Results of Fatigue Life Simulations using Multiaxial Strain-life Method

The field of fatigue life prediction using finite element results is relatively new with commercially available software only appearing in the last ten years or so. There are not yet established standards or universally agreed upon methods for designing for fatigue using finite element results. The concepts of uniaxial strain-life (and the properties from uniaxial testing) can be extended to multiaxial fatigue through three equations: a stress-strain relationship (such as Equ. 3), a strain-life equation (something analogous to Equ. 4 for the uniaxial case) and a multiaxial version of Neuber's rule to account for local plastic effects when using elastic stress-strain FEA resuts. In addition to these three equations, multiaxial strain-life fatigue algorithms use the concept of *critical plane* analysis. In critical plane analysis, the calculated strain tensor at a finite element node (having three direct and three shear components) is resolved onto a number of planes where the damage associated with the strain is evaluated on each plane. Then, the plane with the most damage is selected for use in the strain-life algorithm calculations. In a Cartesian x-y-z coordinate system unique planes can be defined by the orientation the normal of the plane surface makes with respect to the coordinate system. This orientation can be defined by one angle from the x-axis towards the y-axis, and a second angle from the z-axis towards the x-y plane [27]. Here *fe-safe* is used, which, depending on the algorithm, searches for the critical plane with the worst damage (shortest life calculation) in 10 degree increments over the 180 degree range of angle one (above) and the 90 degree range of angle two. Direction cosines are used to calculate the strains onto the calculation plane. This description is intended only as a brief glimpse into multiaxial fatigue analysis for a comprehensive book on multiaxial fatigue consult Socie and Marquis [28].

The results here use the Brown-Miller algorithm with Morrow mean stress correction as the strain-life model with a critical plane analysis. The life $2N_f$ is determined by solving

$$\frac{\Delta\gamma_{\max}}{2}+\frac{\Delta\varepsilon_n}{2}=1.65\,\frac{(\sigma'_f-\sigma_m)}{E}\left(2N_f\right)^b+1.75\,\varepsilon'_f\left(2N_f\right)^c \quad (5)$$

at each node, where $\Delta\gamma_{max}/2$ is the maximum shear strain amplitude and $\Delta\varepsilon_n/2$ is the normal strain to shear stress plane. The critical plane is defined as the plane having the maximum value of $\Delta\gamma_{\max}/2+\Delta\varepsilon_n/2$. As mentioned earlier, this algorithm is recommended for ductile steels. For brittle steels, the maximum principle strain multiaxial algorithm is recommended. This algorithm is formed by replacing the left-hand side of Equ. 4 with the maximum principle strain from the critical plane having the largest value for any plane through the node

Neuber's rule and the calculation of local notch root stress and strain ranges were left out of the earlier discussion of the strain-life equations (Equs. 3 and 4) since they do not relate to test data. It is used to calculate the local effects of notches and discontinuities. The uniaxial local notch stress and strain is calculated from the nominal stress and strain ranges by solving Neuber's rule (Equ. 6 below) and the cyclic elastic-plastic stress-strain curve with the true notch stress and strain (Equ. 7) simultaneously

$$\Delta\varepsilon\cdot\Delta\sigma=K_f^2\Delta e\cdot\Delta S \quad (6)$$

$$\Delta\varepsilon=\frac{\Delta\sigma}{E}+2\left(\frac{\Delta\sigma}{2K'}\right)^{\frac{1}{n'}} \quad (7)$$

where K_f fatigue notch factor, $\Delta\sigma$ and $\Delta\varepsilon$ are the local axial stress and strain at the notch root, respectively, ΔS and Δe are the nominal true axial stress and true axial strain. The material properties E, K', and n' are those of the sound specimens from Table II. For the uniaxial fatigue life calculation using local notch strain range, the resulting $\Delta\varepsilon$ is calculated using Equs. 6 and 7 is used in Equ. 4 to determine the life of the specimen. Multiaxial versions of Neuber's rule Equ. 6 use the strain and stress in the critical plane associated with the algorithm used (i.e. both the maximum shear strain amplitude and the normal strain in the case of the Brown-Miller algorithm).

All the preceding details are handled internally in the *fe-safe* software, the user need only define the uniaxial strain-life and cyclic stress-strain properties and import the finite element stress field (in the case of an elastic simulation) or the stress-strain field (in the case an elastic-plastic FEA simulation). Then the algorithm is selected, and the fatigue life prediction can be run. Nodal value of the FEA simulation are used since they lie on the surface of the component being simulated, defining it better than the integration points which are internal. Integration points can also be used if desired.

Fatigue results for all specimens were run using the elastic simulations results that were first run to compare predicted and measured stiffness properties of steel with porosity [1]. A nodal grid spacing of 0.25 mm was used in these simulations; this our "baseline" grid. This grid of approximately 20 nodes across the specimen diameter was found to give acceptable convergence for the stiffness simulations. The fatigue life prediction is taken as the shortest life

resulting at any node in the *fe-safe* calculations. The results are plotted in Figure 10, where a line of perfect correspondence is given to aid the reader in determining whether a result is conservative (below the line) or nonconservative (above the line). If an FEA fatigue life prediction is within one decade of measurement one can consider it to be within reasonable agreement. Note that eighteen of the data points appear to be within that margin and correspond well with the test results. Of these, only five are conservative. Seven data points are seen to be in poor agreement with the measurement and nonconservative, and two of these have predicted lives about three decades longer than the measurement.

Since the fatigue life prediction is very sensitive to stress concentrations, Specimen 19 was run at three FEA meshes finer than the baseline grid to see the effect on life prediction. The three finer grids had nodal spacings of 0.16, 0.12 and 0.09mm. With each increase in mesh fineness, fatigue life prediction became shorter due to the increase in the local severity of the stress since more detail and stress concentration was resolved in the simulation. This is indicated in Figure 11 as the red triangles progress downward with increasing mesh fineness for Specimen 19. The stress fields on the surface of specimen 19 are shown in Figure 12 for each of the grids. Note that the maximum stress predicted increase from 400 MPa for the baseline case to 467, 488 and then 602 MPa for the finest mesh. The finest mesh gave excellent agreement with the measurement. Specimen 20, which was in very poor agreement with the measurement for the baseline grid, was simulated using two coarser grids than the baseline case (0.42 and 0.58 mm nodal spacings) and then using the three finer grids. Note that all six computational grids are shown in Figure 13 for visual comparison. As shown in Figure 11 for specimen 20, the coarsest mesh predicted the longest life progressing to the finest grid which predicted the shortest life of all grids. Figure 14 is given to emphasize this result, showing the decreasing predicted life with smaller nodal spacing converging to about 390,000 cycles. Though nonconservative, this result is in reasonable agreement with the measured life for this specimen, about 250,000 cycles. An additional specimen, Specimen 17, was also run for all six grids, and these results are given in Figure 15. The same trend is seen as is in Figure 14, decreasing life with finer mesh spacing. In this case the predicted life converges to about 600 cycles and the measured life was about 4400.

These results, and additional fine mesh runs on other specimens emphasized the sensitivity of FEA fatigue life predictions to local stress severity. In all cases increasing the mesh fineness resulted in lower life until they appear to approach convergence. If a mesh finer than the tomography results was run, and resolved all discontinuities sufficiently, total convergence could be achieved. However, that is beyond our computational hardware abilities and probably of no practical use. The more important question to pursue is - can a method be devised to predicted life on a coarser mesh that is close to the converged solution on a fine mesh for these test specimens? Much of the remainder of this paper covers the analysis and methods that were devised for addressing this question.

Development and Results of Adaptive Subgrid Model for Fatigue Life Prediction

Computer simulation models that resolve phenomena smaller than the computational grid are often referred to as subgrid models, and one that adapts based on the ability of the grid to resolve could be called an adaptive subgrid model. Such a model is required in the case of these fatigue life predictions. As a starting pointing, a spherical hole was simulated in a 5 mm cylinder (the specimen diameter) modeling it as a feature (an actual meshed hole) and as a spherical field

of nodes having 100% porosity of the same size. The two cases (meshed feature and as porosity field) are compared in Figures 16*(a)* and 16*(b)*, respectively. The size of hole in this case is 0.2 mm diameter. The size of hole is chosen to be small enough that the results are not influenced by the diameter size, and in order that the results may be compared with stress concentration handbook values [29]. The handbook calculation of the maximum stress for this hole geometry with a nominal stress of 207 MPa is approximately 424 MPa. Not surprisingly, the maximum stress in the FEA simulation in Figure 16*(a)* is 426 MPa and is very close to the handbook calculation value, in fact the FEA result is probably more accurate since the handbook chart was read manually and therefore has some degree of uncertainty. Note that the FEA grid in Figure 16*(a)* has many nodes appropriately concentrated at the edge of the hole and resolves it quite well. In Figure 16*(b)* the FEA mesh and stress field for the porosity field case is shown; it has a maximum stress of 438 MPa, about 3% higher than the handbook calculation. The stress fields in Figure 16 are imported into *fe-safe* and fatigue lives are predicted. The fatigue life prediction for the porosity field case is shown in Figure 17. The minimum life is found to be 135,330 cycles to failure assuming R = -1 fully reversed loading for the nominal applied stress. Strain-life fatigue life calculations performed by hand for the maximum handbook stress give 138,425 cycles to failure. The fatigue life distributions (below 2,000,000 cycles) for the two cases are shown in Figures 18 and 19, for the hole meshed as a feature and hole meshed as a porosity field, respectively. The handbook life calculation is indicated in each figure. Both are shown to agree with the handbook calculation, at the lowest life end of the distribution. Though the meshed porosity field could be made finer, this mesh fineness was determined to be sufficient for achieving good agreement. This shows how the simulations using porosity field and feature coincide if the meshes are fine enough.

Next, simulation cases were run on coarser meshes using the porosity field model of the spherical hole. The values of maximum stress for those cases were compared with the handbook calculation. The stress concentration factor required to amplify the maximum stress for a given coarser mesh simulation to the maximum stress corresponding to the handbook fatigue life is defined as $K_{t,c}$. The porosity field for a coarse mesh case using a 0.2 mm grid spacing (approximately a 0.1 mm node spacing) for the 0.2 mm diameter hole is shown in Figure 20. Since the grid spacing is fairly coarse, the hole is poorly resolved. The stress field resulting from the FEA analysis for this coarse grid is shown in Figure 21, and the maximum stress is only 264 MPa. The $K_{t,c}$ to reach 424 MPa (handbook stress) is 1.61. When simulations like this are made over a range of node spacings the trend appears as shown in Figure 22 for both the 0.2 mm hole and a larger 0.5 mm diameter hole. As the node spacing is increased the $K_{t,c}$ increases until the computational grid fails to pick up any discontinuity due to the sphere at all. At this point $K_{t,c}$ becomes the gross section stress concentration for the sphere in the cylinder [29]. If the sphere is made small enough, such as these two sizes, this $K_{t,c}$ corresponds to a spherical hole in an essentially infinite body so $K_{t,c} = 2.045$.

The two results in Figure 22 depend on the mesh size relative to the hole size. In order to remove this dependency, the same data is plotted in Figure 23 as $K_{t,c}$ versus the node spacing to hole diameter ratio. Given the randomness of how the grid discretizes the hole and this effect on the computations, and that there is actually a range (albeit small) of nodal spacings, the two curves appear to collapse well onto a curve which is

$$K_{t,c} = 2.045 + (1 - 2.045)\, e^{-(\text{Node Spacing}/\ \text{Hole Diameter}) / 0.6428} \tag{8}$$

One could replace the "2.045" with another maximum stress concentration value if desired, and achieve a similar dependency between that discontinuity and grids ability to resolve it. Certainly, this could be studied in more rigorous detail, but the goal here is to determine an engineering approach to address grid dependency is the fatigue life calculations. For now, this relationship between the effect of the discontinuity and the grid looks promising.

In [15,17] it was shown that the effect of microporosity on fatigue could be calculated using the notch sensitivity fatigue notch factor K_f taken from [26] using the pore sizes observed on specimen fracture surfaces. This relationship is

$$K_f = 1 + \frac{K_{t,\max} - 1}{1 + a/r} \tag{9}$$

$$a = 0.0254 \cdot \left(\frac{2070}{S_u} \right)^{1.8} \tag{10}$$

where r is the notch root radius in millimeters, $K_{t,max}$ is the stress concentration factor for the discontinuity and S_u is the ultimate strength of the material in MPa. When the fatigue notch factor $K_f = K_{t,max}$ the material is fully notch sensitive; here a fully notch sensitive evaluation of Equ. 9 will be termed $K_{f,max}$. In [15,17] $K_{t,max} = 2.045$ was used since the single micropore has little impact on raising the net section stress distribution. The subgrid model should account for this notch sensitivity at small pores where $K_f < K_{t,max}$ and should revert to the microporosity relationship in such cases, since no practical FEA mesh will be able to resolve these micropores. Hence, at micropores a practical mesh (about 0.5 mm node spacing and larger) will typically have a nodal spacing to pore diameter ratio > 2, so $K_{t,max} \approx 2.045$ in Equ. 9. Then the resulting K_f should revert to the relationship dependent on pore size shown in Figure 24 as used in [15,17].

Since *fe-safe* only allows for users to apply constant fatigue notch factors to the entire surface of the part, or to the entire part, a variable fatigue notch factor throughout the part such as will be required to use this subgrid fatigue model is not readily applied within the software. Users of *fe-safe* can, however, define the static and fatigue material properties (strain-life and cyclic stress strain, refer to Tables II and III) as functions of temperature. The subgrid model must then be applied within *fe-safe* by importing the fatigue notch factor field at the nodes into *fe-safe* as an ABAQUS results file temperature field, and defining the fatigue properties (σ_f', b, ε_f', and c) as functions of fatigue notch factor. This is not trivial since a given K_f results in a strain-life curve by solving Equs. 6 and 7 simultaneously and then using the results in solving for $2N_f$ in Equ. 4 over the entire strain range desired. To determine the fatigue properties as functions of K_f , the error is minimized between an entire strain-life curve developed using a given K_f value and sound fatigue properties, and an entire strain-life curve with no K_f (or = 1) for given values of the fatigue properties σ_f', b, ε_f', and c. For each strain-life curve, the fatigue properties σ_f', b, ε_f', and c are iterated on and solved until the curve resulting from using their values matches the curve for a given K_f. Software was developed by the authors to perform this exercise, and the resulting dependencies of the fatigue properties on K_f are given in Figures 25 through 28 for σ_f', b, ε_f', and c, respectively.

The next undertaking requires developing a relationship between the amount of porosity (pore fraction) and representative pore size. This *Pore Size Model* will be used to define the hole diameter in Equ. 8 and the radius of the notch in Equ. 9 based on the local pore fraction at a node. In the case of this work, the porosity is from the tomography data, but in practice it will be the pore fraction from a casting simulation, i.e. MAGMAsoft. Approximately two years ago, we developed a probabilistic *pore size distribution model* which is in many ways similar to the approach taken in a very recent article [6]. This model is used to guide the proper selection of the pore size model. A pore size model results that uses this pore growth and merging model and comparisons of this model with measurements of porosity size and distribution from specimen surfaces and analysis of the ASTM radiographs [30]. Beginning with the an assumption that the porosity is a uniform spacing of spherical pores, the pore fraction is given by

$$\varepsilon_p = \frac{4\pi}{3} n_0 r_{sphere}^{\ 3} \tag{11}$$

where r_{sphere} is the pore radius, and n_0 is the number density of pores. Image analysis measurements were made on two specimen surfaces having microporosity, and an average pore spacing d_p was found to be 177 to 344 μm for multiple views on polished surfaces. The pore density from these measurements, n_0, was then found to be $2.4\text{x}10^{10}$ to $1.8\text{x}10^{11}$ pores/m^3 by the relationship

$$d_p = \left(1/n_0\right)^{1/3} \tag{12}$$

for the assumption of a uniform spacing of spherical pores. The measurements just mentioned were made on specimens where the area fraction (also then pore fraction) is about 0.7%. It can readily be demonstrated that the pore size distribution and pore merging must be accounted for to attain physically realistic results. Consider, as has been observed, that microporosity usually has pores ranging from 10 to 50 μm diameter, but often a 100 μm appears on the same surface. For a pore radius r_p = 100 μm and a $n_0 = 10^{11}$ pores/m^3 , which was measured, the spherical model Equ. 11 gives ε_p to be about 42%. This is unrealistic, and merging must be considered. A distribution of pore sizes with a number density corresponding to a pore size, or pore size range, must be used, and merging must be considered.

The details of the pore size distribution model with merging are beyond the scope of this paper, but a brief discussion will be given to understand its basis. Assuming a lognormal distribution of pore sizes that nucleates when porosity forms, it is assumed that as additional porosity forms the pores in the distribution grow proportionally to the square of their radius and no further pores nucleate. The total porosity amount as porosity grows is given by a summation of Equ. 11 over the entire distribution of pore sizes. From the entire pore size distribution a mean pore radius R_{mean} and a mean or total pore spacing $d_{pore} = n^{-1/3}$ can be calculated, where n is the total number density. The *merging criterion* used is that pores are capable of merging if their radius exceeds half the total pore spacing $R_{pore} > d_{total}/2$. The *frequency of pore merging* is determined by the probability that two pores will take part in a merging event. This requires a probabilistic approach. This probability is dependent on the product of the number density ratios of the merging pores (either within a bin of single pore size meeting the merging criterion or between two bins of different pore sizes). The number density ratio is number density of one pore size bin divided by the total number density. By this model, merging pores continue to form as part of the distribution, they continue to merge and grow along with the distribution.

Also, note that n decreases (d_{pore} increases) as the mean pore radius increases. There are numerous parameters used in the pore size distribution model, such as those defining the shape of the initial nucleation size distribution and initial total number density, and reasonable physical values for these will give a range of results. Nevertheless the model gives insightful results that can be used along with measurements as a basis for selecting a pore size model.

Representative pore size distribution model results are given in Figures 29 through 32. Figure 29 compares the distributions of pore sizes as the porosity level increases from the nucleation distribution at 0.1% to 5% porosity with 1% and 3% shown in between. The number density is shown on a non-log scale so the order of magnitude of the decrease in number density can be more easily compared. The initial nucleation total number density is a parameter in the model, and this was taken as $n = 10^{12}$ pores/m^3 based on our measurements at approximately 1% porosity and comparing back to the nucleation condition required to have reasonable agreement. Significant merging is seen starting around 3% as observed near 100 μm where a second distribution of merged pores is taking shape. This merged distribution is more readily apparent in Figure 30 where the result at 5% is plotted alone and rescaled; here the merged distribution appears to have a mean of just over 100 μm diameter. At 10% the total number density is about 1 pore/cm^3 and R_{mean} is approximately 1 mm. This agreed with measurements of ASTM radiographs [30] having pore radii of about 1mm. The model parameters seemed physically reasonable. The distribution at 10% porosity is shown in Figure 31 for a non-log and in Figure 32 on a log-scale. Pore diameters are seen to range up to several millimeters, and the merging pore distribution is very readily seen in Figure 32. Because of the assumptions in the model, it is not believed to produce reasonable results at larger porosity levels. It does not take into account microstructural and effects of solidification interacting with pore size. Only results to 10% porosity are shown here.

Figures 33 *(a)* and *(b)* compare results of the pore size distribution model with measurements made previously. From the analysis of the ASTM radiographs [30], the pore radii at low pore fractions are seen to be much larger (between 500 μm and 1 mm) in the radiographs than predicted by the model. In our analysis of cut specimen surface with microporosity (up to about 2% porosity), shown in Figure 33 *(b)*, pores radii no larger than about 10 to 20 μm were observed, and these values fall below the mean of the pore distribution model. Looking at Figure 29, the reader will note the pore distributions at 1% and 3% porosity show the size range of 10 to 20 μm range which is more reasonable than the ASTM measurements. It can only be summarized that the ASTM radiographs are not good material from which to determine an *absolute* amount of porosity since they only indicate porosity detectable by radiography, and it is know that the "Microporosity Specimens" data in Figures 33 *(a)* and *(b)* is radiographically sound as well. It is highly likely that the ASTM radiograph data in Figure 33 *(a)* should be shifted to the right, having more actual porosity for a given radii measurement. The exact amount of shift though is difficult to determine without performing measurements on the plates from which the ASTM standards are based.

Examining these results, and considering that the resulting pore size model would be used in fatigue calculations, it was determined that the pore size should track the maximum (worst case) from the pore distribution model. The large pore sizes at low pore fractions from the ASTM radiograph study are disregarded. When pore merging dominates the distribution model

around pore fraction of 0.1, the pore size distribution model is thought to become unrealistic. The final pore size relation that was dselected is shown in Figure 34 and is compared with the pore size distribution model results up to slightly over 0.1 pore fraction. After this the distribution model pore sizes grow exponentially due to overly aggressive merging and finally level off at about 3 cm radius. The pore size model piecewise curve that was selected is shown in Figure 35; it is

$$R_{pore} = \frac{282.52 \cdot \varepsilon_{\text{pore}}}{1.0 + 25846.63 \cdot \varepsilon_{\text{pore}} - 275154.35 \cdot \varepsilon_{\text{pore}}^{\,2}} \quad \text{for } \varepsilon_{\text{pore}} \le 0.0386 \tag{13}$$

$$R_{pore} = 0.176888 - 0.166247 \cdot \exp(-21223.91 \cdot \varepsilon_{\text{pore}}^{\,3.98865}) \quad \text{for } 0.0386 < \varepsilon_{\text{pore}} < 0.0941$$

$$R_{pore} = 0.3563 + 0.08877 \cdot \log(\varepsilon_{\text{pore}}) \quad \text{for } \varepsilon_{\text{pore}} \ge 0.0941$$

where ε_{pore} is the porosity fraction.

The results of the pore size model are integrated into the subgrid fatigue model through custom software that generates the fatigue notch factors at the ABAQUS finite element nodes. This is done by post processing the ABAQUS results file. The software algorithm operates as outlined below:

1. ABAQUS binary results file is read in, most importantly: mesh geometry, nodal averaged stress and strain tensor data, and porosity values at nodes. Note: strain is not currently used.
2. Porosity size model Equ. 13 is used to calculate pore sizes at nodes based on porosity at node.
3. Finite element grid is interrogated at all nodes so that the local nodal spacing is determined at each node based on the nearest neighboring node.
4. If porosity exists at a node, results from steps 2 and 3 are used in Equ. 8 to determine $K_{t,c}$ accounting for the subgrid porosity not resolved in the FEA analysis.
5. Equs. 9 and 10 are used to determine the final fatigue notch factor K_f at a node based on notch sensitivity concepts.
6. New ABAQUS binary results file is generated for use in *fe-safe*: mesh geometry, nodal averaged stress and strain tensor data, and subgrid calculated fatigue notch factor values at node which needs to be written out as an ABAQUS "TEMP" temperature field for use in *fe-safe*.

The subgrid fatigue model results from *fe-safe* show greatly improved predictions for coarser grids that are closer to the converged fine mesh results. The grid study results from Figures 14 and 15 are repeated in Figures 36 and 37 for comparison with the subgrid fatigue model. Note that the maximum notch factor used is 2.045. As noted earlier, this value could be modified, but it is based here on the concept of a spherical pore. There are numerous other geometries that would produce higher K_f [29] values, but it is desired that this model to be able to reproduce the microporosity results produced earlier. A higher K_f would not accomplish that.

At the three finest meshes, the subgrid model has no effect in Figures 36 and 37 since the meshes are fine enough to resolve the most important features in the stress field. For the three coarser meshes, the sub grid model results are in some cases an order of magnitude closer to the converged fine mesh results, and even more so in the case of Specimen 20 shown in Figure 37. For Specimen 20 the improvement relative to the fine mesh results is dramatic. Examining all results on the baseline 0.25 mm nodal spacing, the subgrid fatigue model improves the predicted and measured comparison, especially for the worst nonconservative data points, as shown in Figure 38 where the original results are compared with the subgrid model. Vertical lines are used in the figure to indicate data points which move appreciably using the subgrid model. To recap, the subgrid model uses the ABAQUS simulated stress field, *fe-safe* and fatigue properties dependent on K_f as shown in Figures 25 through 28 with the multi-axial Brown-Miller algorithm with Morrow mean stress correction is used in *fe-safe*. Predicted life is taken as the smallest life in the *fe-safe* calculation. In Figure 38, there are also test data points where the subgrid model has little or no effect, indicating that the stress field and features are already adequately resolved. This is particularly true at lower lived specimens where the fatigue life is governed by higher stresses overall, rather than the local details of the stress field influenced more by porosity.

Although it is an improvement over the original fatigue model, the subgrid fatigue model had six data points lying outside of one decade of agreement on the nonconservative side (see Figure 38). This is undesirable from a safety factor standpoint in a predictive model. If there is disagreement outside of a decade; it would be best to have it on the conservative side. Since the x-ray tomography cannot detect microporosity, it was decided to investigate the effect of a low background level microporosity on the fatigue life predictions. There is a background level of microporosity undetectable by the radiography in the specimen. Since casting simulations predicted porosity throughout the specimen gage section [15], and small micropores could be found (as they can usually be found) dispersed in the background of sections with larger macroporosity, it seems a logical theory to test. After several iterations, including using higher values of maximum notch factor (up to $K_{f,max} = 4$), it was decided that a uniform background pore size no smaller than 100 μm radius be used everywhere (even at sound nodes). However, when the pore size model gives larger value of radius, the larger value is used. This is based on the observation (see Figure 33 and [17]) that even in specimens with mean pore sizes on the order of 10 μm it is not uncommon to find pore sizes on the order of 100 μm. This is also approximately the initial maximum pore radius in our pore size model Equ. 13.

The comparison between the measured and predicted fatigue lives of specimens using the baseline node spacing for the subgrid fatigue models with and without the background porosity of $R_{pore} = 100$ μm is shown in Figure 39. Again, vertical lines are used in the figure to indicate data points which move appreciably due to the addition of the background porosity. The lowered fatigue lives are primarily due to steel which was previously modeled as 100% sound (which also exhibit higher stresses due to stress redistribution) now having $R_{pore} = 100$ μm. Note that the addition of the background porosity to the model affects some data points more than others. Overall the agreement is greatly improved with the measurements, as shown in Figure 40, where only predictions versus measurement results for this final "recommended" model of fatigue for test specimens is given for the subgrid model with background porosity.

It should be pointed out that in applications of the fatigue model casting simulation tools are now able to predict porosity such as the background microporosity that is not detectable by radiography. Therefore, the addition of a background field of porosity would not be used to analyze a real casting using the porosity predictions from simulation. One reason that a background field is used here for the specimens is because simulation predicts that it should be.

Results from an Example Casting Case Study

The affects of the porosity formed in the casting process on fatigue life of a nozzle casting is presented as an example case study. The analysis uses the fatigue properties and subgrid fatigue model previously described here. Half-symmetry is used in both the MAGMAsoft casting simulation and the ABAQUS and *fe-safe* part service performance analysis. An advanced porosity prediction module in MAGMAsoft was used to simulate the casting process as shown in Figure 41. Only a small amount of macro-porosity, which would be visible without magnification, is predicted on the outside surface of the casting at riser contacts as shown circled in Figure 42 *(a)*. The remaining porosity in the casting is limited to microporosity at the centerline of the housing or bell-shape nozzle wall as seen in the x-ray view shown in Figure 41 *(b)*. The MAGMAlink program is used to transfer the porosity field from the casting simulation (as-cast part) onto the FEA mesh node points of the machined part. This requires loading the FEA model of the part (shown in magenta in Figure 43) into the preprocessor in MAGMA and correctly positioning the final machined part into position overlapping the as-cast part. As the user manipulates the finite element mesh into place, MAGMAlink keeps track of the resulting transformation matrix (translations and rotations) necessary to transfer the porosity field between the casting simulation and the FEA mesh. Though not used in the current case study, MAGMAlink can transfer any other outputs from the casting simulation (i.e. residual stress, temperature history, microstructure, etc.). Here the FEA mesh is an ABAQUS input file (*.inp). After the FEA model is correctly positioned the porosity results are transferred to the FEA mesh as shown in Figure 44. A custom piece of software is used to remove error porosity values for nodes that fall outside of the casting which occur for example if weldments are added to the final part, or if data are poorly interpolated, and create the porosity field for analysis in ABAQUS and *fe-safe* by converting the % porosity values in MAGMAsoft to pore fraction values.

The porosity field at the FEA nodes is used in an elastic stress analysis simulation in ABAQUS using elastic properties that are locally dependent on the porosity at the nodes (Equs. 1 and 2). It was found that the stress field with porosity shown in Figure 45 is essentially unchanged from the "sound" material run. There is little or no stress redistribution since the regions with porosity are not highly stressed. The highest stressed locations are predicted to be sound in MAGMAsoft (see Figure 45). The subgrid model is applied next to develop the fatigue notch factor field that results from pore size in combination with the node spacing as shown in Figure 46. Finally the stress and K_f fields are imported into *fe-safe*, and the resulting life distribution in the part is predicted as shown in Figure 47. The fatigue life distribution in the part for sound material looks very similar to the part with porosity since the locations having $K_f \neq 1$ are in low stressed areas and still have much longer lives than the blue areas in Figure 47. Bear in mind that the life prediction by multiaxial strain-life methods is typically thought of as crack initiation life in a component. Therefore cracks can be expected to form at the lowest life points indicated in Figure 47 starting at around 5000 cycles (or possibly as low as 500 cycles

considering the plus minus one decade model verification results). It is recommended to monitor the areas of lowest life during part service for crack initiation and growth. Also, good toughness characteristics would be highly desirable in the steel used to resist this crack growth and extend the life of the part.

IV. CONCLUSION

A fatigue life prediction method using existing commercial software has been developed and applied to an example case study part. The fatigue model includes an adaptive subgrid technique which improves the model's ability to predict the detrimental effects of porosity which coarse computational grids cannot resolve. The model has been verified by comparing predicted results to measured fatigue life for specimens with average porosity distributions ranging between 8% and 22%. Measured and predicted fatigue lives for almost all 25 test specimens were found to fall with one decade; three were only slightly outside this range. This is taken in fatigue predictions as very good agreement.

ACKNOWLEDGEMENTS

This research was undertaken through the American Metalcasting Consortium (AMC). AMC is sponsored by Defense Supply Center Philadelphia (DSC, Philadelphia, PA) and the Defense Logistics Agency (DLA, Ft. Belvoir, VA). This work was conducted under the auspices of the Steel Founders' Society of America (SFSA) through substantial in-kind support and guidance from SFSA member foundries. Any opinions, findings, conclusions, or recommendations expressed herein are those of the authors and do not necessarily reflect the views of DSC, DLA, or the SFSA and any of its members.

The example casting case study fatigue predictions were performed under research sponsored by the U.S. Army Benet Laboratories and was accomplished under Cooperative Agreement Number W15QKN-06-R-0501. The views and conclusions contained in this document are those of the authors and should not be interpreted as representing the official policies, either expressed or implied, of U.S. Army Benet Laboratories or the U.S. Government. The U.S. Government is authorized to reproduce and distribute reprints for Government purposes notwithstanding any copyright notation heron.

REFERENCES

1. R.A. Hardin and C. Beckermann, "Simulation of the Mechanical Performance of Cast Steel with Porosity: Static Properties," in *Proceedings of the 60th Technical and Operating Conference*, SFSA, Chicago (2006).

2. R.A. Hardin, R.K. Huff and C. Beckermann, "Integrated Design of Steel Castings for Service Performance," *Modeling of Casting, Welding and Advanced Solidification Processes – XI*, ed. C. Gandin and M. Bellet, TMS, Warrendale, Pennsylvania, USA, 2006, pp. 653-660.

3. S.C. Haldimann-Sturm and A. Nussbaumer, “Fatigue Design of Cast Steel Nodes in Tubular Bridge Structures”, *International Journal of Fatigue*, 2007, article in press.

4. P. Li, D.M. Maijer, T.C. Lindley and P.D. Lee, “A Through Process Model of the Impact of In-Service Loading, Residual Stress, and Microstructure on the Final Fatigue Life of an A356 Automotive Wheel”, *Materials Science and Engineering A*, 2007, **460–461**, pp. 20–30.

5. X. Zhu, J.Z. Yi, J.W. Jones, and J.E. Allison, “A Probabilistic Model of Fatigue Strength Controlled by Porosity Population in a 319-Type Cast Aluminum Alloy: Part I. Model Development”, *Metallurgical and Materials Transactions A*, 2007, **38A**, pp. 1111-1122.

6. X. Zhu, J.Z. Yi, J.W. Jones, and J.E. Allison, “A Probabilistic Model of Fatigue Strength Controlled by Porosity Population in a 319-Type Cast Aluminum Alloy: Part II. Monte-Carlo Simulation”, *Metallurgical and Materials Transactions A*, 2007, **38A**, pp. 1123-1135.

7. P. Baicchi, L. Collini, E. Riva, “A Methodology for the Fatigue Design of Notched Castings in Gray Cast Iron”, *Engineering Fracture Mechanics*, 2007, **74**, pp. 539–548.

8. J. Linder, M. Axelsson and H. Nilsson, “The Influence of Porosity on the Fatigue Life for Sand and Permanent Mould Cast Aluminium”, *International Journal of Fatigue*, 2006, **28**, pp. 1752–1758.

9. Y. Nadot, J. Mendez and N. Ranganathan, “Influence of Casting Defects on The Fatigue Limit of Nodular Iron”, *International Journal of Fatigue*, 2004, **26**, pp. 311–319.

10. Y. Nadot and V. Denier, “Fatigue Failure of Suspension Arm: Experimental Analysis and Mutliaxial Criterion”, *Engineering Failure Analysis*, 2004, **11**, pp. 485-499.

11. D.L. McDowell, K. Gall, M.F. Horstemeyer, and J. Fan, “Microstructure-Based Fatigue Modeling of Cast A356-T6 Alloy”, *Engineering Fracture Mechanics*, 2003, **70(1)**, pp. 49-80.

12. M.F. Horstemeyer, N. Yang, K. Gall, D.L. McDowell, J. Fan, and P.M. Gullett, “High Cycle Fatigue of a Die Cast AZ91E-T4 Magnesium Alloy”, *Acta Materialia*, 2004, **52(5)**, pp. 1327-1336.

13. T. Mansson, F. Nilsson, “Fatigue Life Estimation of Cast Components”, *International Journal of Cast Metals Research*, 2001, **13(6)**, pp. 373-378.

14. P. Hausild, C. Berdin, P. Bompard, N. Verdiere, “Influence of Shrinkage Cavities on Fracture Behaviour of Duplex Stainless Steel”, *Materials Science and Engineering A*, 2002, **335(1-2)**, 164-174.

15. K.M. Sigl, R. Hardin, R.I. Stephens, and C. Beckermann, “Fatigue of 8630 Cast Steel in the Presence of Porosity,” *International Journal of Cast Metals Research*, 2004, 17(3), pp. 130-146.

16. Y. Murakami, *Metal Fatigue: Effects of Small Defects and Nonmetallic Inclusions*, (Elsevier Science Ltd., Oxford, 2002).

17. Sigl, K.M., Hardin, R., Stephens, R.I., and Beckermann, C., "Fatigue of 8630 Cast Steel in the Presence of Shrinkage Porosity," in Proceedings of the 57th Technical and Operating Conference, SFSA, Chicago (2003).

18. Standard E606, "Standard Practice for Strain-Controlled Fatigue Testing", *2002 Annual Book of ASTM Standards* (American Society of Testing and Materials, West Conshohocken, PA 2002), **Vol. 03.01**, pp. 569-583.

19. R. I. Stephens, *Fatigue and Fracture Toughness of Five Carbon or Low Alloy Cast Steels at Room or Low Climatic Temperatures* (Carbon and Low Alloy Technical Research Committee, Steel Founders' Society of America, Des Plaines, IL, 1982).

20. Hardin, R. and Beckermann, C., "Effect of Porosity on Mechanical Properties of 8630 Cast Steel," in Proceedings of the 58th Technical and Operating Conference, SFSA, Chicago (2004).

21. W. Rasband: *ImageJ 1.35p*, National Institutes of Health, USA.

22. A.C. Kak and M. Slaney: *Principles of Computerized Tomographic Imaging*, (Soc. for Ind. and App. Mathematics, 2001, pp. 275-296).

23. *IMSL Fortran Subroutines for Mathematical Applications: Math/Library Volumes 1 and 2*, Visual Numerics, Inc., 1997.

24. Roberts, A.P., and Garboczi, E.J., "Elastic Properties of Model Porous Ceramics," *J. Am. Ceram. Soc.*, 2000, 83(12), pp. 3041-3048.

25. *ABAQUS/Standard*, ABAQUS, Inc., Providence, RI, 2006.

26. R. I. Stephens, A. Fatemi, R. R. Stephens, H. O. Fuchs, *Metal Fatigue in Engineering* (2nd Edition, Wiley-Interscience, New York, 2000).

27. *fe-safe User Manual*, Safe Technology Ltd., 2006, pp. 233-239.

28. D.F. Socie and G.B. Marquis, *Multiaxial Fatigue*, Society of Automotive Engineers, 2000.

29. R. E. Peterson, *Stress Concentration Factors* (Wiley-Interscience, New York, 1974), p. 137.

30. Carlson, K., Ou, S., Hardin, R. and Beckermann, C., "Analysis of ASTM X-ray Shrinkage Rating for Steel Castings," in *Proceedings of the 54th Technical and Operating Conference*, SFSA, Chicago (2000).

Table I. Experimental measurements from fatigue testing [17] test stress level, porosity measurement from radiographic analysis, measured strain and elastic modulus, and fatigue life.

		Porosity Fraction Measured from Radiographs		Strain*10^4	Elastic Modulus (GPa)	Fatigue Life (Cycles)
Specimen Number	Applied Stress Level of Test (MPa)	Average in Gage Section	Maximum Cross-section	Measured	Measured	Measured
1	96	0.104	0.432	7.01	137	1,365
2	96	0.101	0.208	6.44	149	79,908
3	126	0.101	0.256	8.81	143	24,320
4	53	0.128	0.297	3.84	138	851,275
5	126	0.097	0.185	8.24	153	29,023
6	66	0.134	0.275	4.55	145	216,516
7	66	0.095	0.201	4.68	141	4,053,800
8	66	0.185	0.363	4.89	135	57,566
9	53	0.146	0.587	6.09	87	10,812
10	126	0.213	0.326	9.33	135	37,089
11	66	0.117	0.250	4.85	136	113,503
12	66	0.148	0.415	5.84	113	15,419
13	96	0.185	0.538	12.47	77	6,042
14	126	0.139	0.507	10.50	120	160
15	53	0.187	0.551	6.09	87	15,868
16	66	0.076	0.160	3.98	166	1,681,018
17	96	0.096	0.254	8.65	111	4,392
18	53	0.085	0.148	3.66	145	1,342,218
19	126	0.093	0.225	8.87	142	13,013
20	53	0.099	0.182	3.71	143	249,752
21	96	0.122	0.300	7.68	125	41,066
22	66	0.117	0.262	4.37	151	769,074
23	126	0.121	0.205	8.13	155	40,896
24	96	0.144	0.288	6.76	142	333,025
25	126	0.129	0.280	8.51	148	7,456

Table II - 8630 Steel Monotonic Properties [19].

Property	Sound Material
S_u (MPa)	1 144
S_y (MPa)	985
E (GPa)	207
%EL	Not Measured
%RA	29
σ_f (MPa)	1 268
ε_f	0.35
K (MPa)	Not Measured
n	Not Measured

Table III - 8630 Steel Cyclic Properties [19].

Property	Sound Material
S_f (MPa)	293
S_f/S_u	0.26
K' (MPa)	2 267
n'	0.195
S_y' (MPa)	661
b	-0.121
c	-0.693
σ_f' (MPa)	1 936
ε_f'	0.42

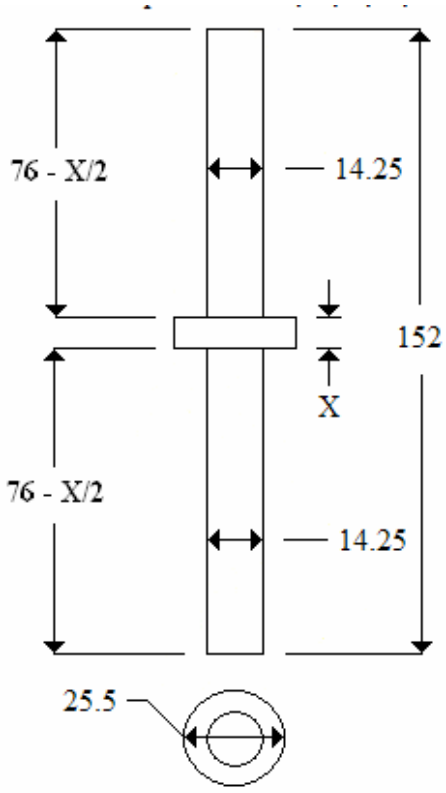

Porous Specimen Blanks

Fig. 1 - Dimensions of cast blanks in millimeters. Dimension “X” = 5, 7.5, and 10 mm for the “least”, “middle”, and “most” porosity specimen groups respectively.

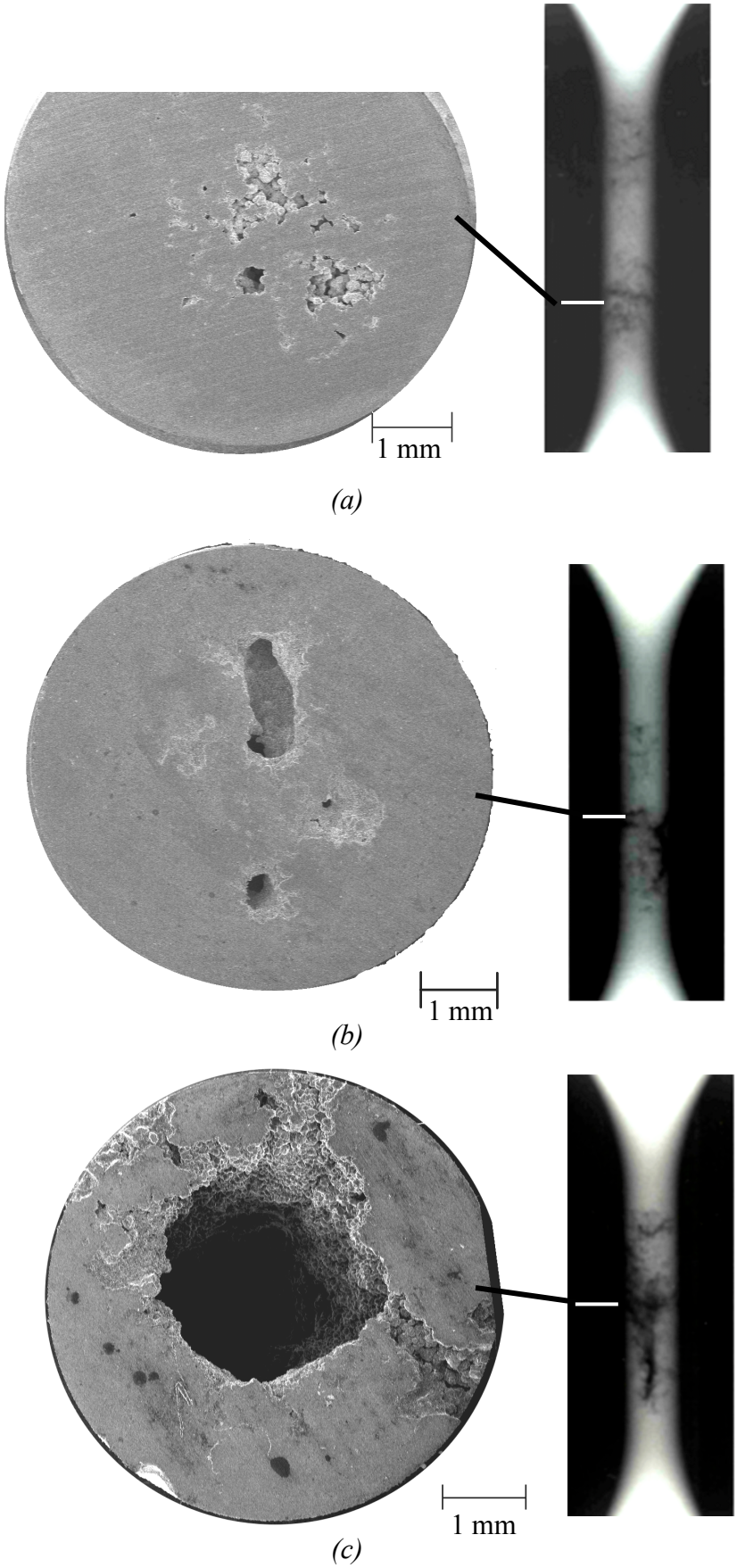

Fig. 2—Cut and polished surfaces of three specimens cast with different porosity levels ranging from *(a)* Specimen 22 representing the least, to *(b)* Specimen 3 representing the middle range, to *(c)* Specimen 13 representing the most porosity. Radiographs of the specimen gage sections are given to the right of each surface with the longitudinal position of the cut indicated.

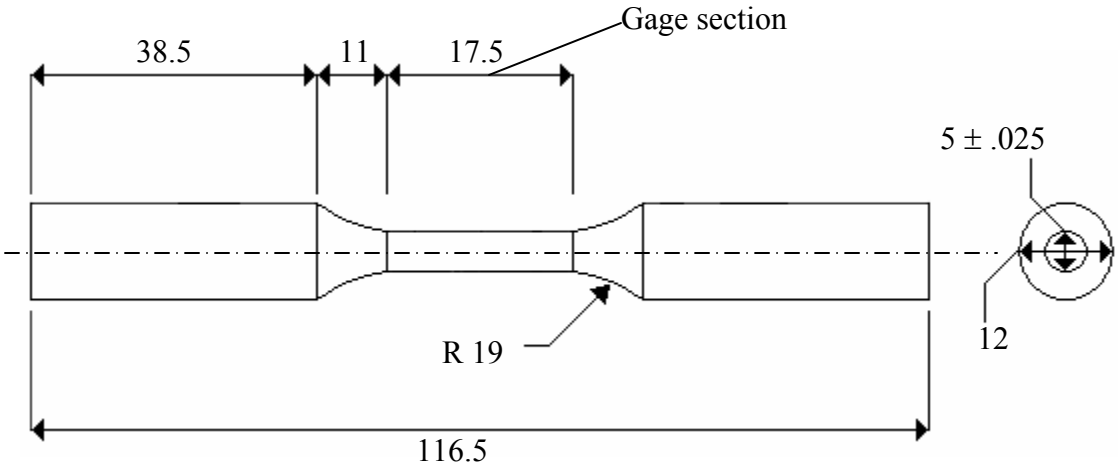

(a)

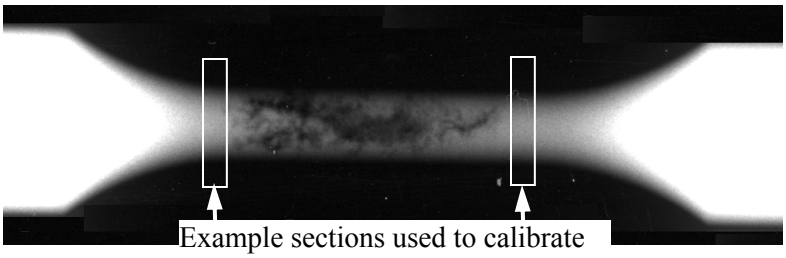

(b)

Fig. 3—*(a)* Dimensions of test specimens in millimeters; *(b)* Radiograph of test specimen with sections of sound material used to calibrate gray level intensity to section thickness indicated.

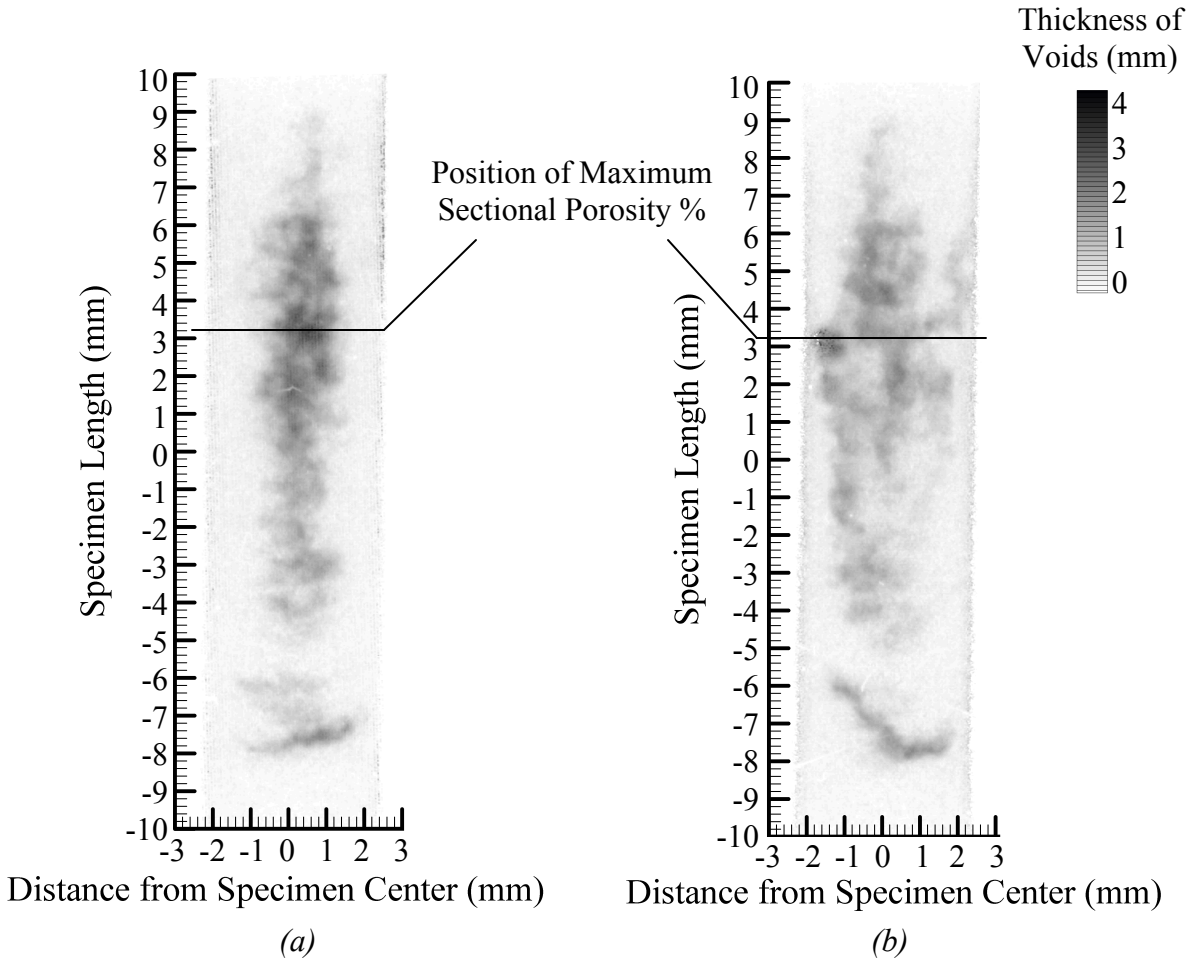

Fig. 4—*(a)* Digitized radiograph of Specimen 3, View 1; *(b)* Second radiographic view of same specimen taken after rotating 90 degrees about lengthwise axis, View 2.

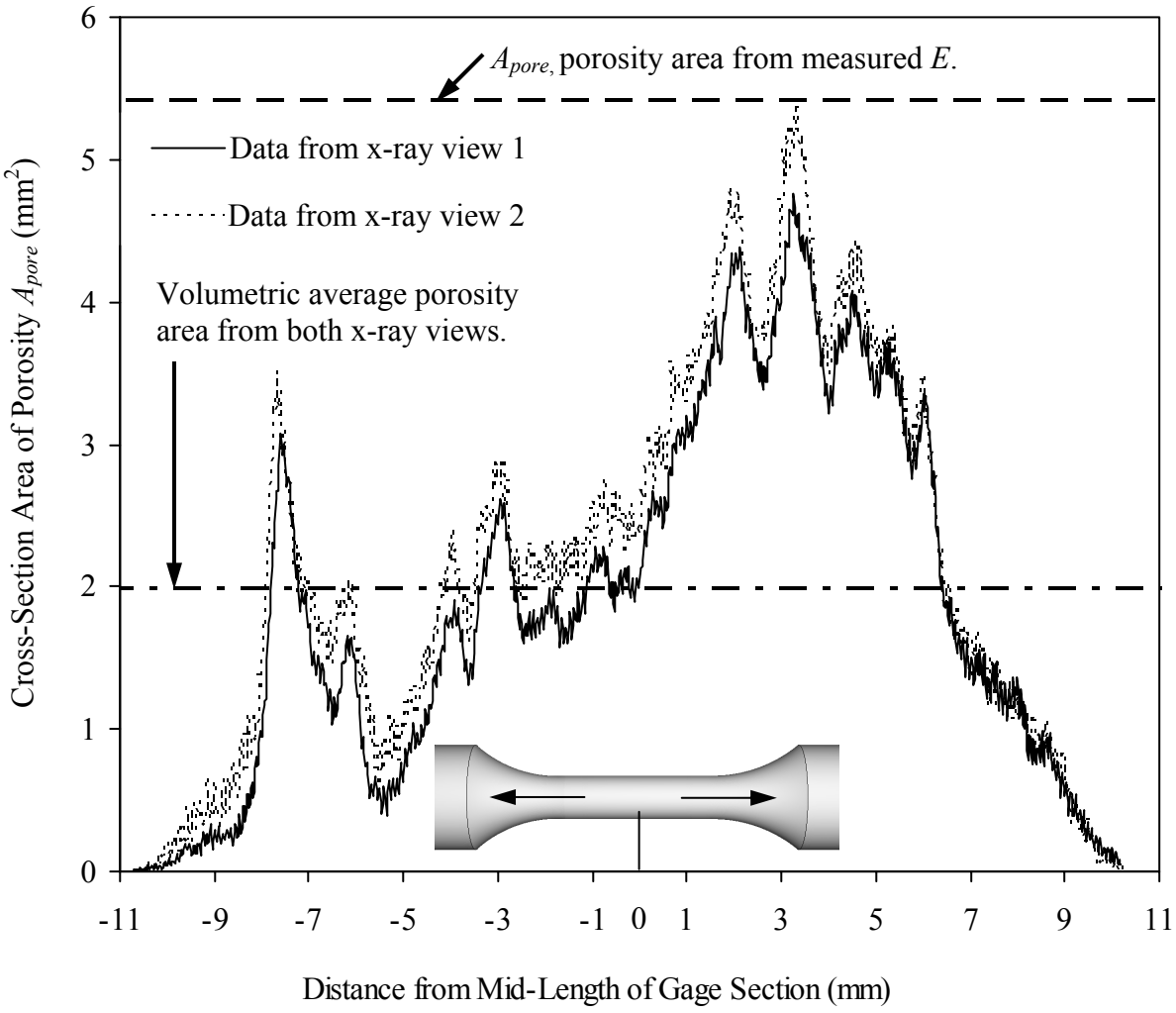

Fig. 5—Cross-sectional area of porosity versus lengthwise axis position of Specimen 3, position referenced to center of specimen length for the two radiographic views that are shown in Fig. 4. Volumetric average porosity and effective porosity area determined from measured modulus are indicated for comparison.

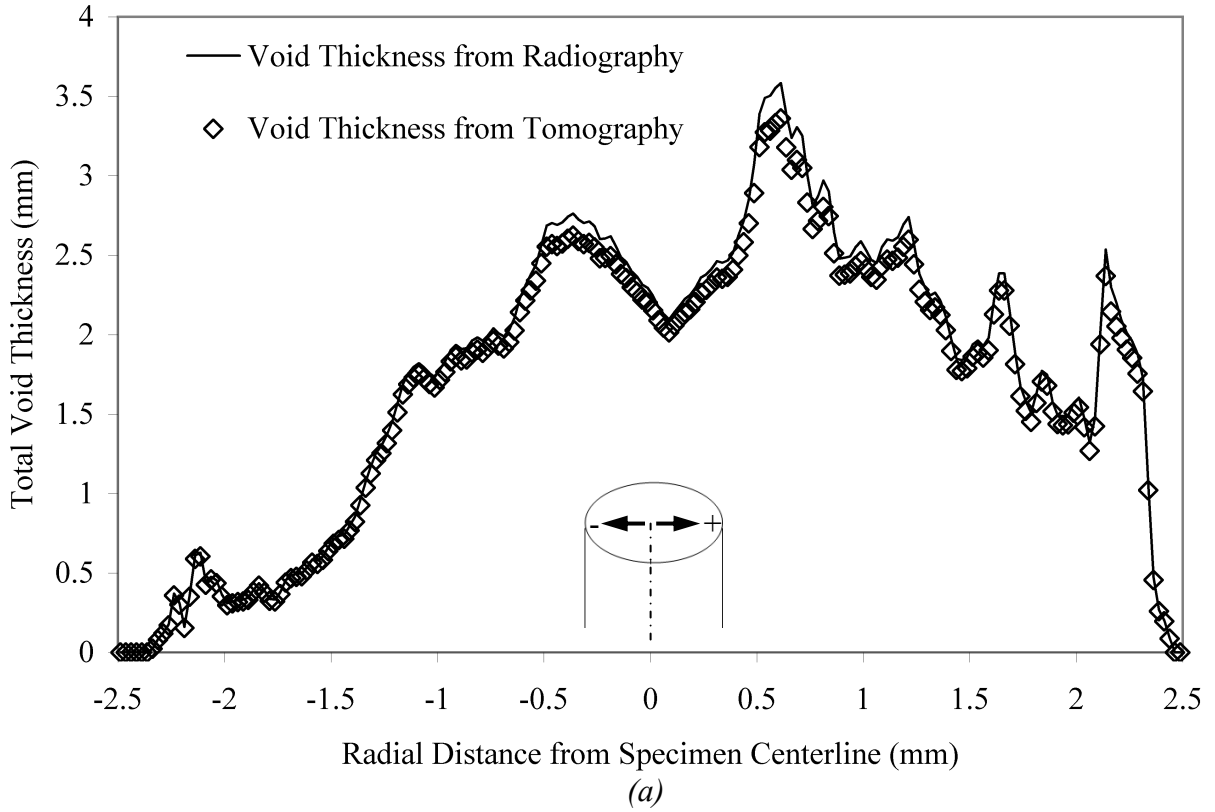

(a)

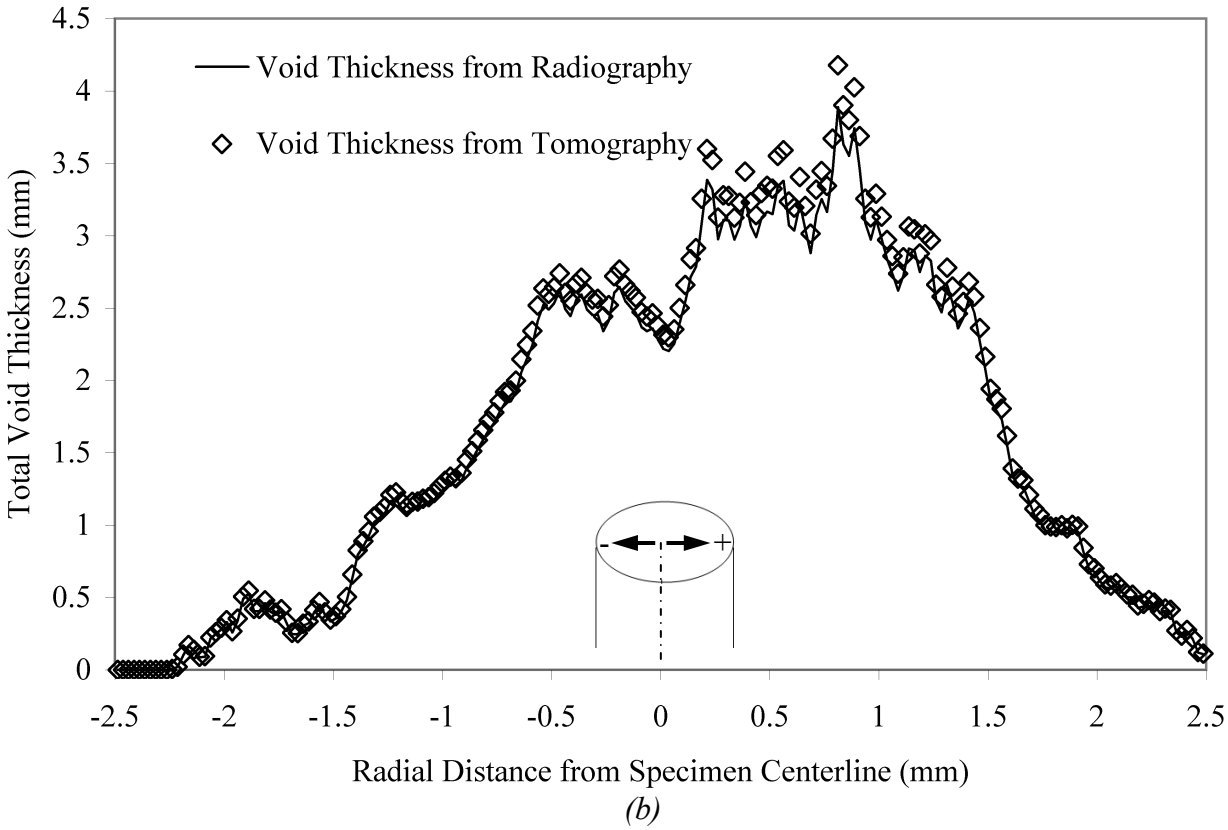

(b)

Fig. 6—Comparison between the total void dimension of the porosity determined from the radiograph and resulting from the tomographic reconstruction of the porosity for two radiographic views *(a)* and *(b)*. Data is from a lengthwise position in the specimen gage section across the specimen diameter.

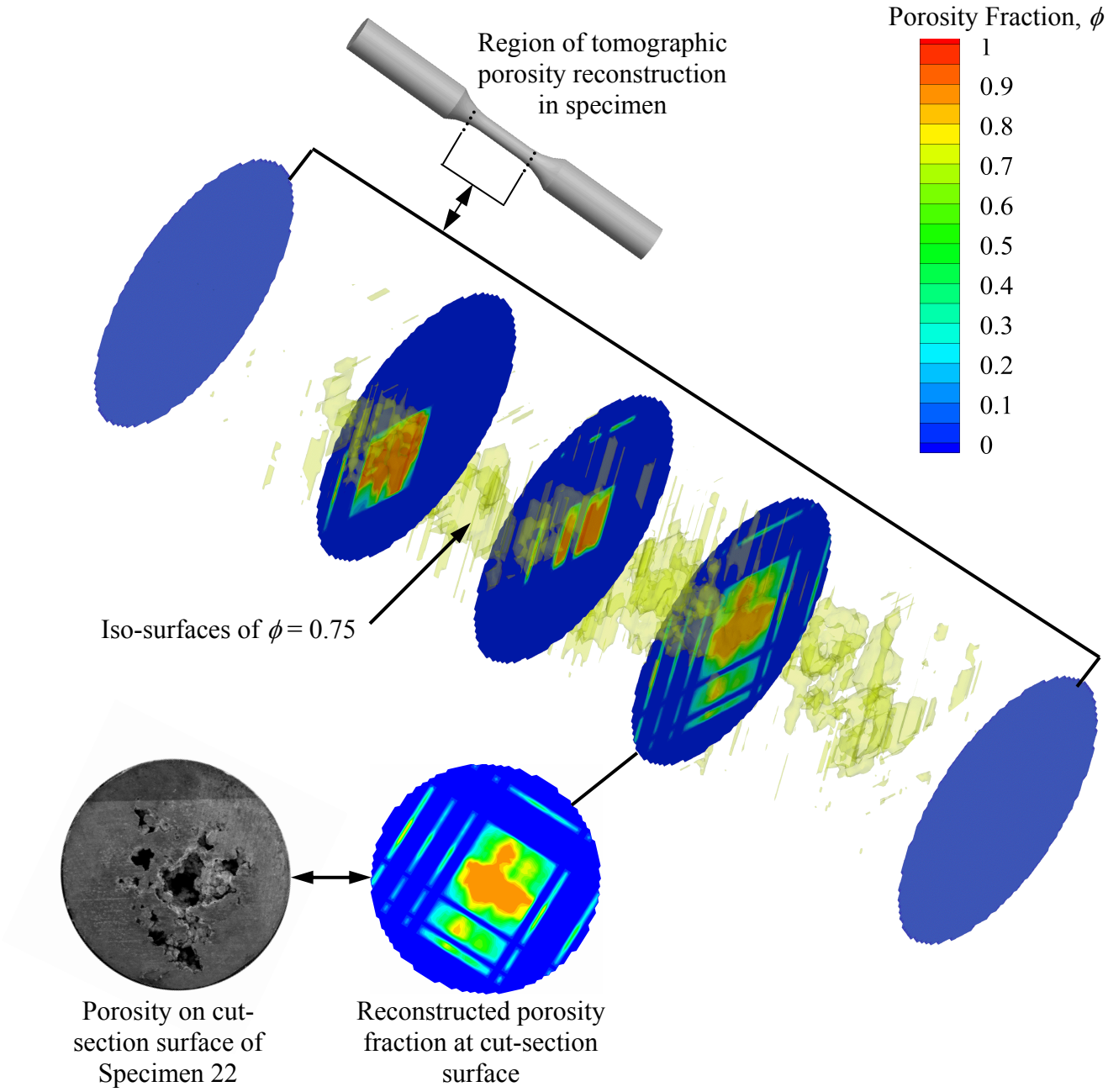

Fig. 7—Example of internal porosity distribution reconstructed from x-ray tomography in the test section of a fatigue test specimen, Specimen 22. Slice of the 3-D porosity field from tomography is compared to a cut specimen surface at the same lengthwise position.

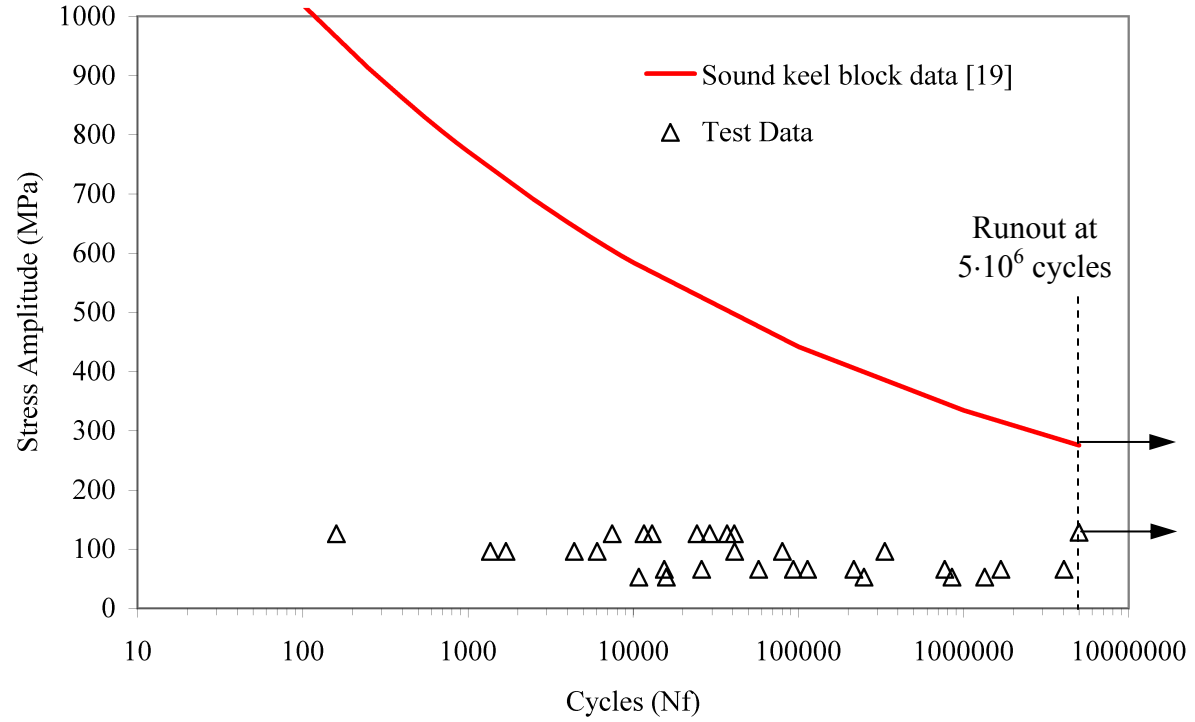

Fig. 8 — Fatigue test data of specimens with porosity compared with sound data from [19].

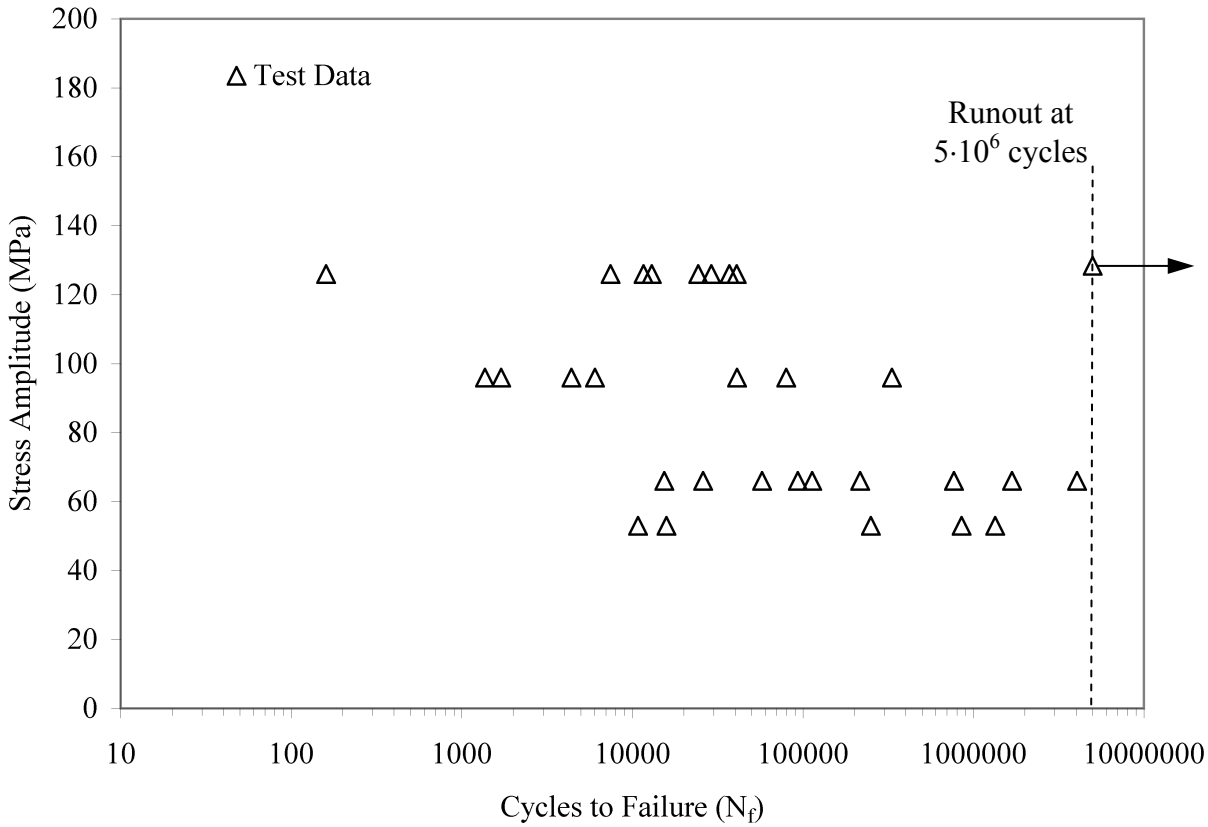

Fig. 9 — Fatigue test data of specimens with porosity tested at three stress levels 126, 96, 66, and 53 MPa. Note the single runout specimen.

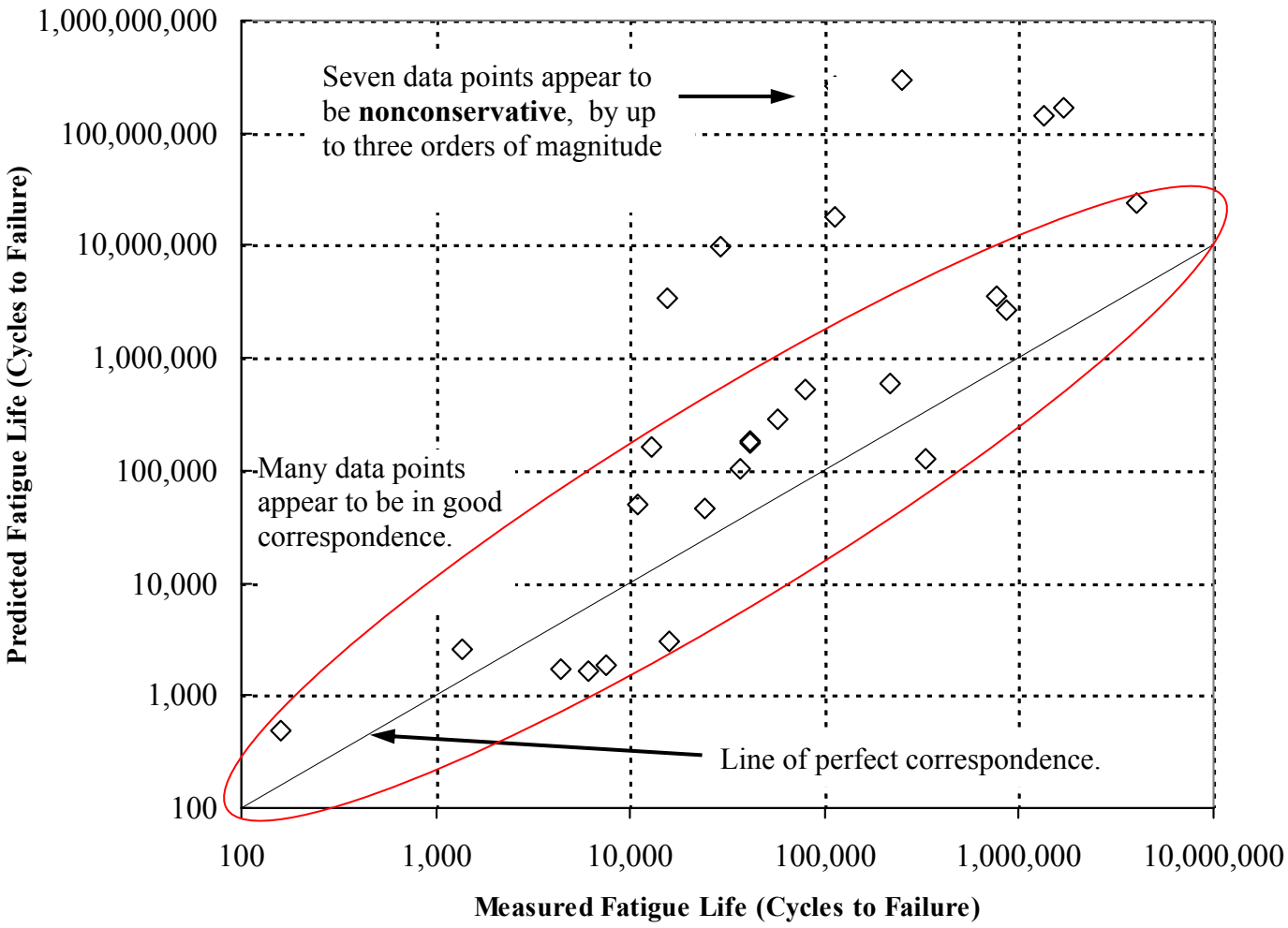

Fig 10 — Comparison between measured and predicted fatigue lives of specimens for node spacing ≈ 0.25 mm. Prediction used ABAQUS simulated stress field and sound fatigue properties from Table III in fe-safe multi-axial Brown-Miller algorithm with Morrow mean stress correction. Predicted life is taken as the smallest life in the fe-safe calculation.

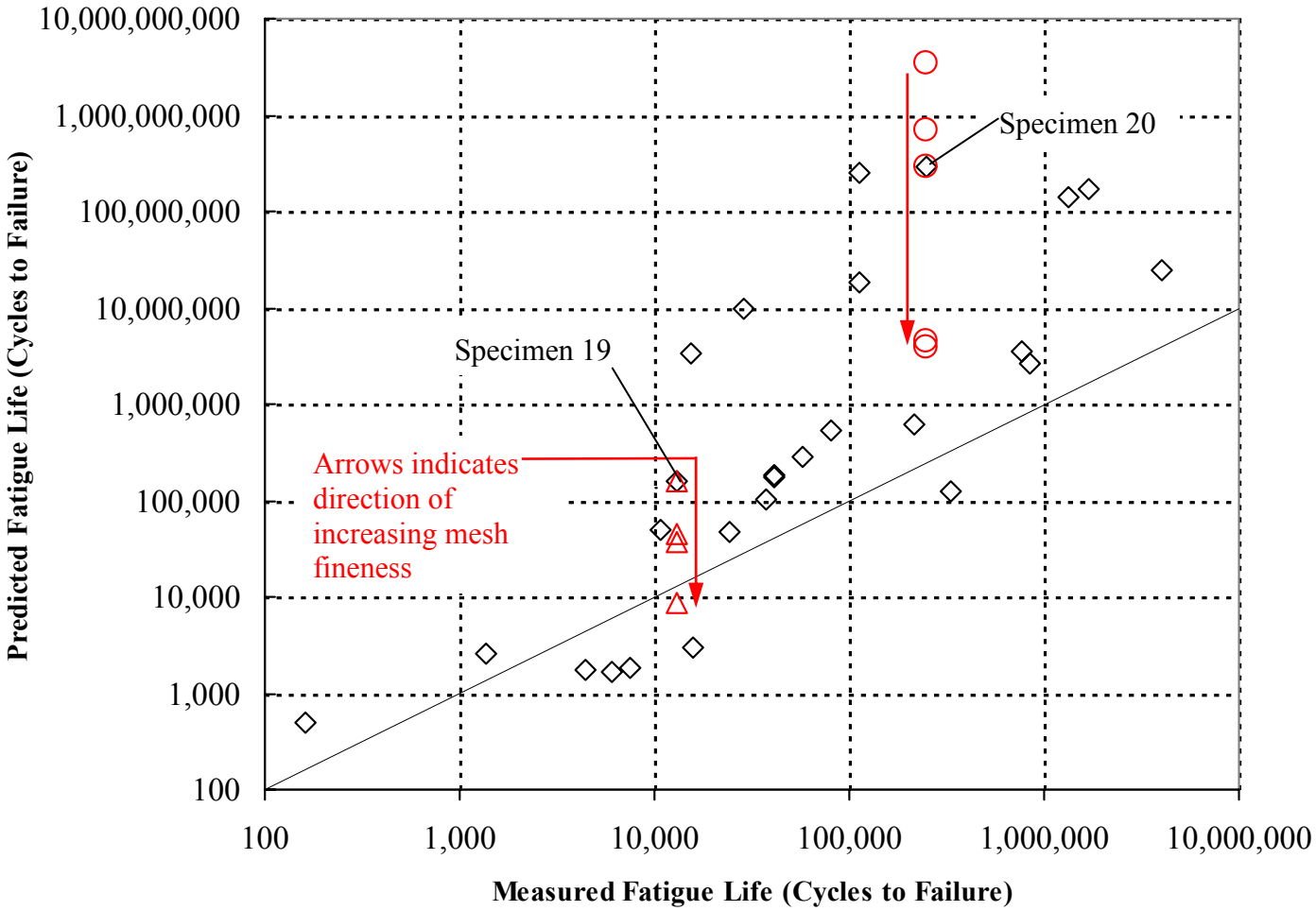

Fig. 11 — Comparison between measured and predicted fatigue lives of specimens shown in Fig. 10 with additional runs made for additional runs for Specimen 19 at three finer grids, and at two coarser and three finer finite element mesh grids for Specimen 20.

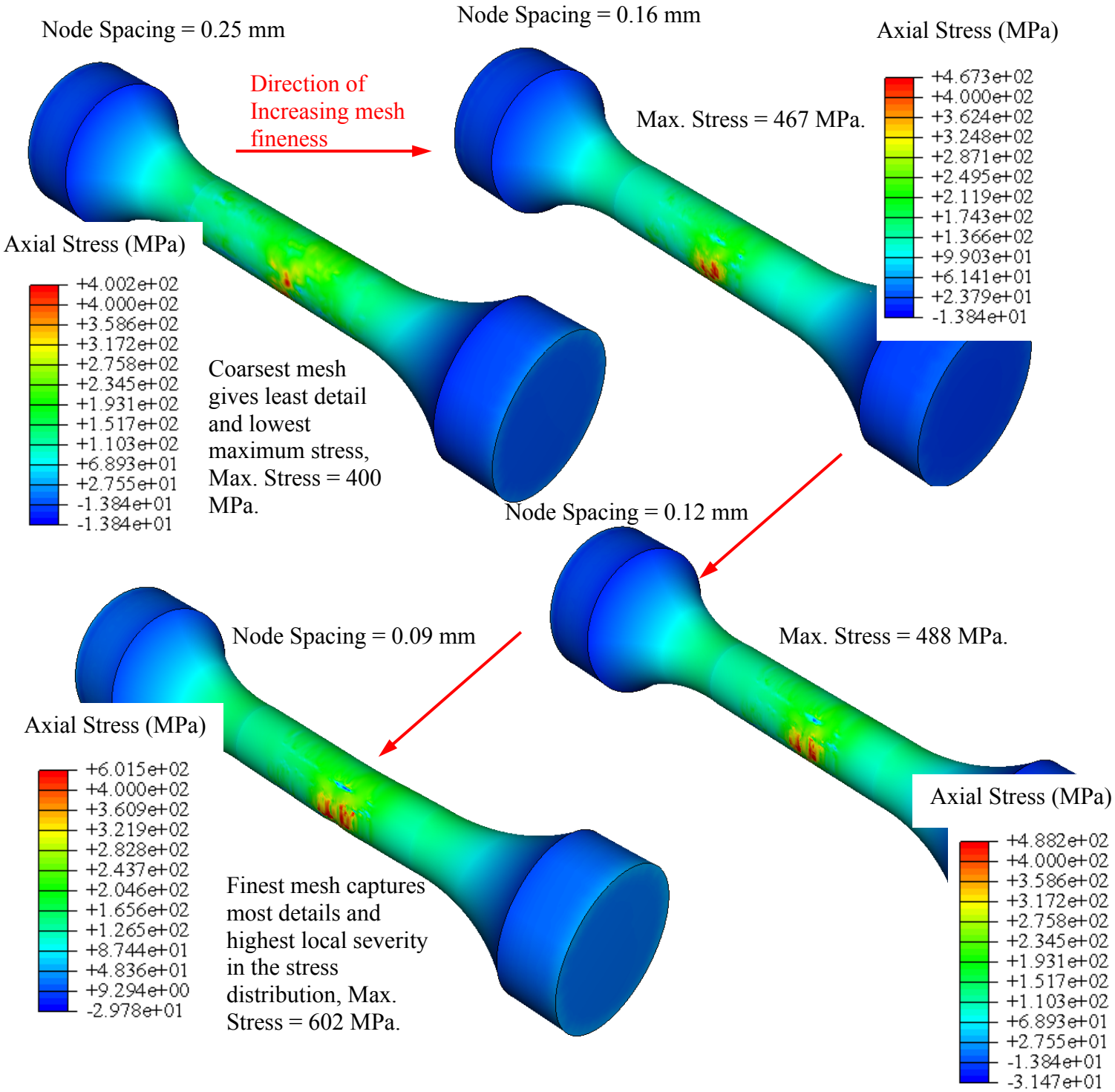

Fig. 12 — Stress results for the four grids used to simulate Specimen 19 shown in Fig. 11. Finer grids give higher stresses from more detailed porosity field.

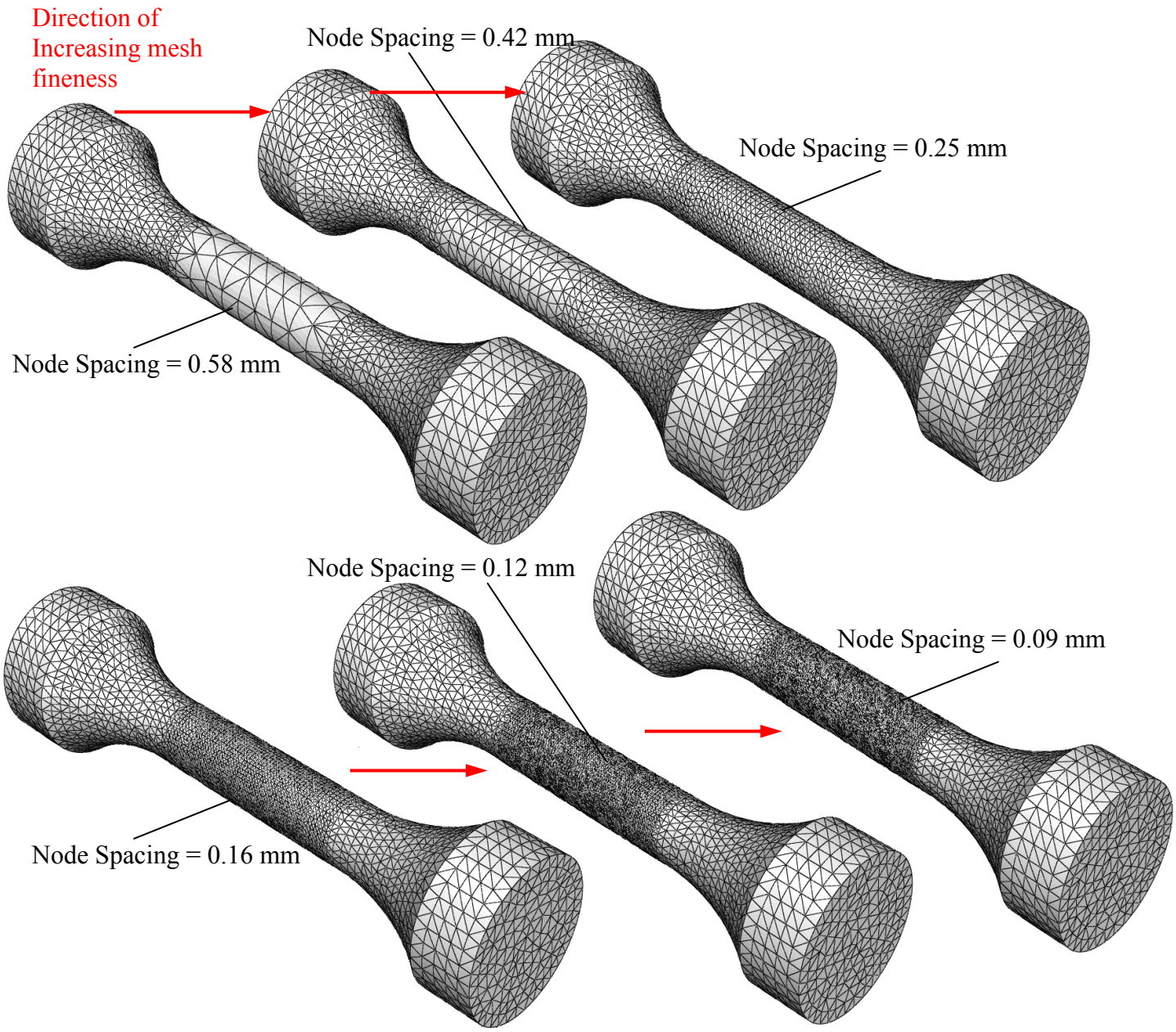

Fig. 13 — Visual comparison of the six finite element meshes used in the grid studies from Figs. 14 and 15.

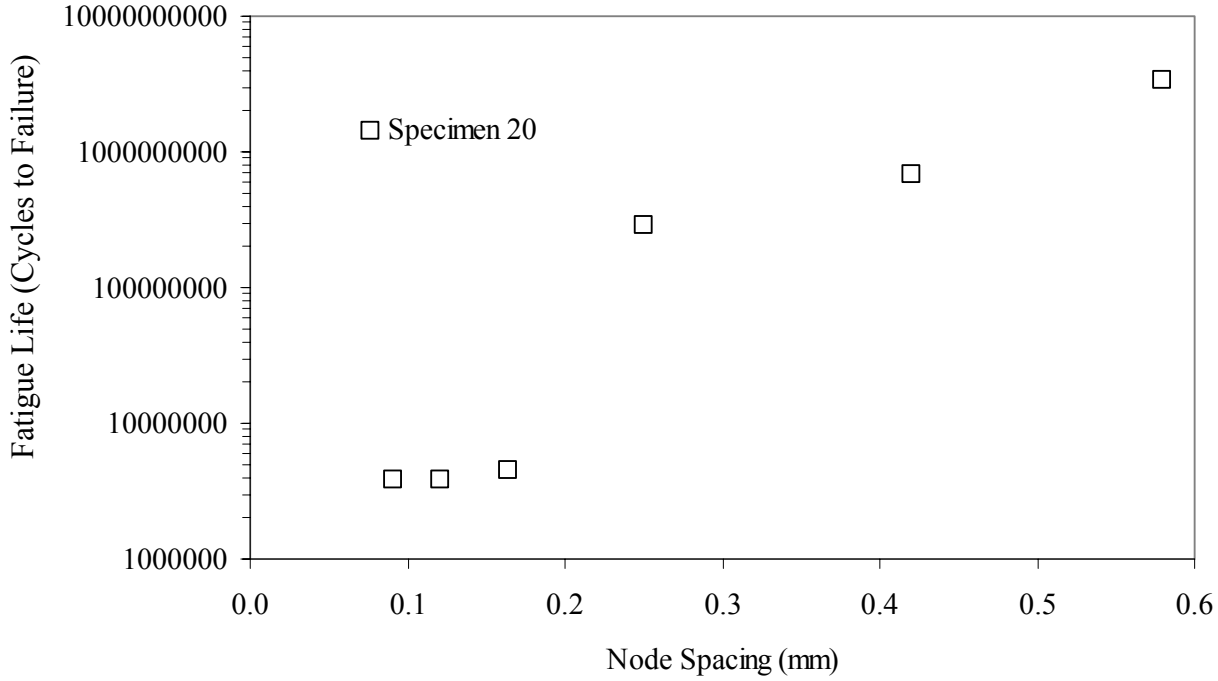

Fig. 14 — Effect of finite element model node spacing on predicted fatigue life for Specimen 20.

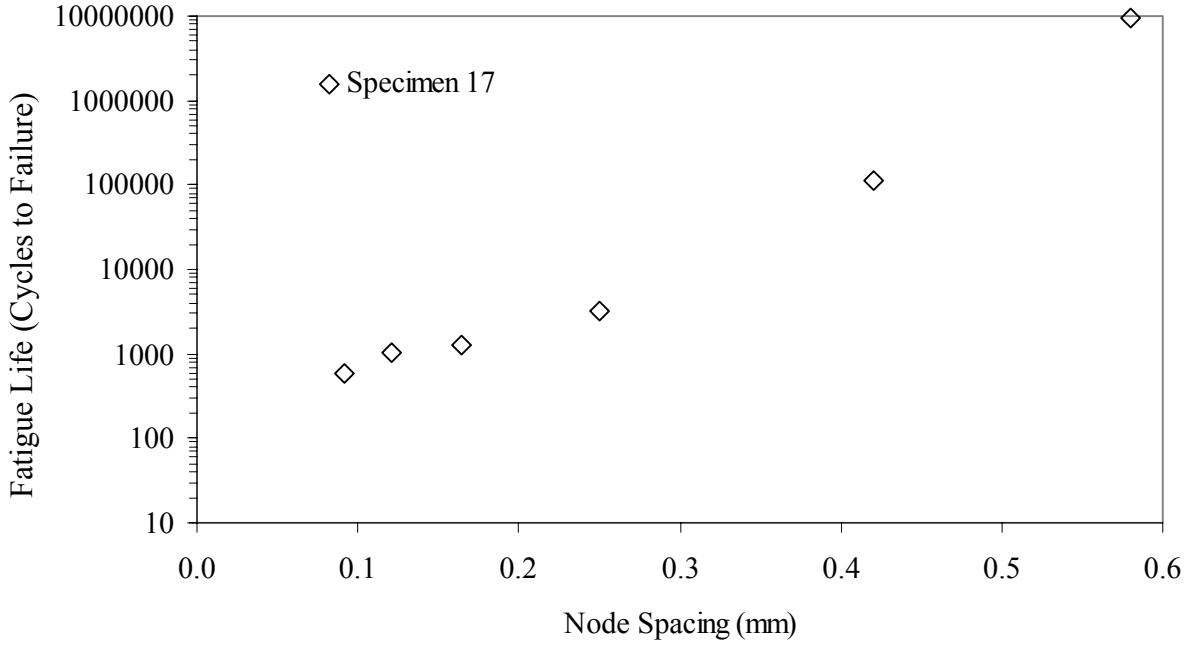

Fig. 15 — Effect of finite element model node spacing on predicted fatigue life for Specimen 17.

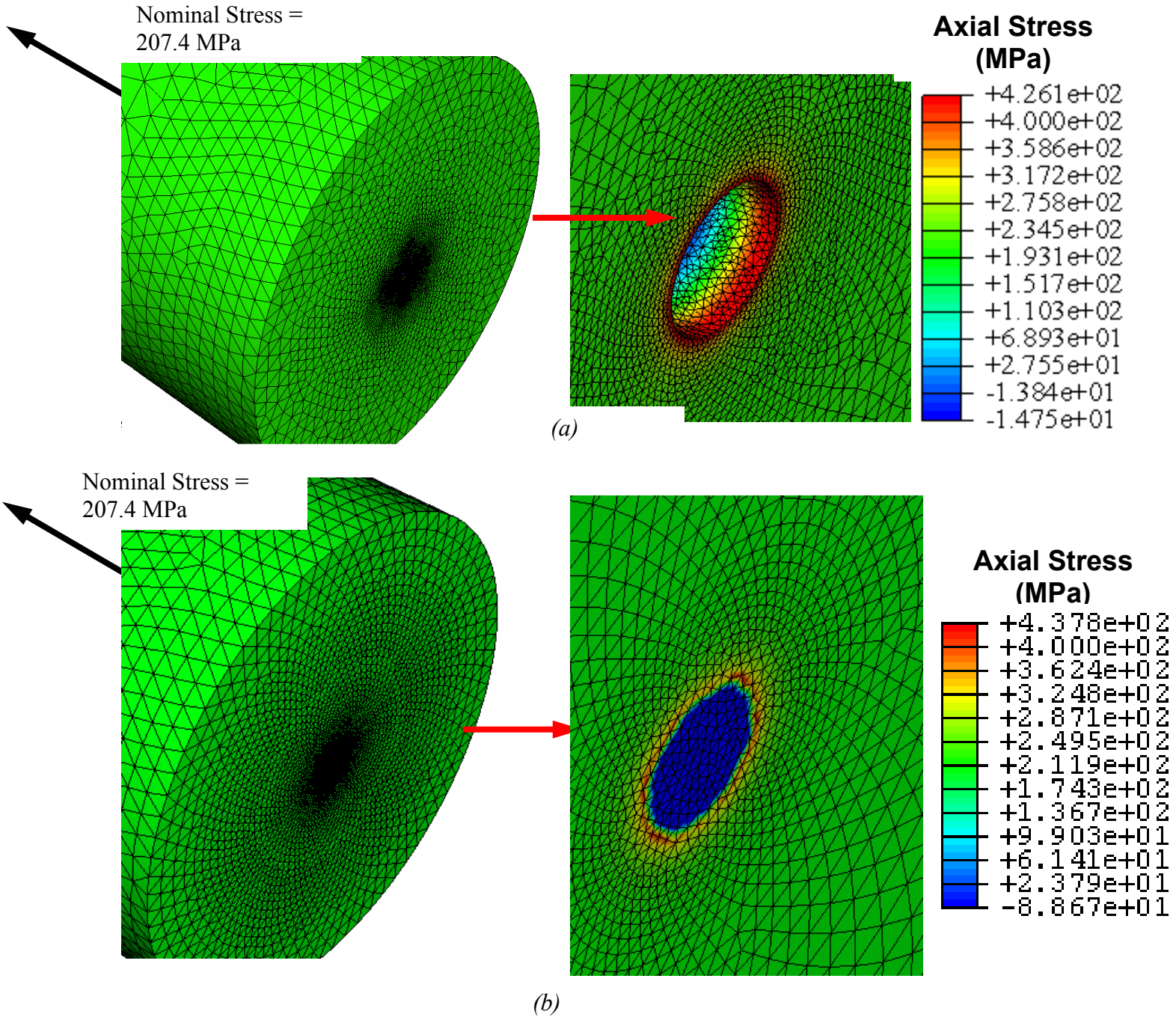

Fig. 16 — ABAQUS stress results for a 0.2 mm diameter spherical hole in a 5 mm diameter cylinder with 207 MPa applied nominal stress. Half symmetry is used to model *(a)* hole as a feature meshed in the model gives a maximum stress = 426 MPa and *(b)* hole as a porosity field (pore fraction = 1) giving a maximum ABAQUS stress = 438 MPa both of which are close to the maximum handbook calculation 424 MPa.

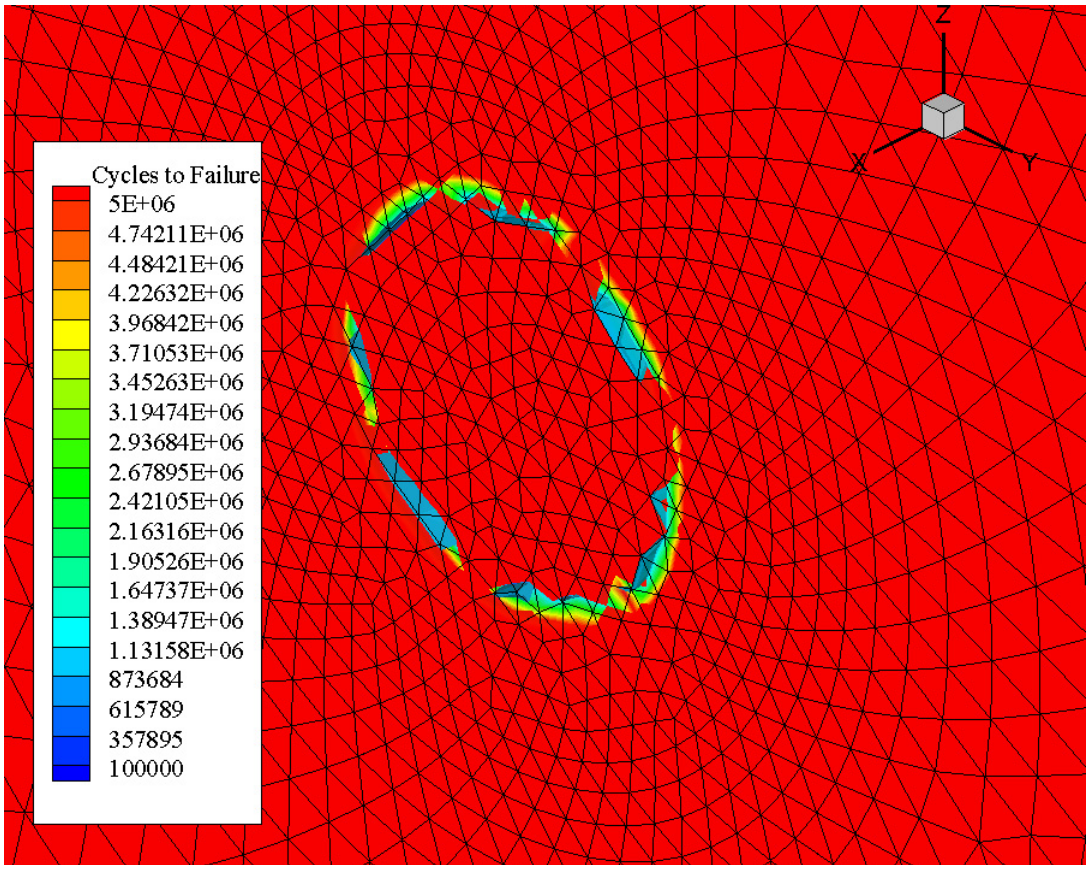

Fig. 17 — Predicted life for stress field in Fig. 16 *(b)* from fe-safe cycles to failure for fully reversed loading (R = -1) at 207 MPa for a spherical shaped porosity field having 100% porosity with radius 0.2 mm. Shortest predicted life here is 135,330 cycles and hand calculation is 138,425 cycles.

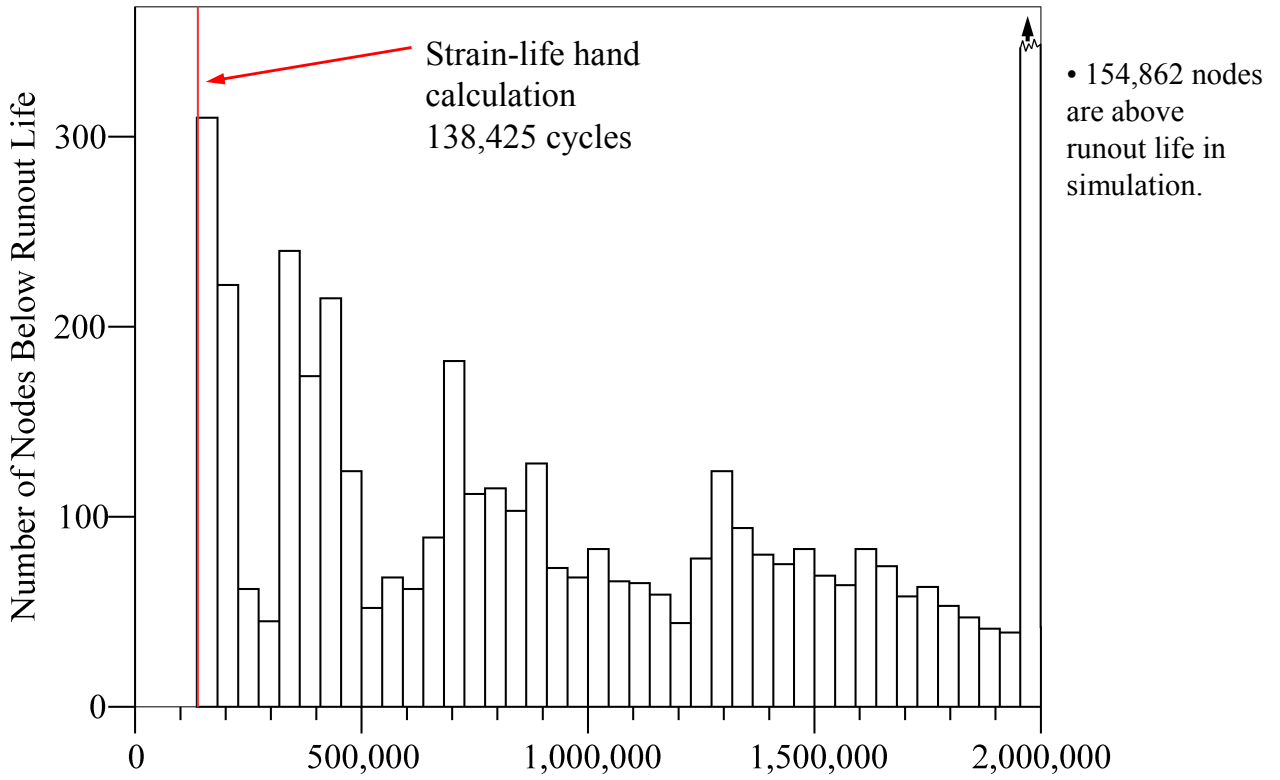

Fig. 18 — Predicted life distribution below runout from fe-safe for stress field in Fig. 16 *(a)* for hole modeled as a feature. Shortest life is 159,210 cycles. Hand calculation life indicated in histogram.

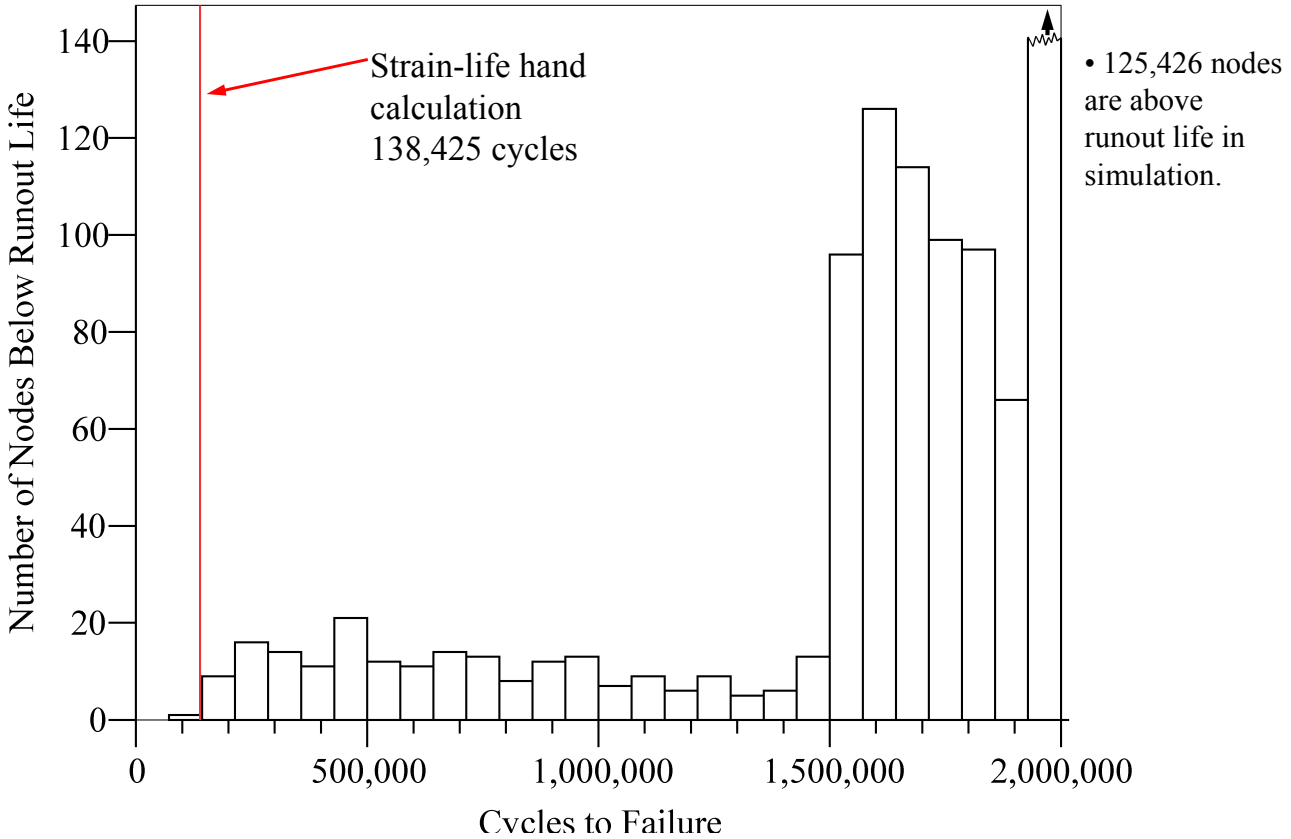

Fig. 19 — Predicted life distribution below runout from fe-safe for stress field in Fig. 16 *(b)* for hole modeled as a porosity field. Shortest life is 135,330 cycles. Hand calculation life indicated in histogram.

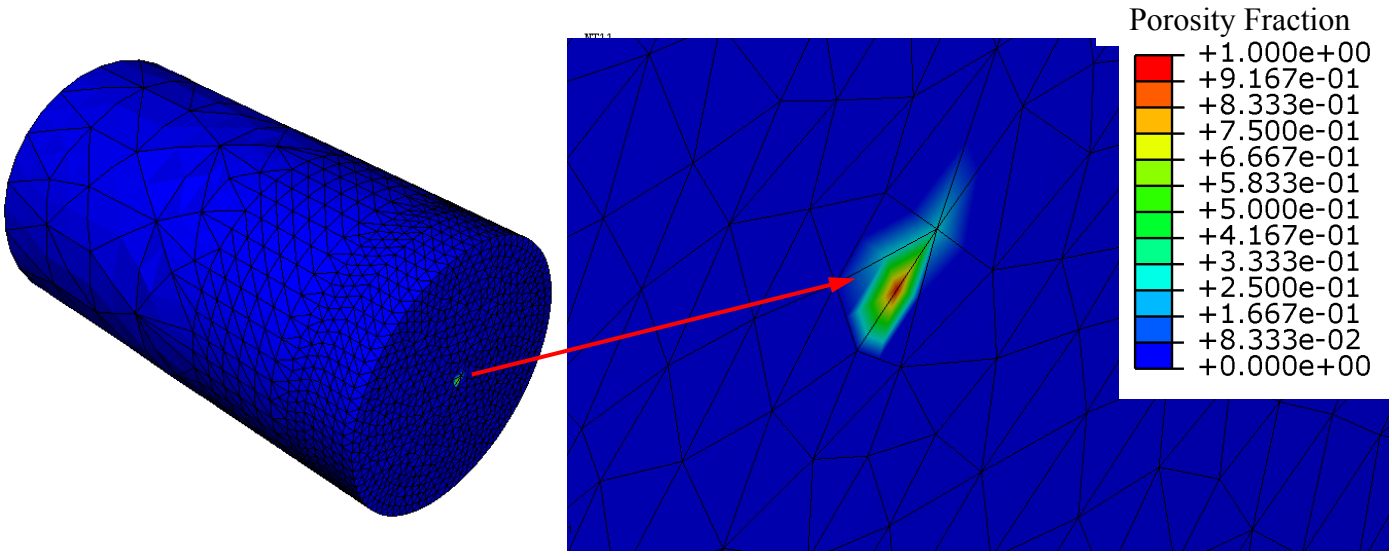

Fig. 20 — Example of porosity field for mesh study is a coarse 0.2 mm grid spacing of the 0.2 mm diameter hole. Node spacing is approximately ½ the grid spacing.

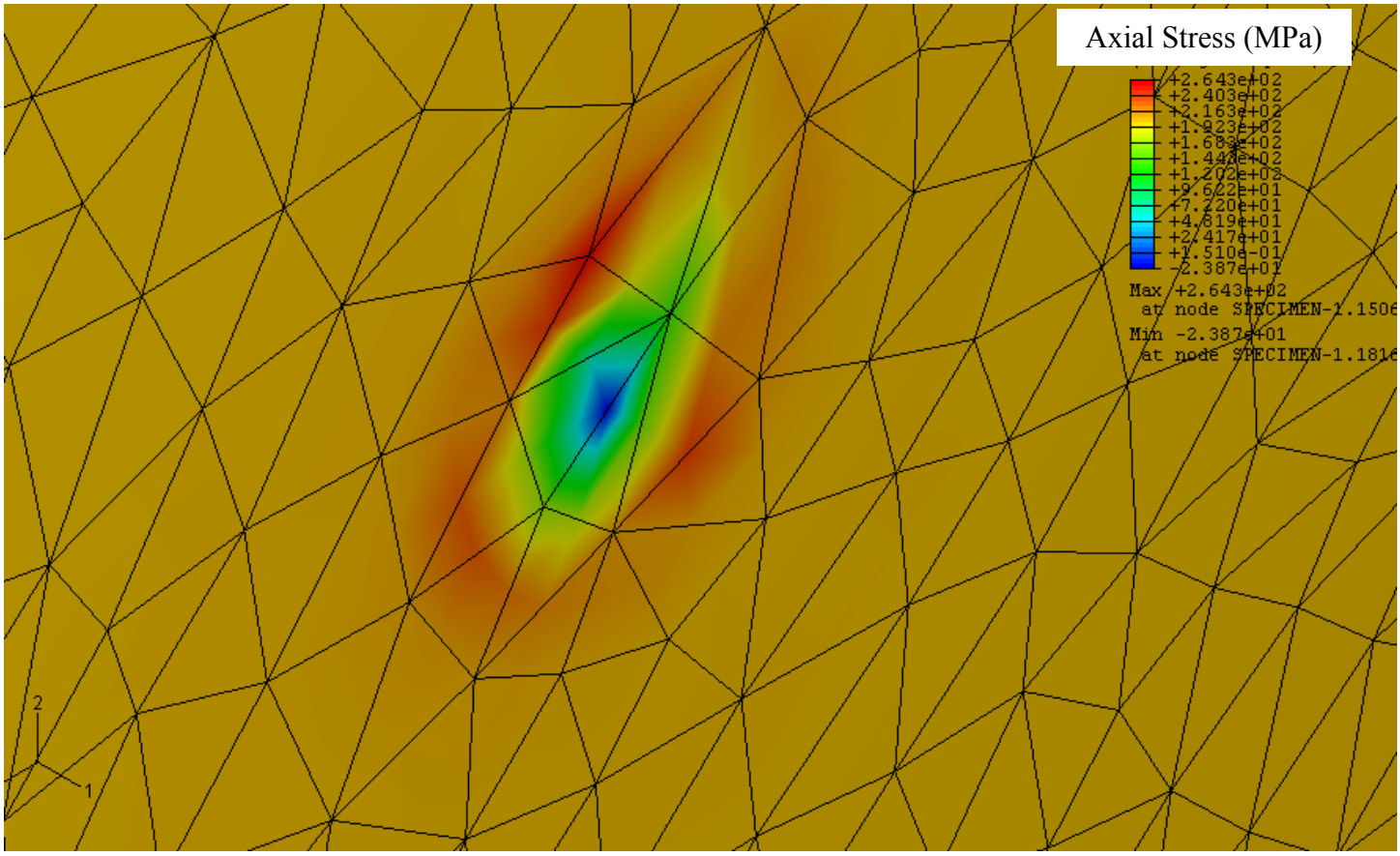

Fig. 21 — Resulting stress field for porosity shown in Fig. 21 (0.2 mm grid spacing and 0.2 mm diameter hole). Maximum ABAQUS stress = 264 MPa, and K_t = 1.61 to achieve actual maximum

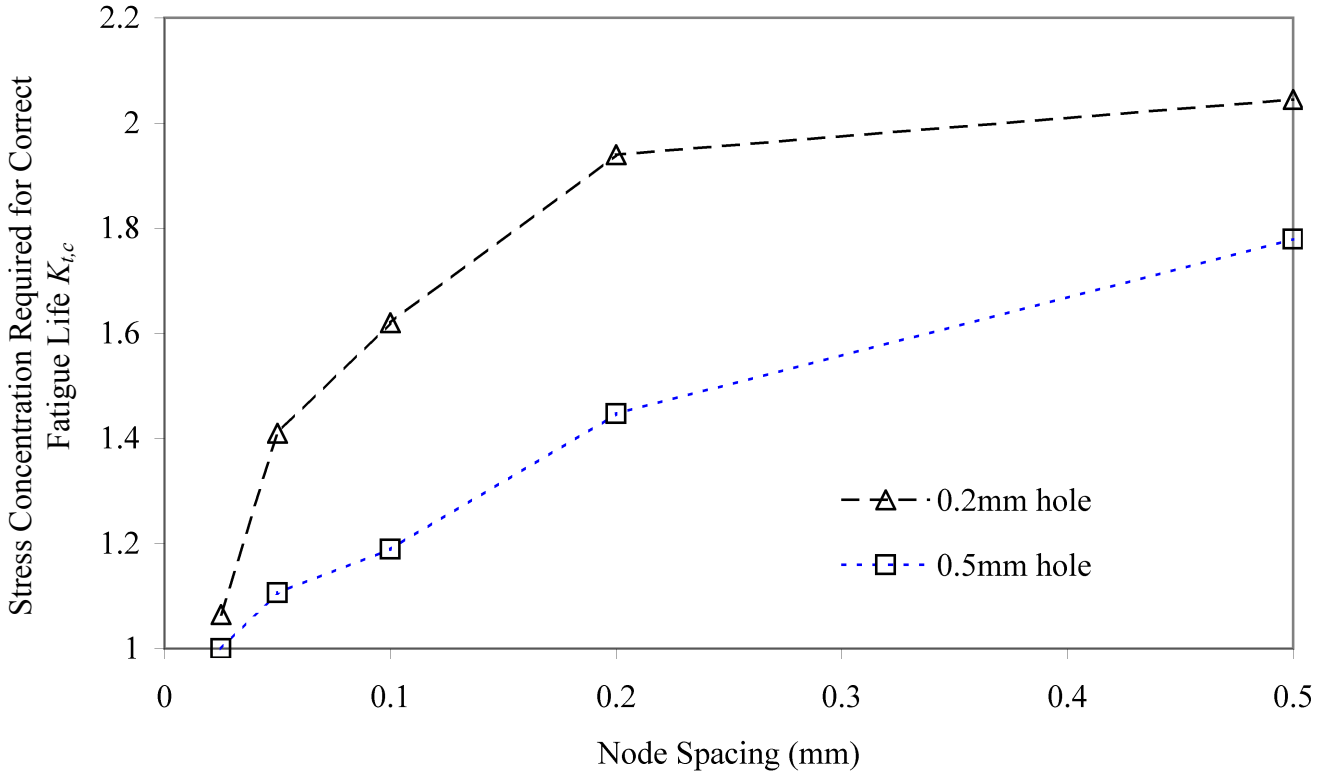

Fig. 22 — Stress concentration $K_{t,c}$ required to achieve correct fatigue life at five nodes spacings (approximately ½ the element grid spacing) for 0.2 and 0.5 mm diameter spherical holes modeled using porosity field.

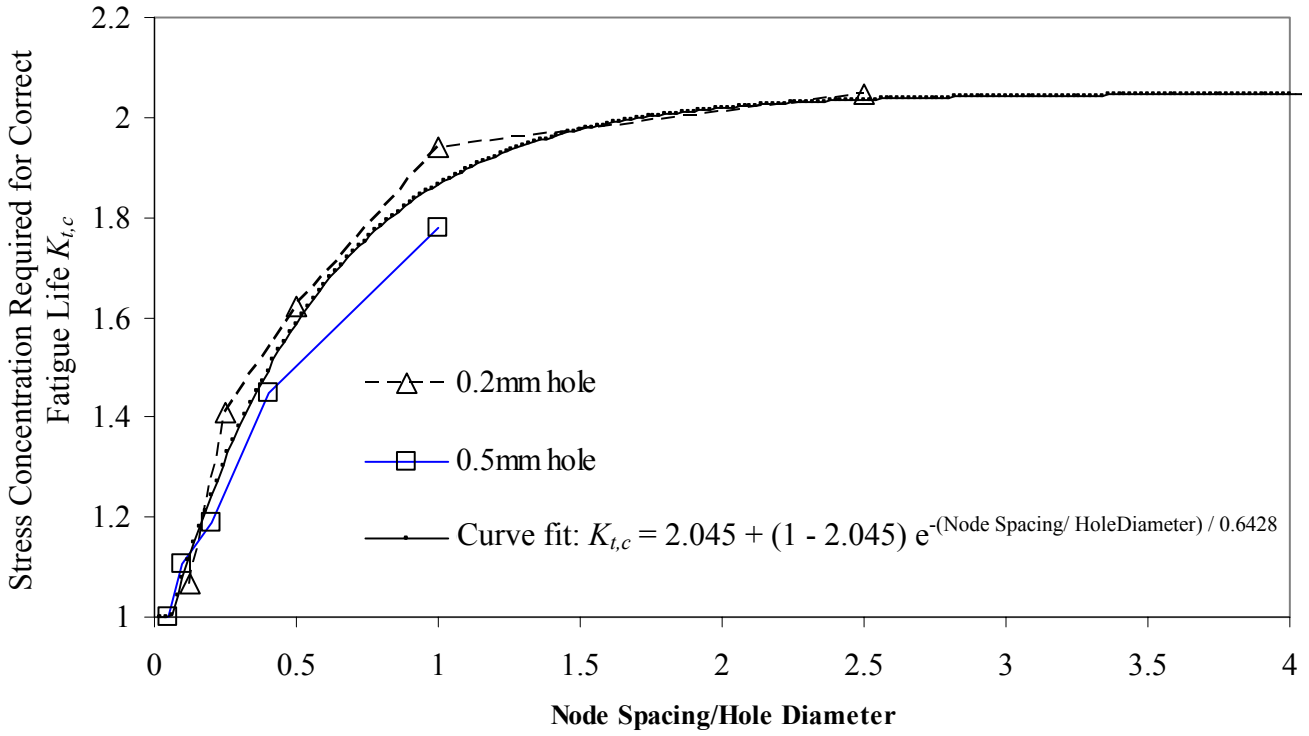

Fig. 23 — Stress concentration $K_{t,c}$ required to achieve correct fatigue life at five nodes spacing to hole diameter ratios for 0.2 and 0.5 mm spherical holes modeled using porosity field.

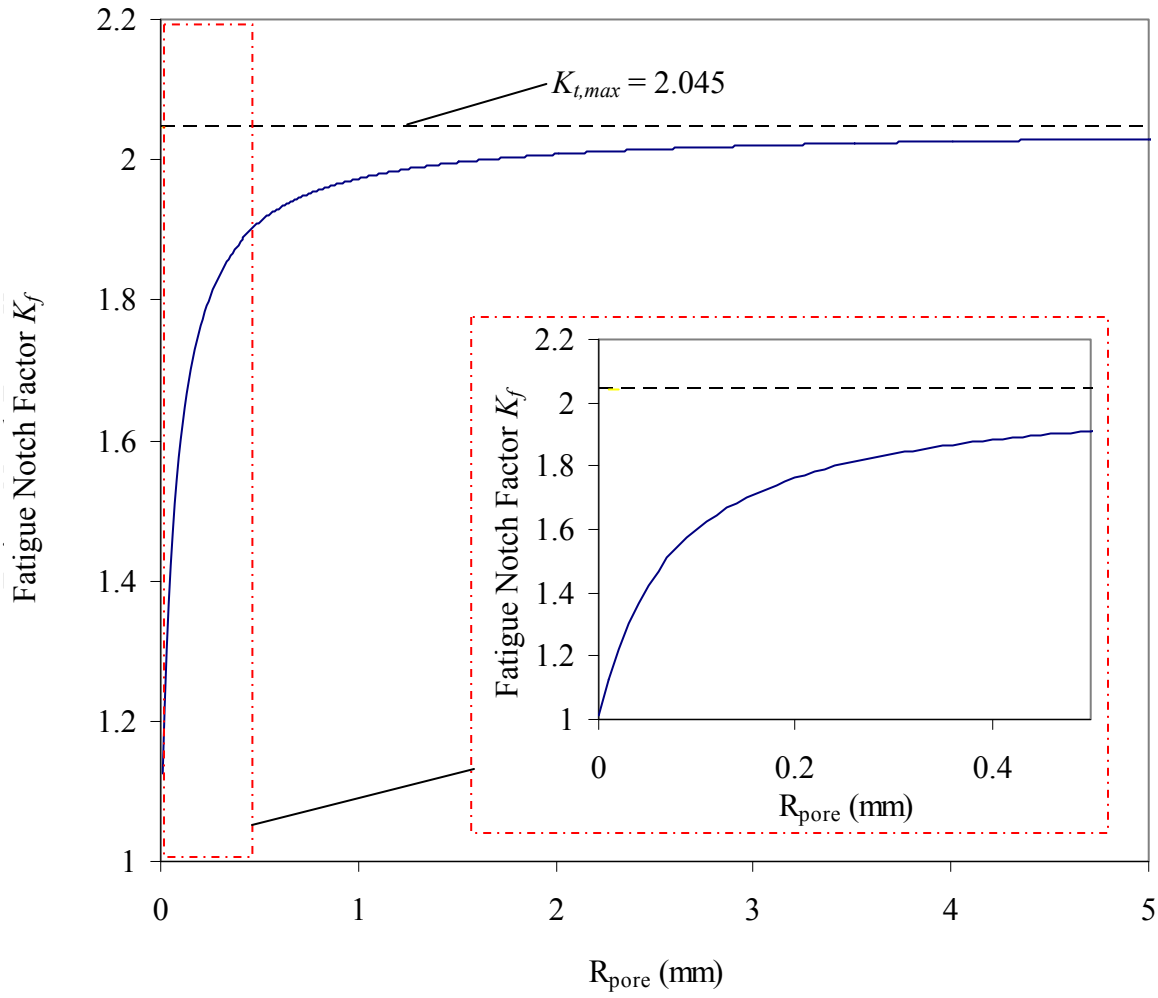

Fig. 24 — Fatigue notch factor K_f from Equ. 9 for S_u = 1144 MPa with $K_{t,max}$ = 2.045.

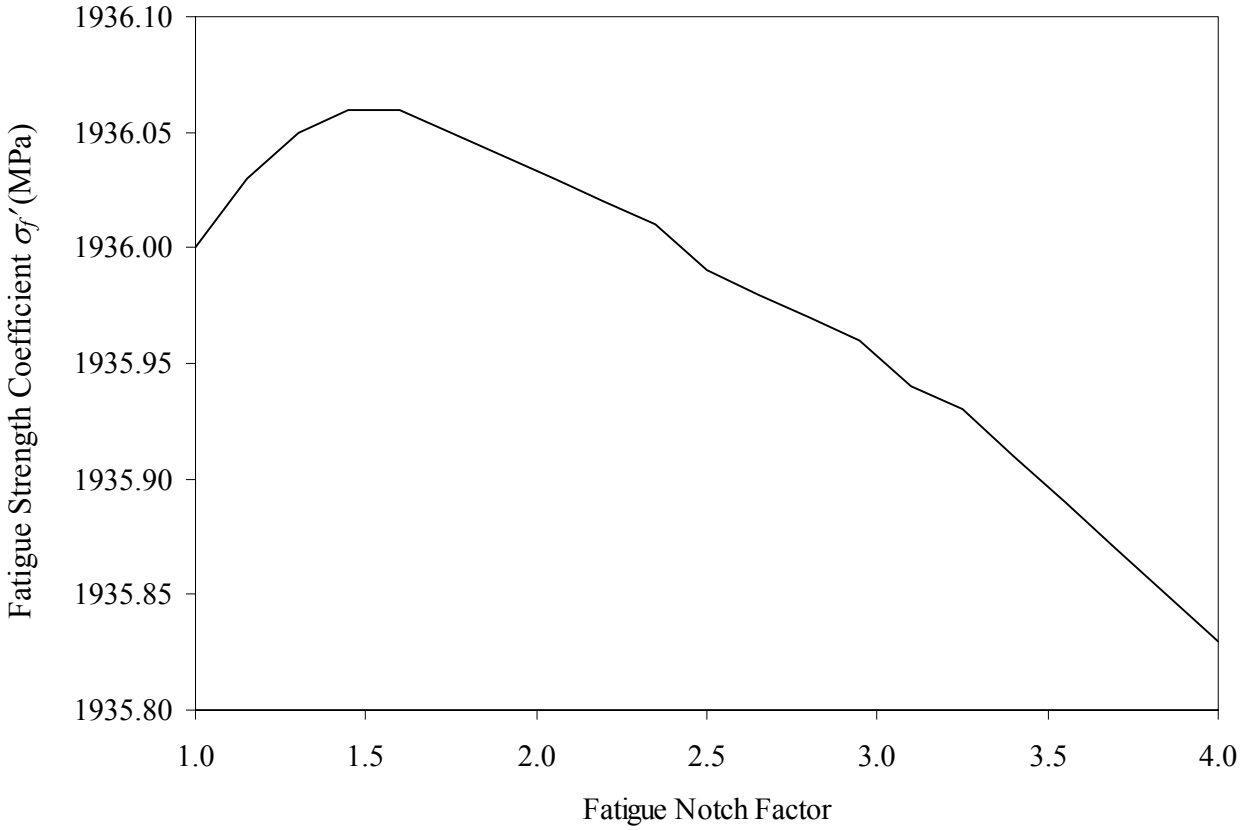

Fig. 25 — Fatigue strength coefficient σ_f' versus corresponding fatigue notch factor to give identical solutions to the strain-life equations along with other three fatigue properties at the same notch factor.

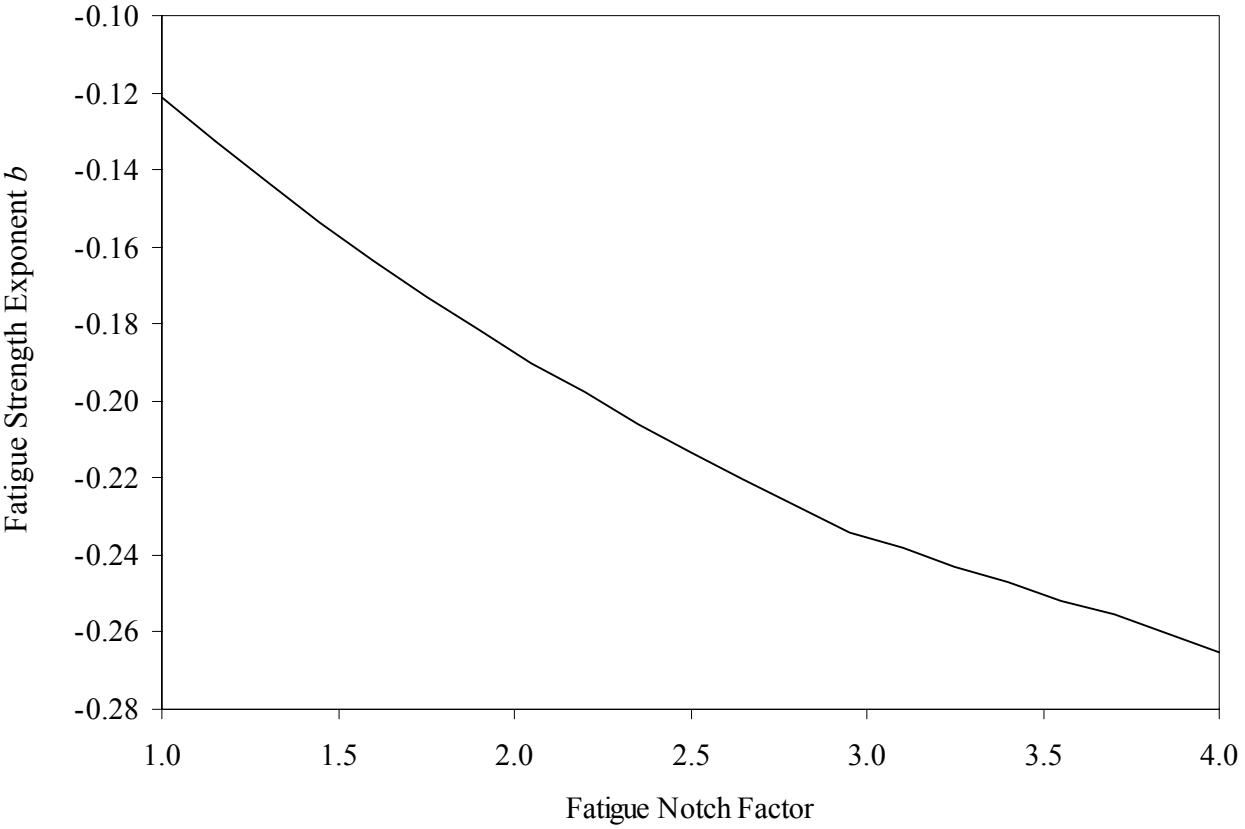

Fig. 26 — Fatigue strength exponent b versus corresponding fatigue notch factor to give identical solutions to the strain-life equations along with other three fatigue properties at the same notch factor.

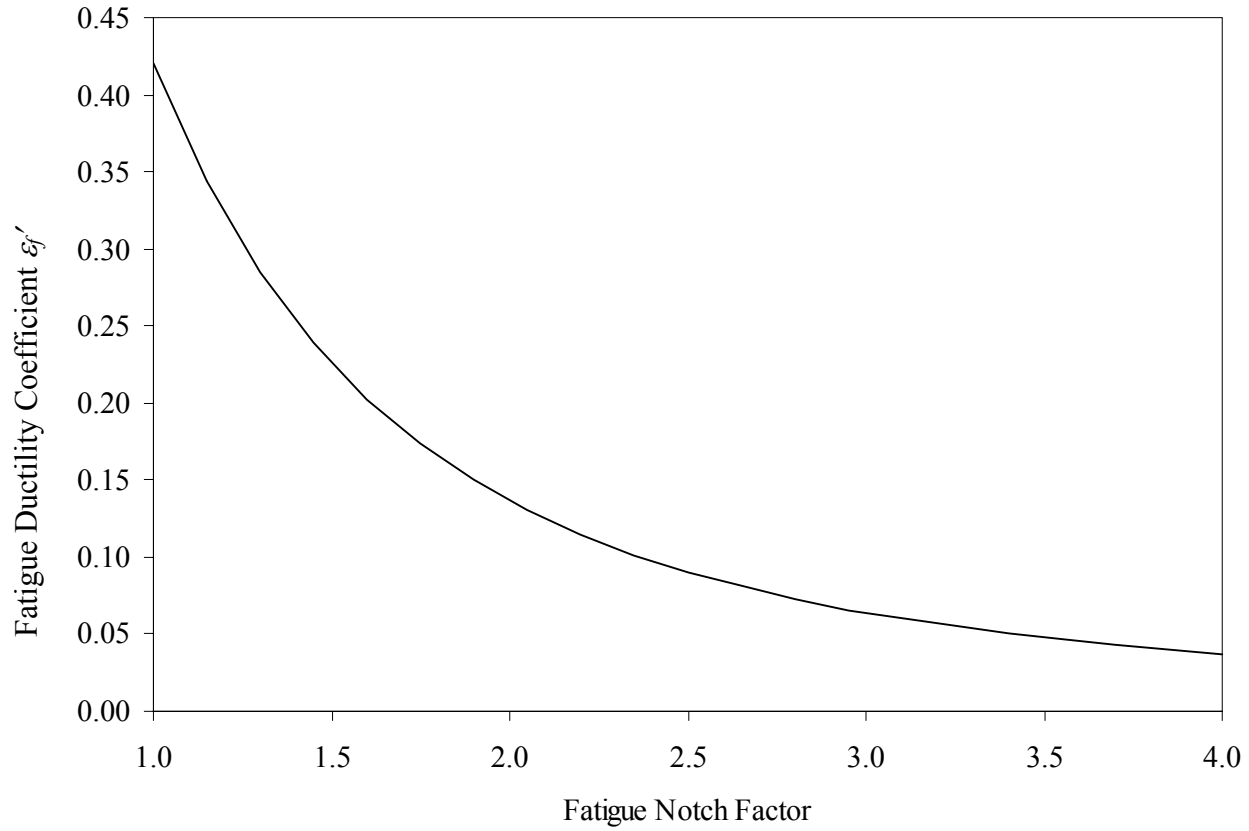

Fig. 27 — Fatigue ductility coefficient ε_f' versus corresponding fatigue notch factor which give identical solutions to the strain-life equations along with other three fatigue properties at the same notch factor.

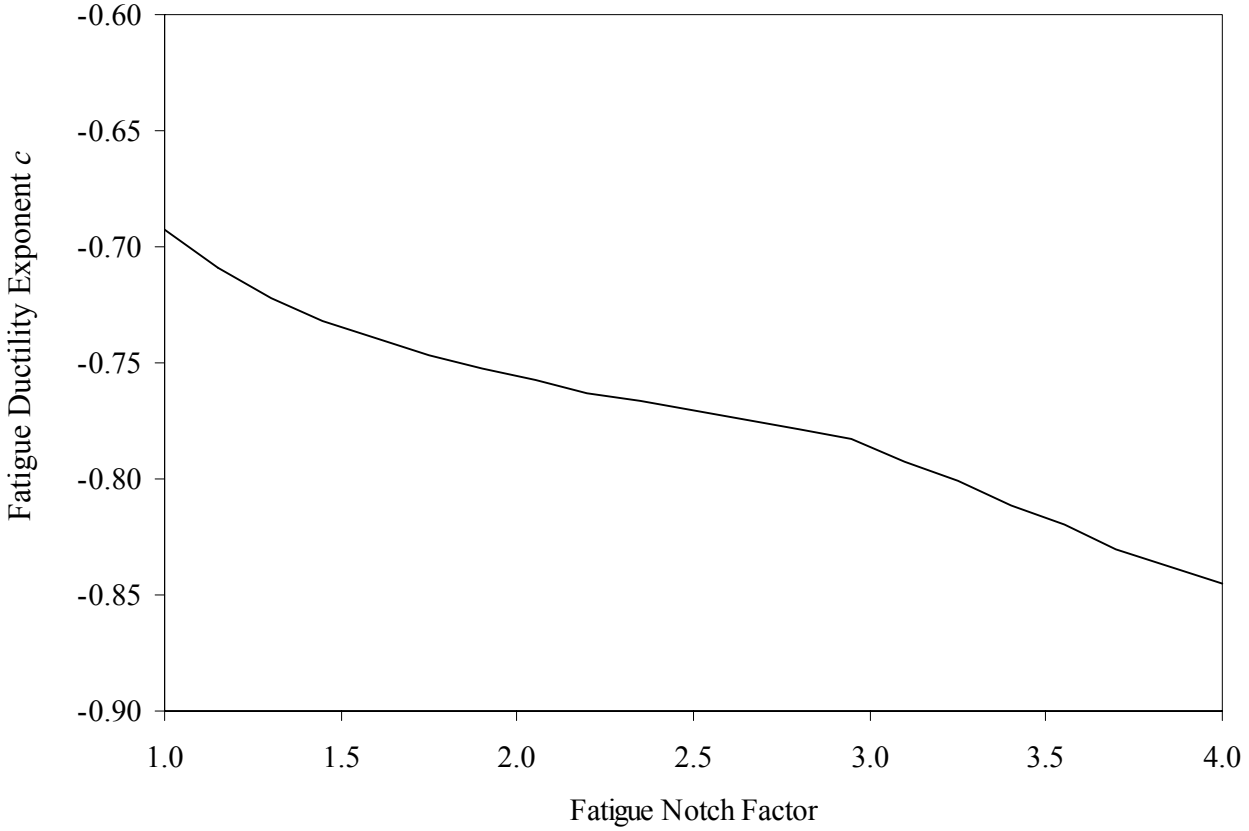

Fig. 28 — Fatigue ductility exponent c versus corresponding fatigue notch factor which give identical solutions to the strain-life equations along with other three fatigue properties at the same notch factor.

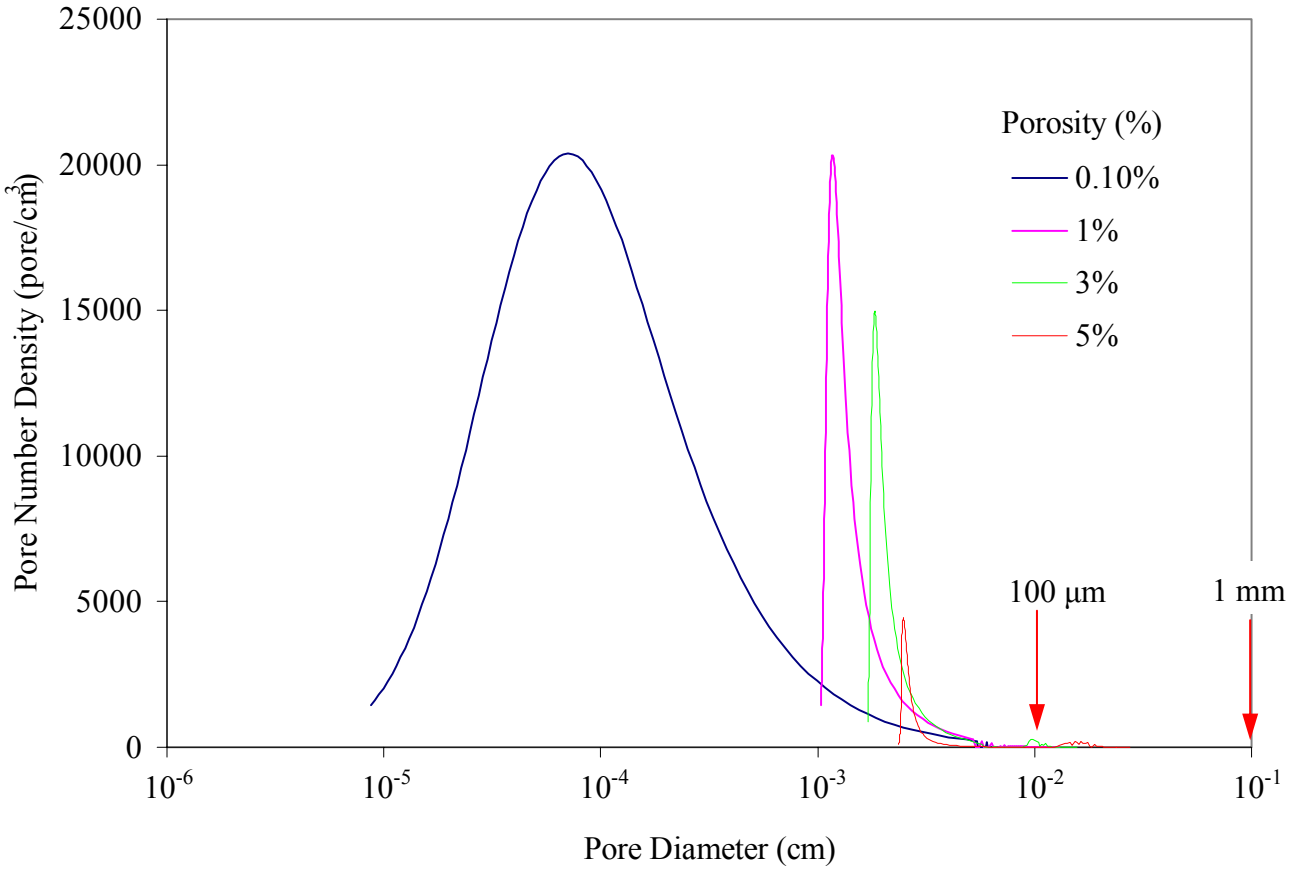

Fig. 29 — Pore number density distributions at the start of porosity formation (0.1 %), and at 1%, 3% and 5% porosity. Number density decreases as pores grow and merge together into larger pores.

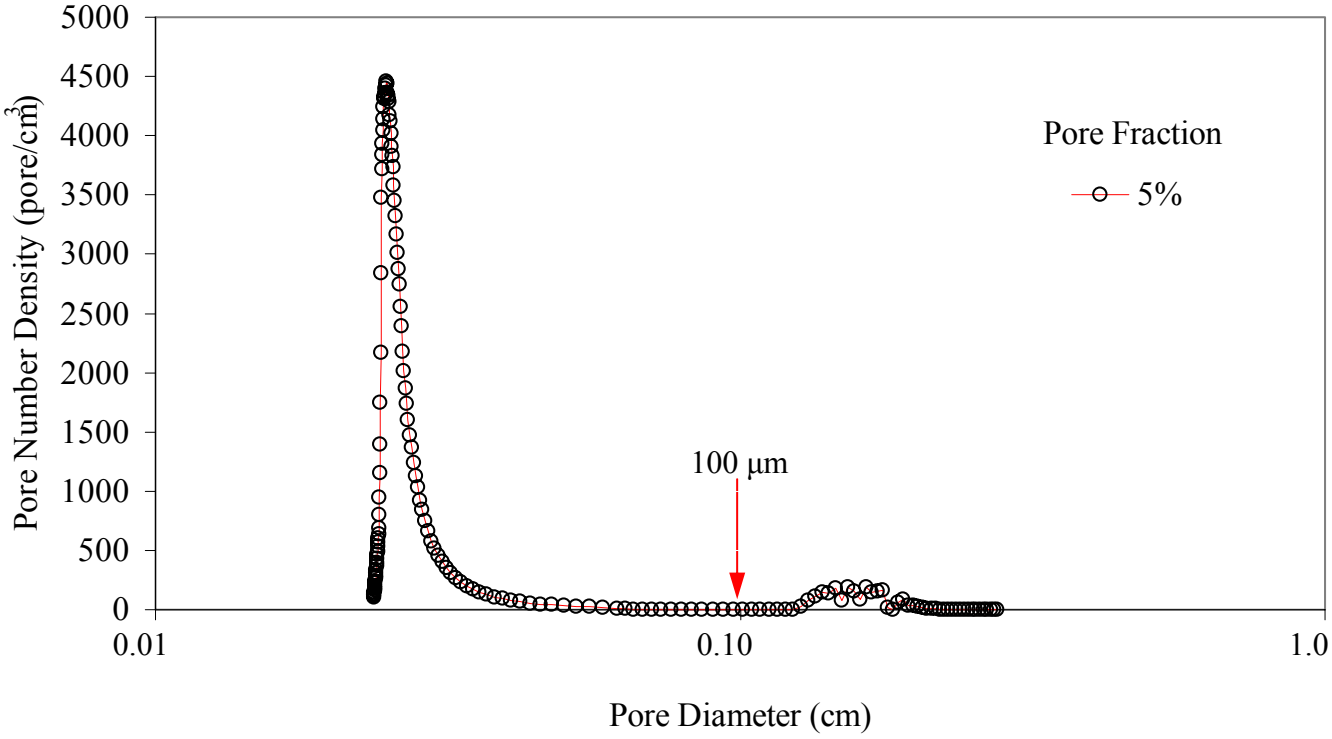

Fig. 30 — Pore number density distribution at 5% porosity. Merged pores begin to form a second distribution of merged pores at about 200 µm.

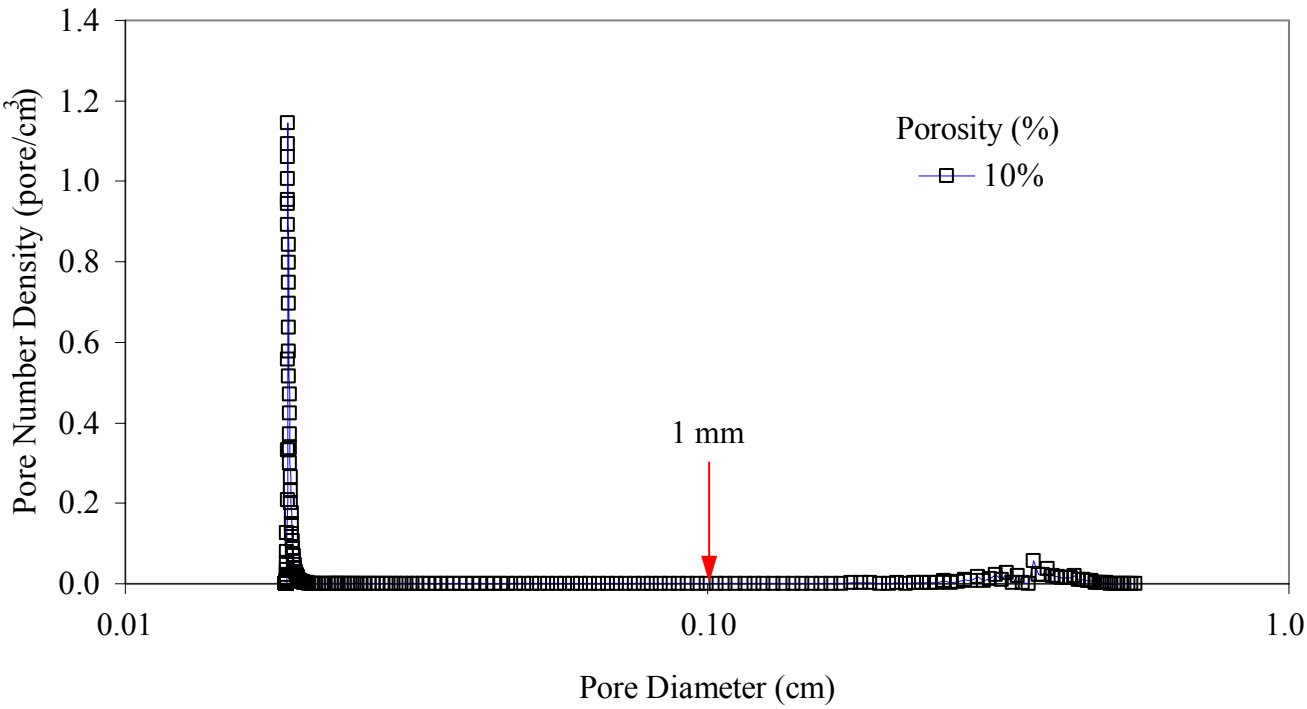

Fig. 31 — Pore number density distributions at 10% porosity. Maximum pore sizes are now on the order of several mm in diameter.

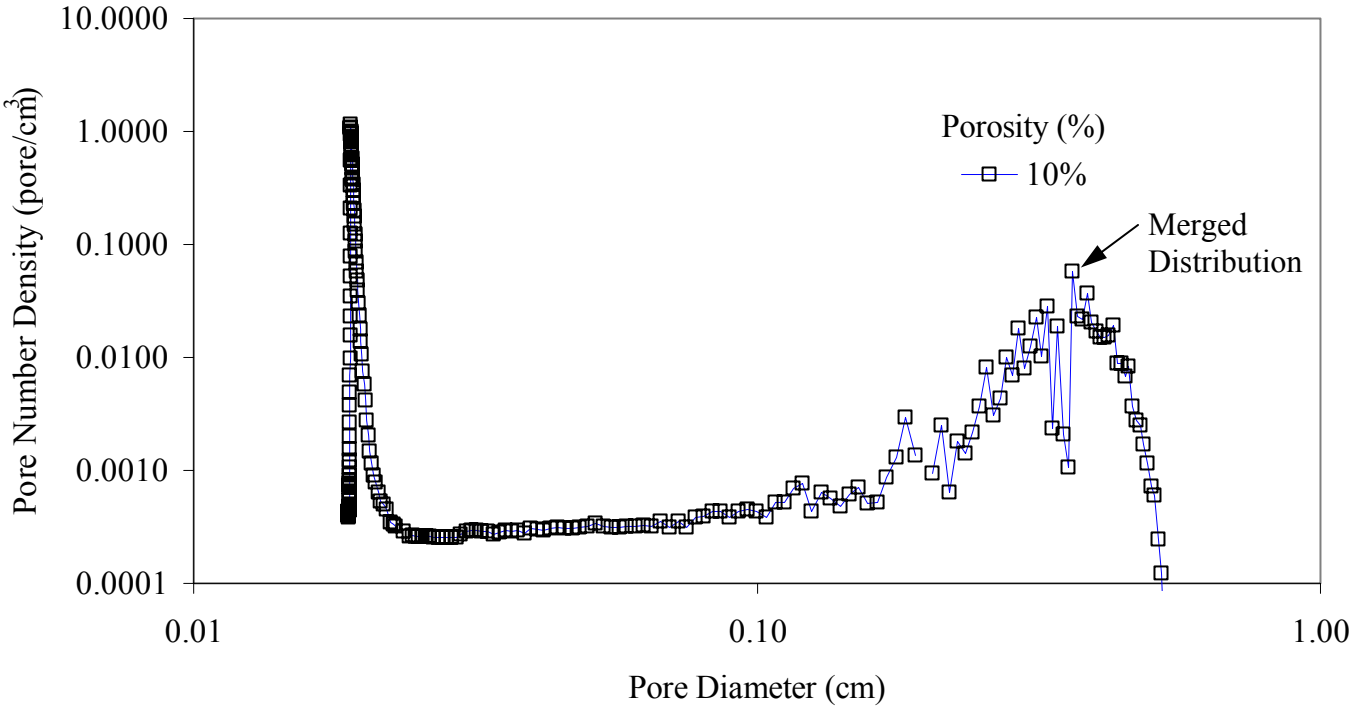

Fig. 32 — Pore number density distributions at 10% porosity with number density plotted on log scale to visualize the merged pore distribution with pore sizes of several mm in diameter.

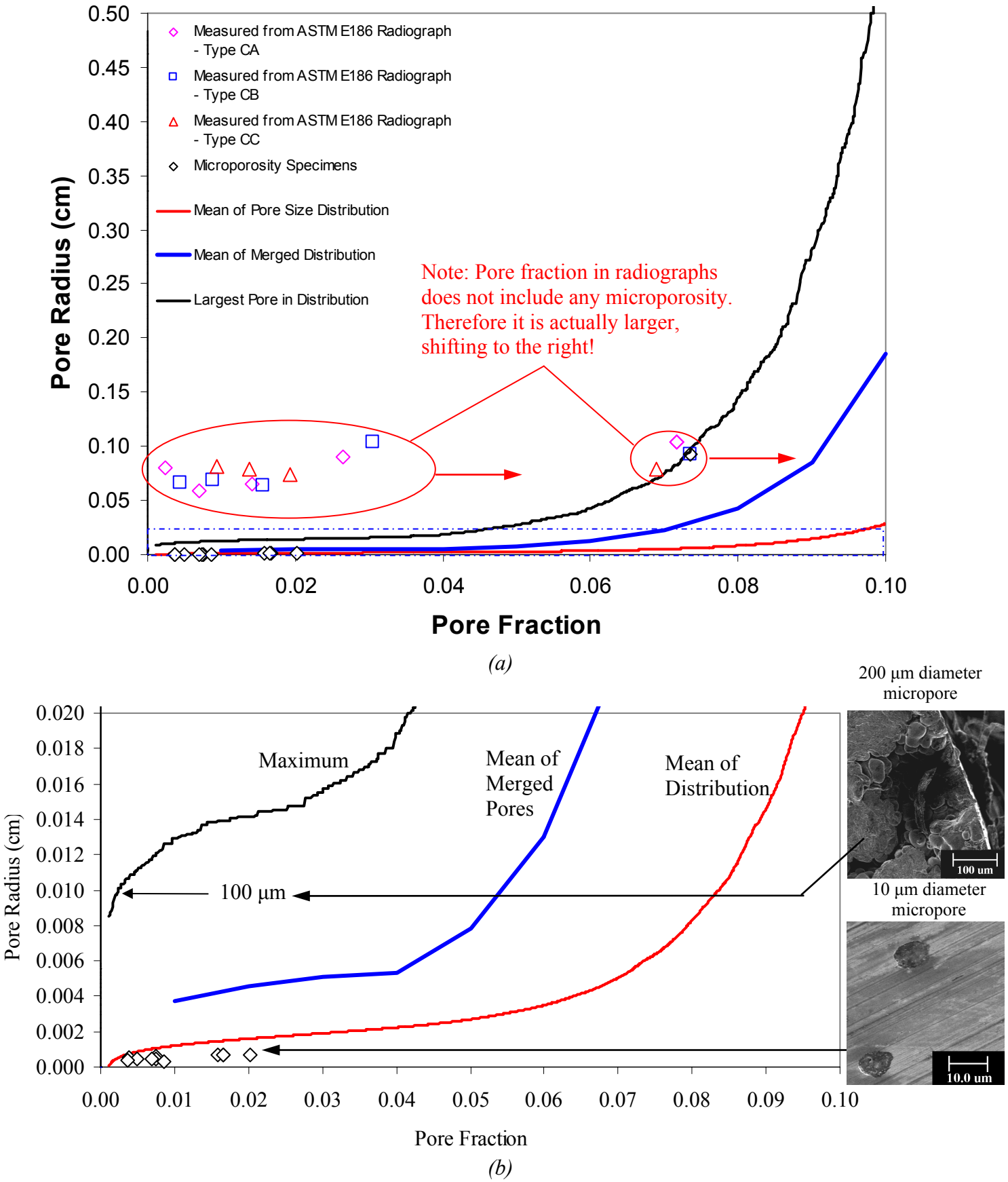

Fig. 33 — *(a)* Pore size distribution model results (maximum, mean of the merged pores and mean of entire distribution) compared with pore size measurements from ASTM radiographic analysis [30] and cut-surfaces of radiographically sound specimens with microporosity and *(b)* comparison with micro only.

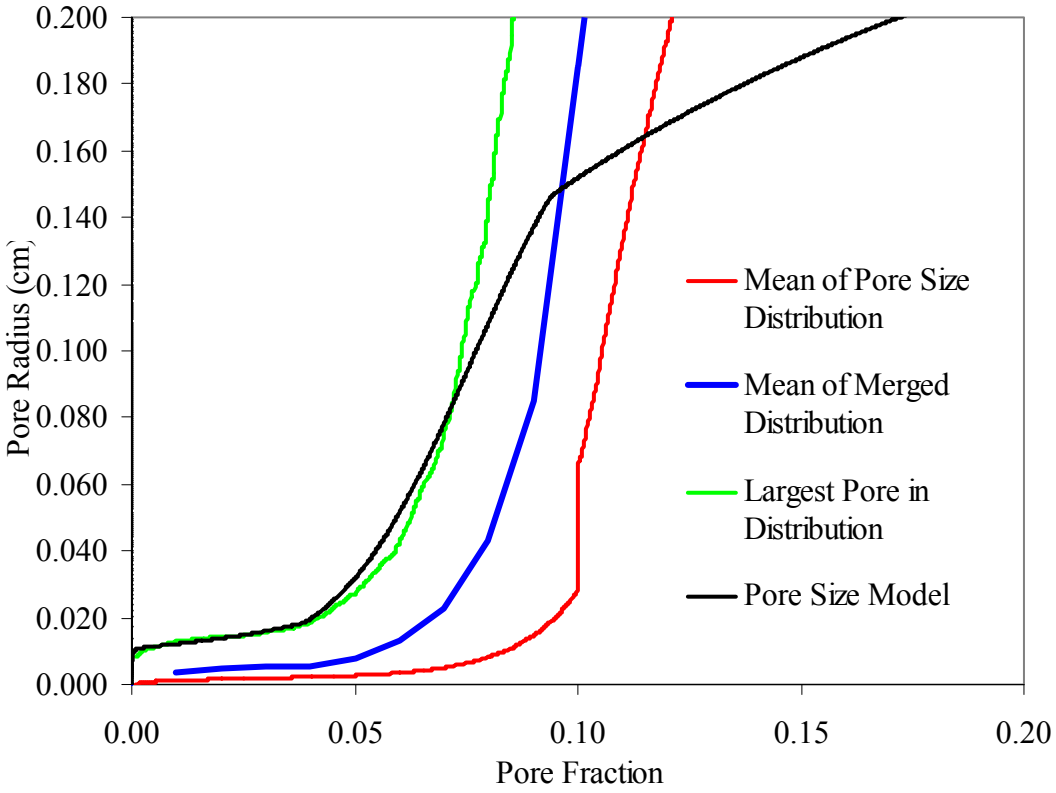

Fig. 34 — Comparison of pore size model used in subgrid fatigue model to pore size distribution model results.

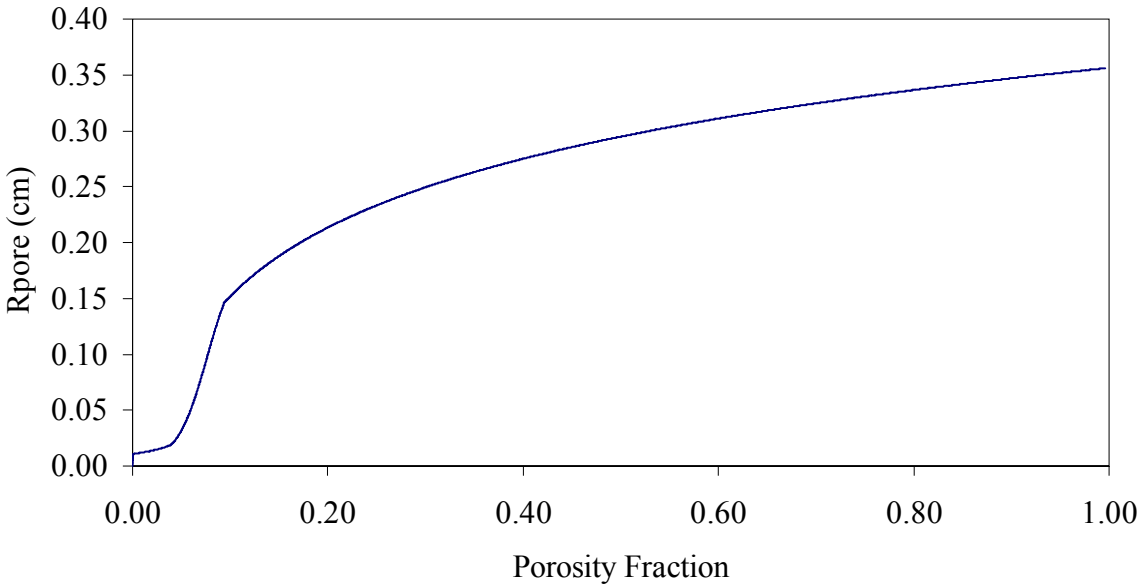

Fig. 35 — Entire pore size model curve used in subgrid fatigue model.

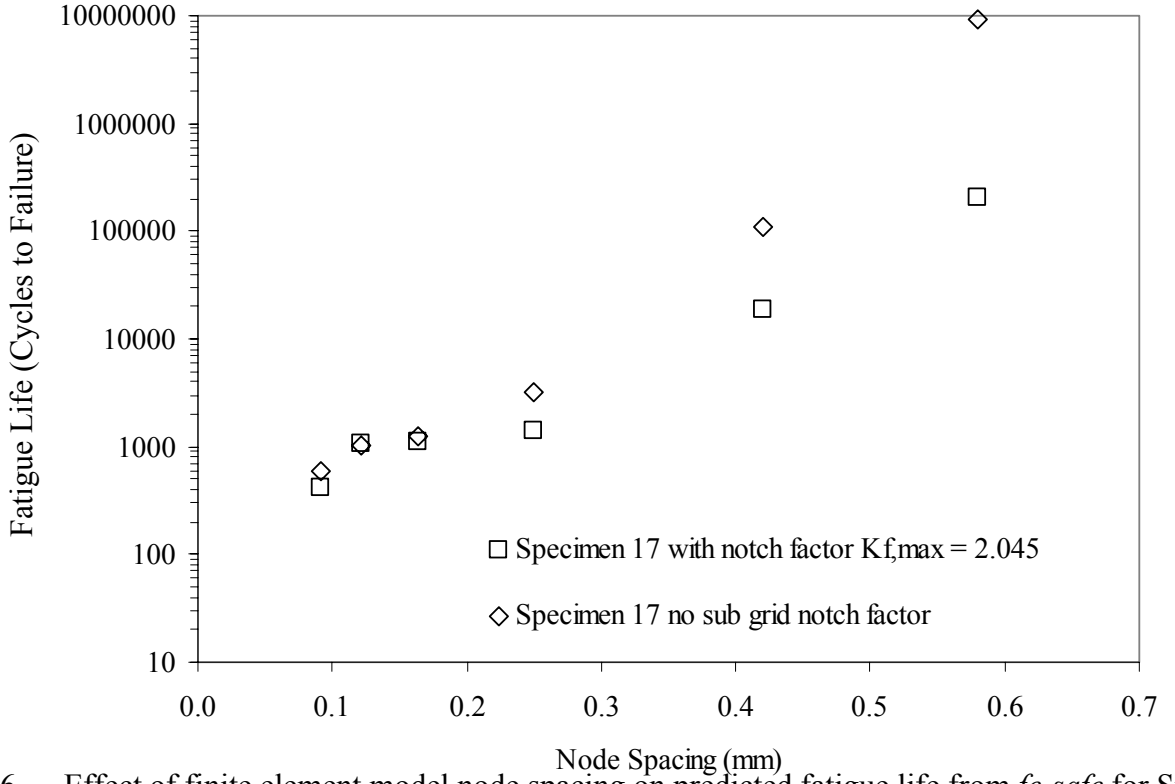

Fig. 36 — Effect of finite element model node spacing on predicted fatigue life from *fe-safe* for Specimen 17; original method without subgrid fatigue model, and with subgrid model with $K_{f,max} = 2.045$.

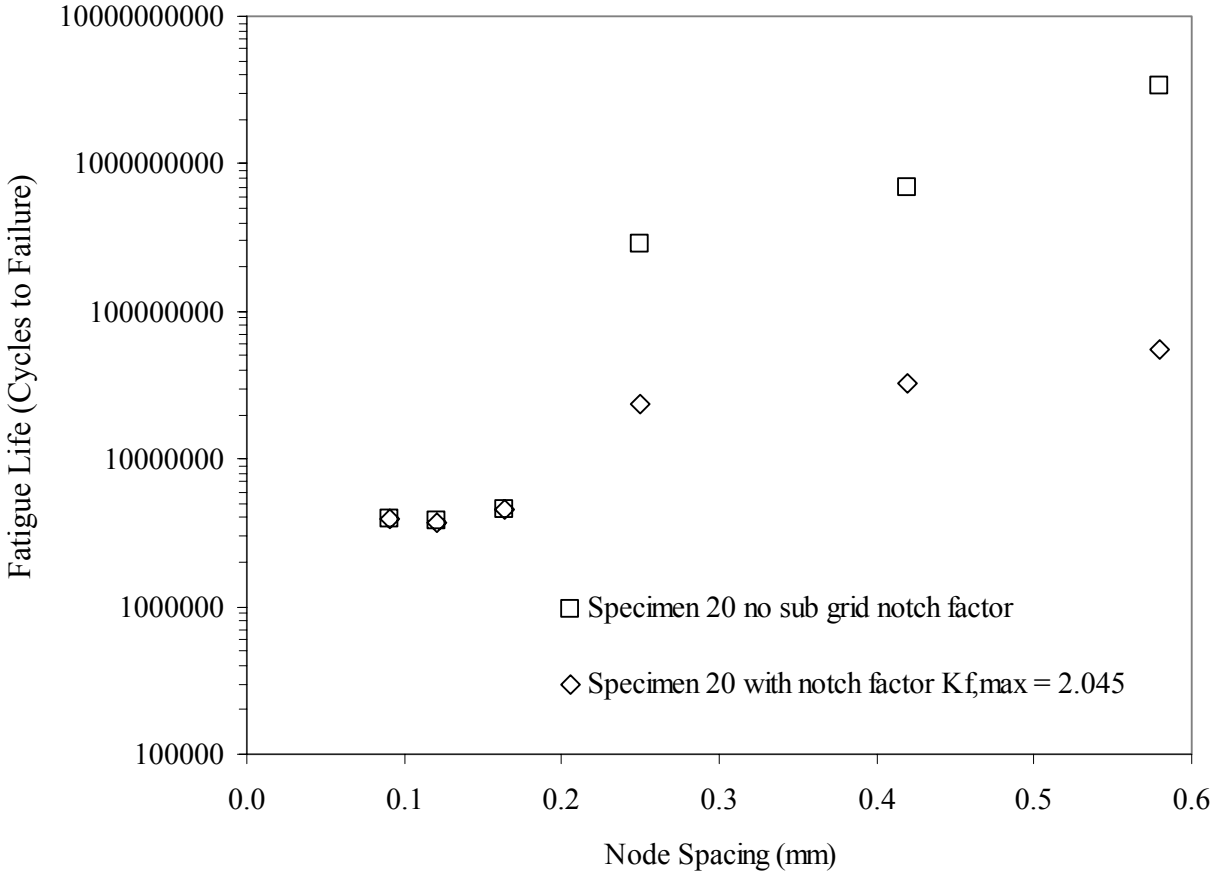

Fig. 37 — Effect of finite element model node spacing on predicted fatigue life from *fe-safe* for Specimen 20; original method without subgrid fatigue model, and with subgrid model with $K_{f,max} = 2.045$. There is vast improvement at 0.25 mm node spacing and larger.

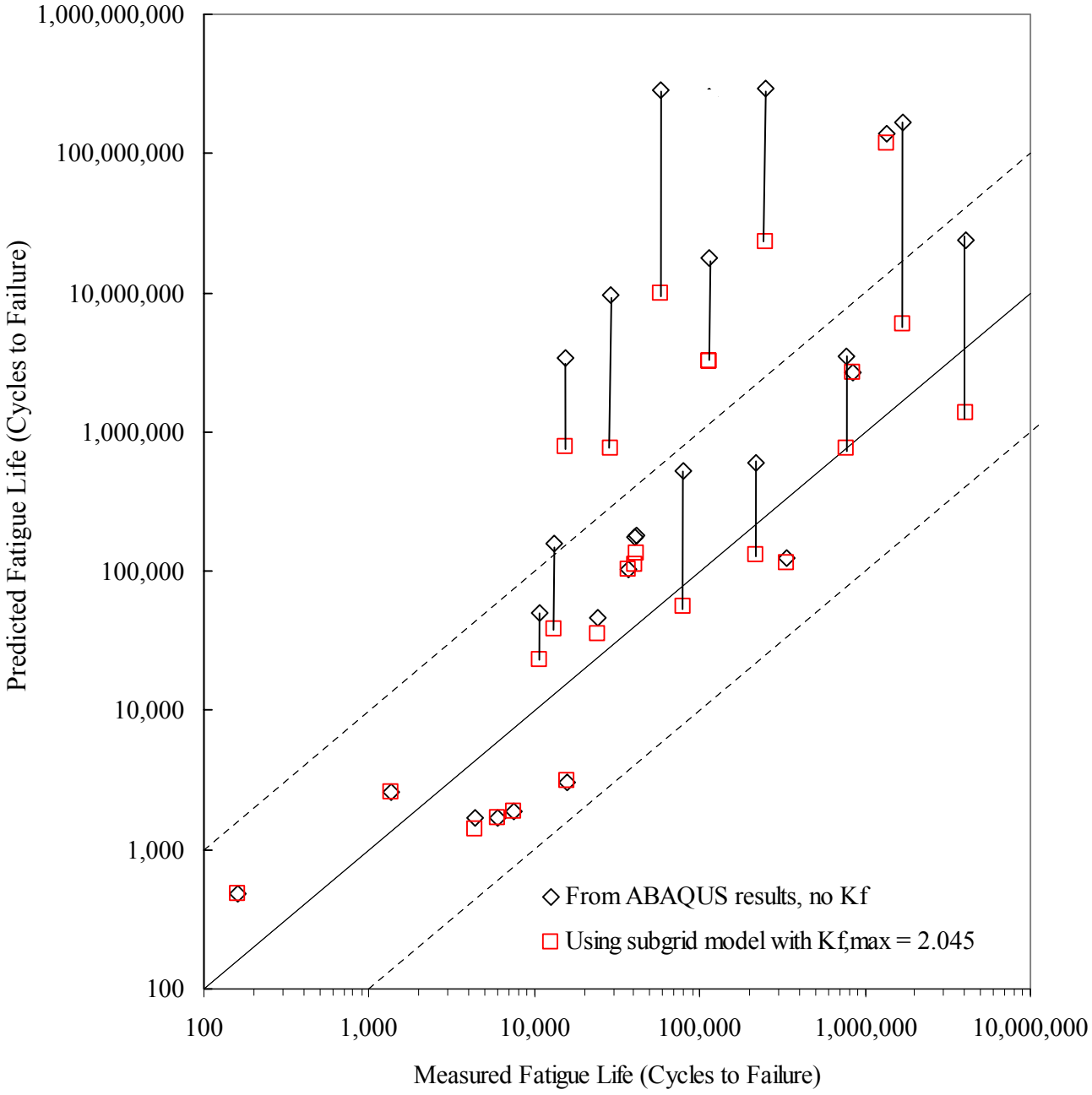

Fig. 38 — Comparison between measured and predicted fatigue lives of specimens for node spacing ≈ 0.25 mm for original method (no K_f) and for the subgrid fatigue model with $K_{f,max} = 2.045$. Prediction uses ABAQUS simulated stress field, and subgrid fatigue model with fatigue properties dependent on K_f as shown in Figures 25 through 28. Multi-axial Brown-Miller algorithm with Morrow mean stress correction is used in *fe-safe*. Predicted life is taken as the smallest life in the *fe-safe* calculation.

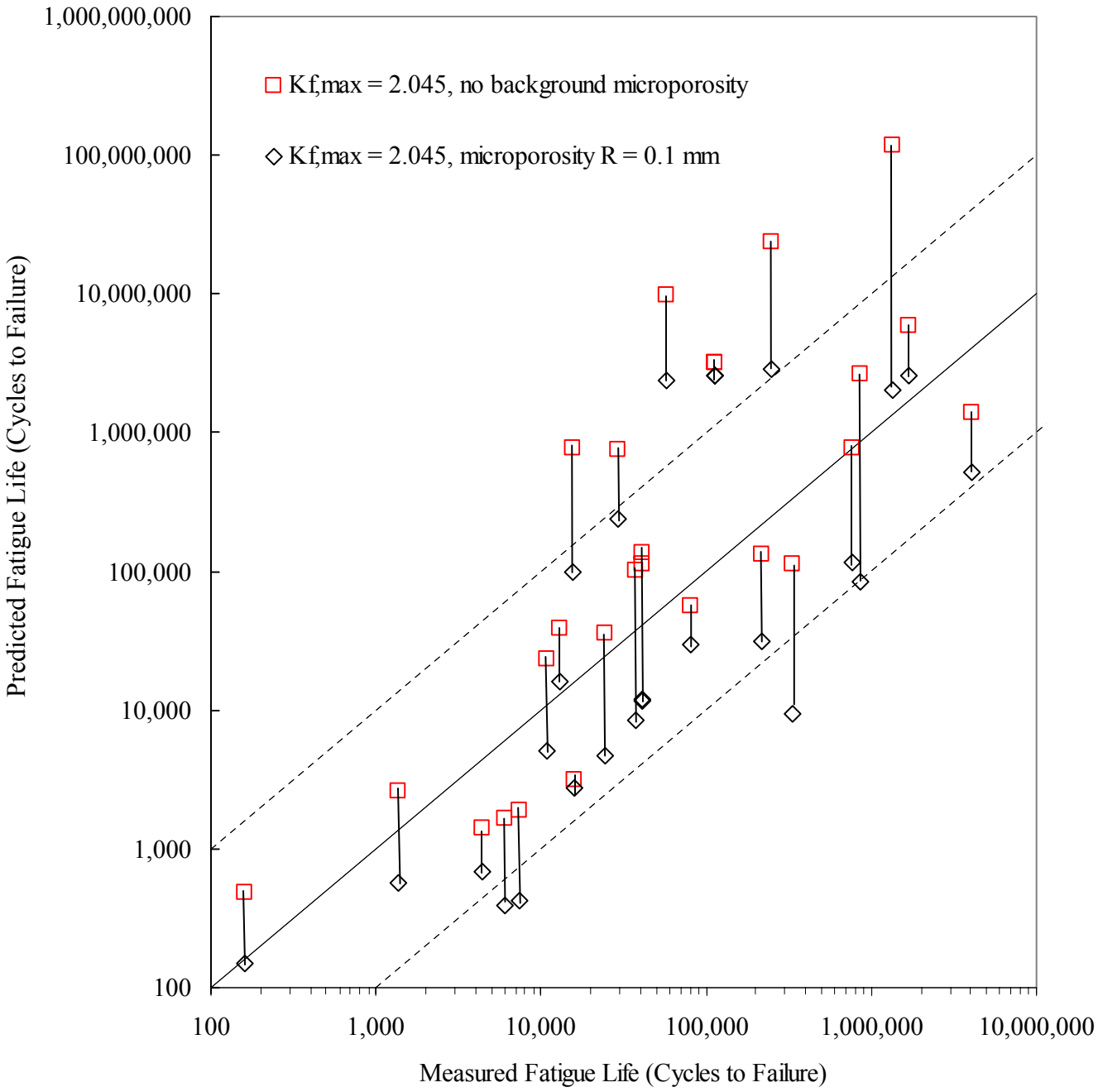

Fig. 39 — Comparison between measured and predicted fatigue lives of specimens for node spacing ≈ 0.25 mm for the subgrid fatigue model with $K_{f,max}$ = 2.045 (higher values), and the same model but using a uniform background pore size no smaller than 100 μm radius (i.e. even at nodes where tomography gives material as 100% sound). Otherwise, conditions are the same as in Figure 38.

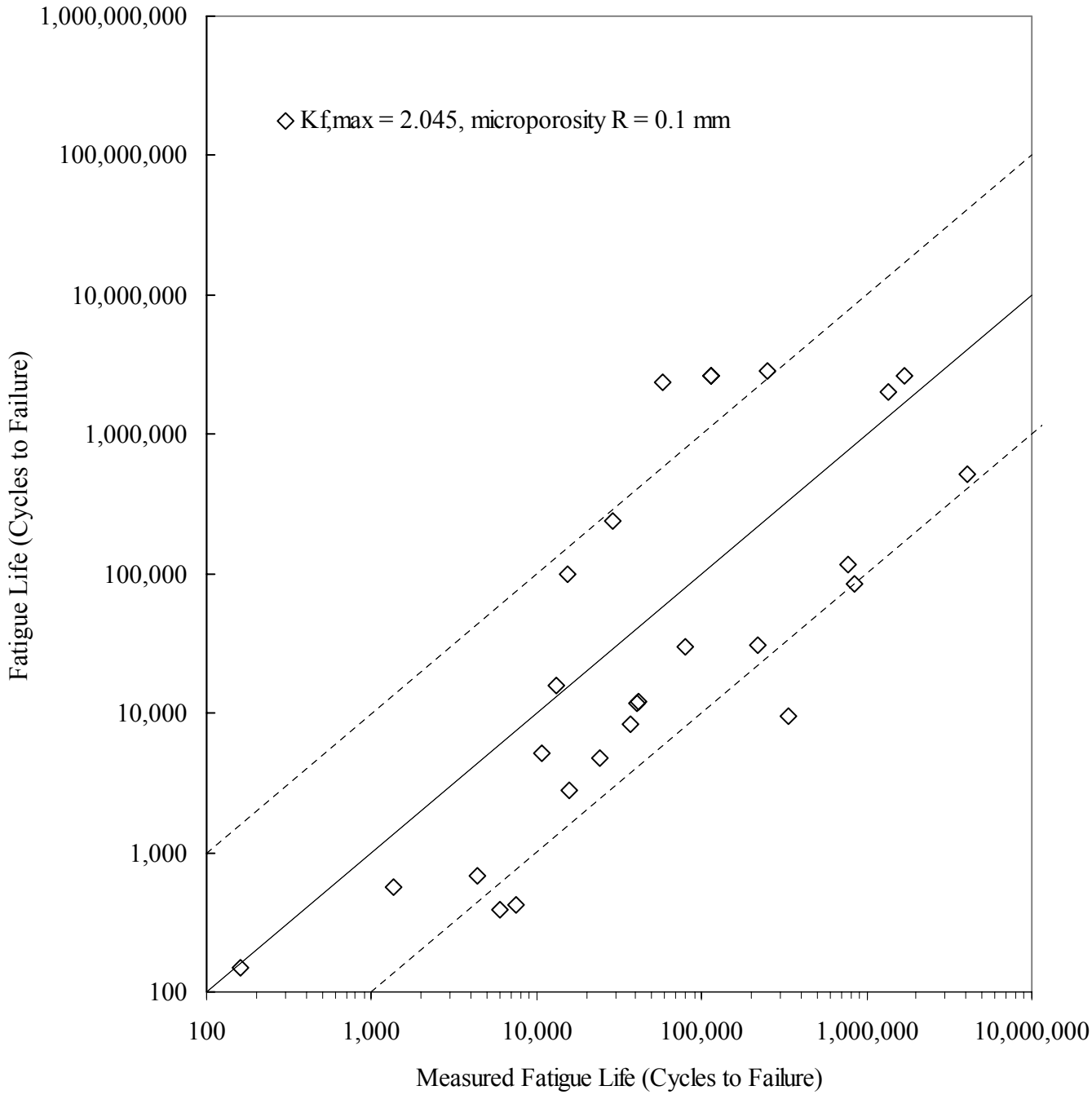

Fig. 40 — Comparison between measured and predicted fatigue lives of specimens for node spacing ≈ 0.25 mm for final model giving the best agreement. Results are repeated from Figure 39, but provided alone for clarity. A uniform background pore size no smaller than 100 μm radius is used everywhere (even at sound nodes), when pore size model gives larger value of radius the larger value is used.

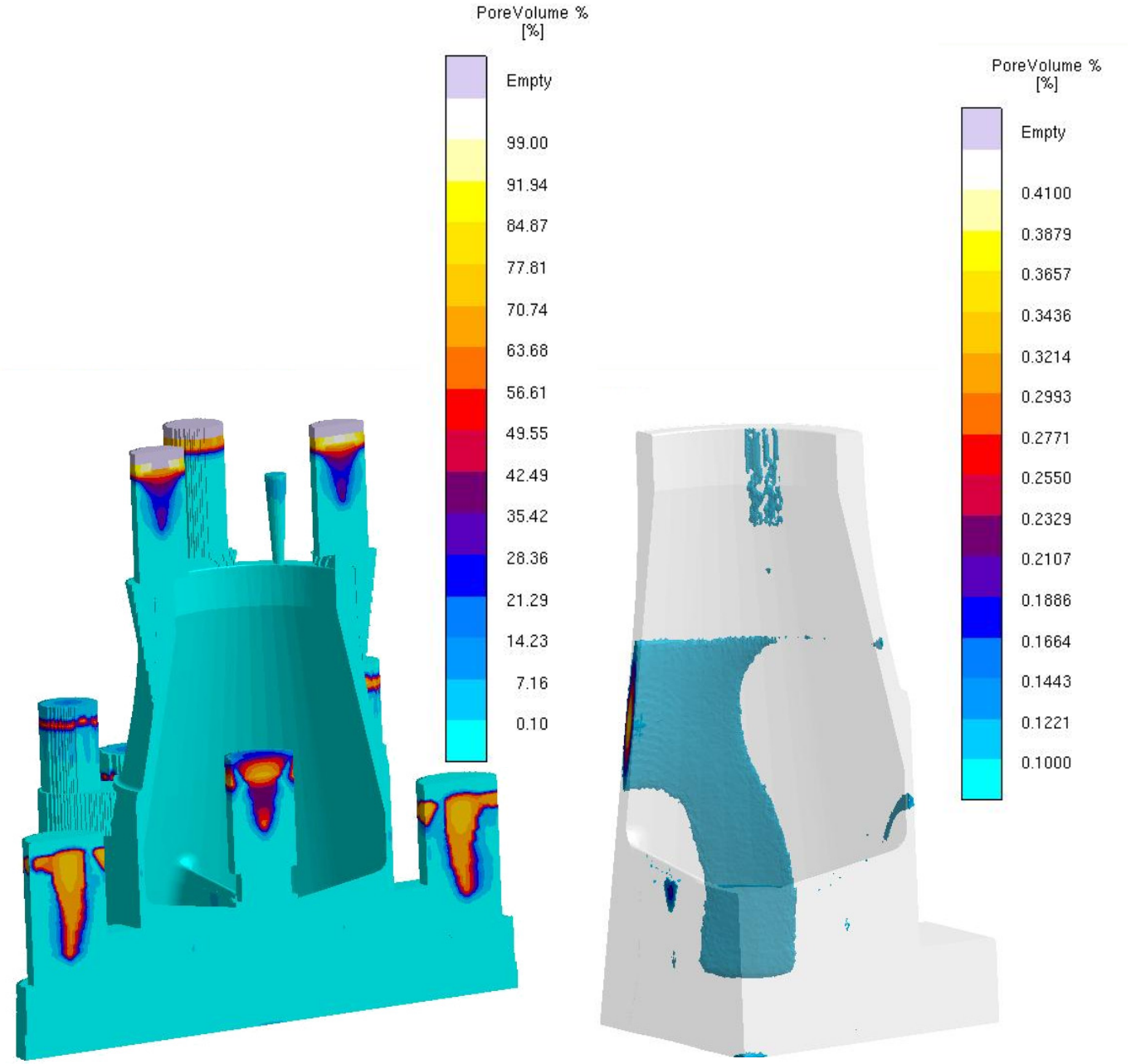

(a) *(b)*

Fig. 41 — Porosity prediction from the advanced porosity module in MAGMAsoft. Macroporosity is predicted in the risers in *(a)* and at two small locations of riser contacts on the casting surface. The x-ray view of the casting only in *(b)* shows locations of dispersed microporosity in the nozzle wall, and in the vanes.

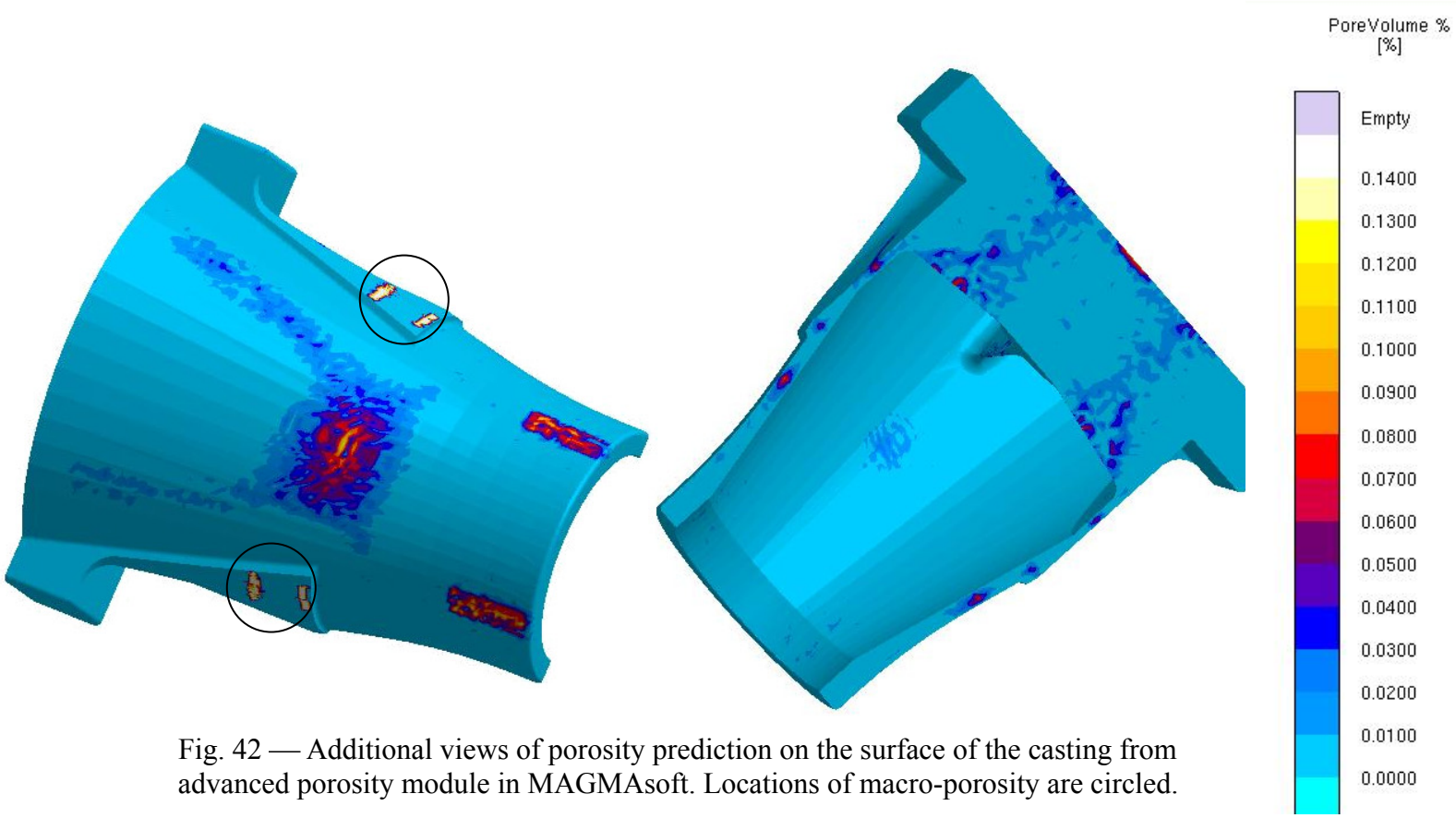

Fig. 42 — Additional views of porosity prediction on the surface of the casting from advanced porosity module in MAGMAsoft. Locations of macro-porosity are circled.

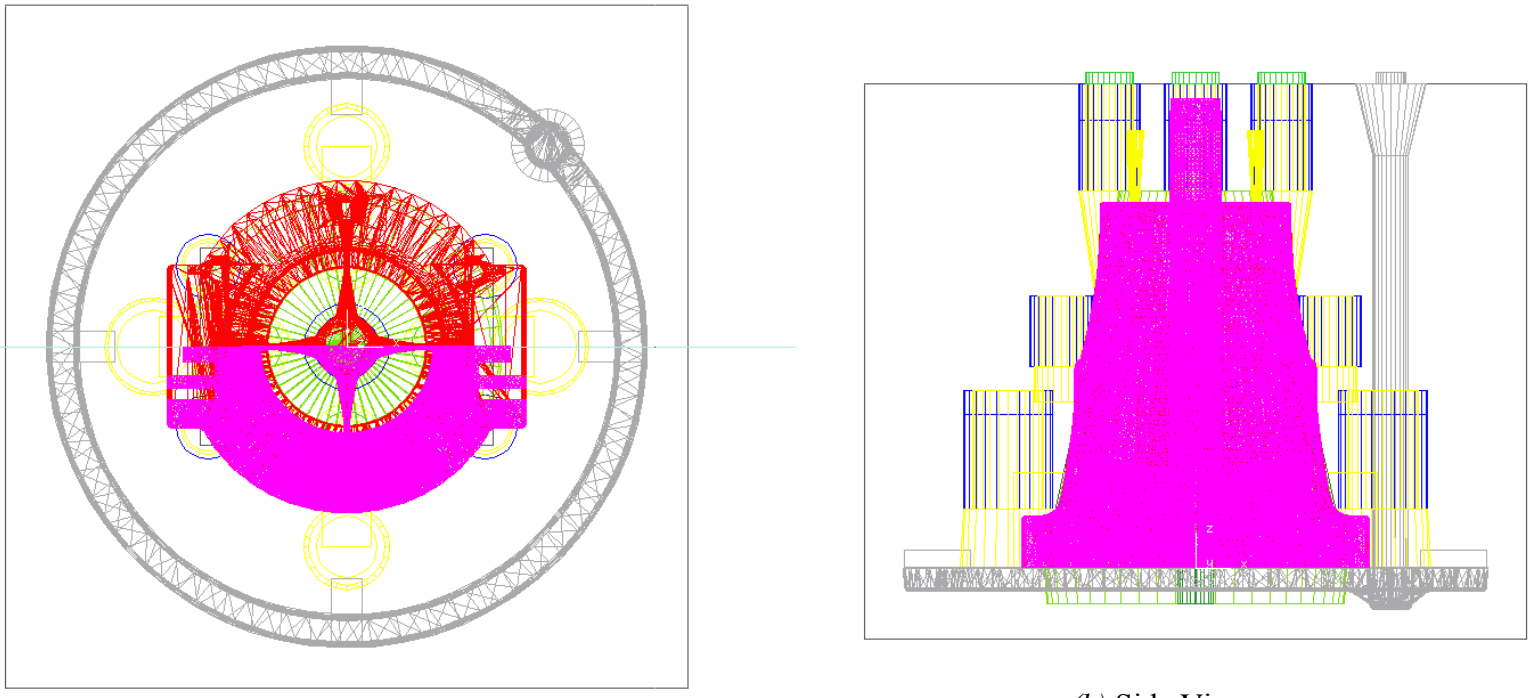

(a) Top View

(b) Side View

Fig. 43 — Top and side views of correctly positioned (after rotation and translation) finite element mesh (shown in magenta) brought into the MAGMAlink program as an ABAQUS FEA mesh input (inp) file.

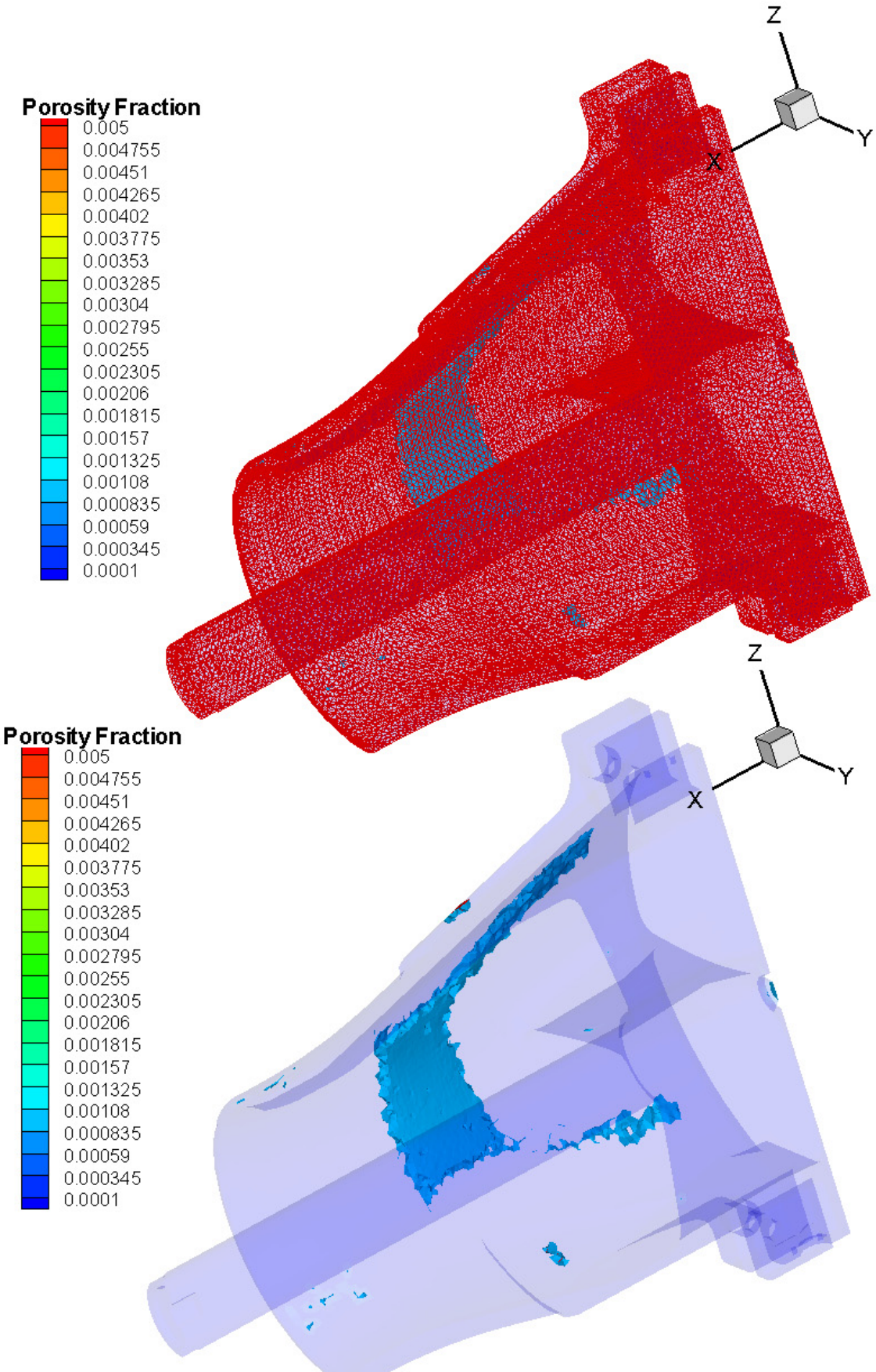

Fig. 44 — Porosity field from MAGMAsoft advanced porosity module transferred to FEA mesh. FEA mesh shown above and x-ray view shown below. Note that porosity filed has to be converted from % to pore fraction before performing calculations in ABAQUS and *fe-safe*.

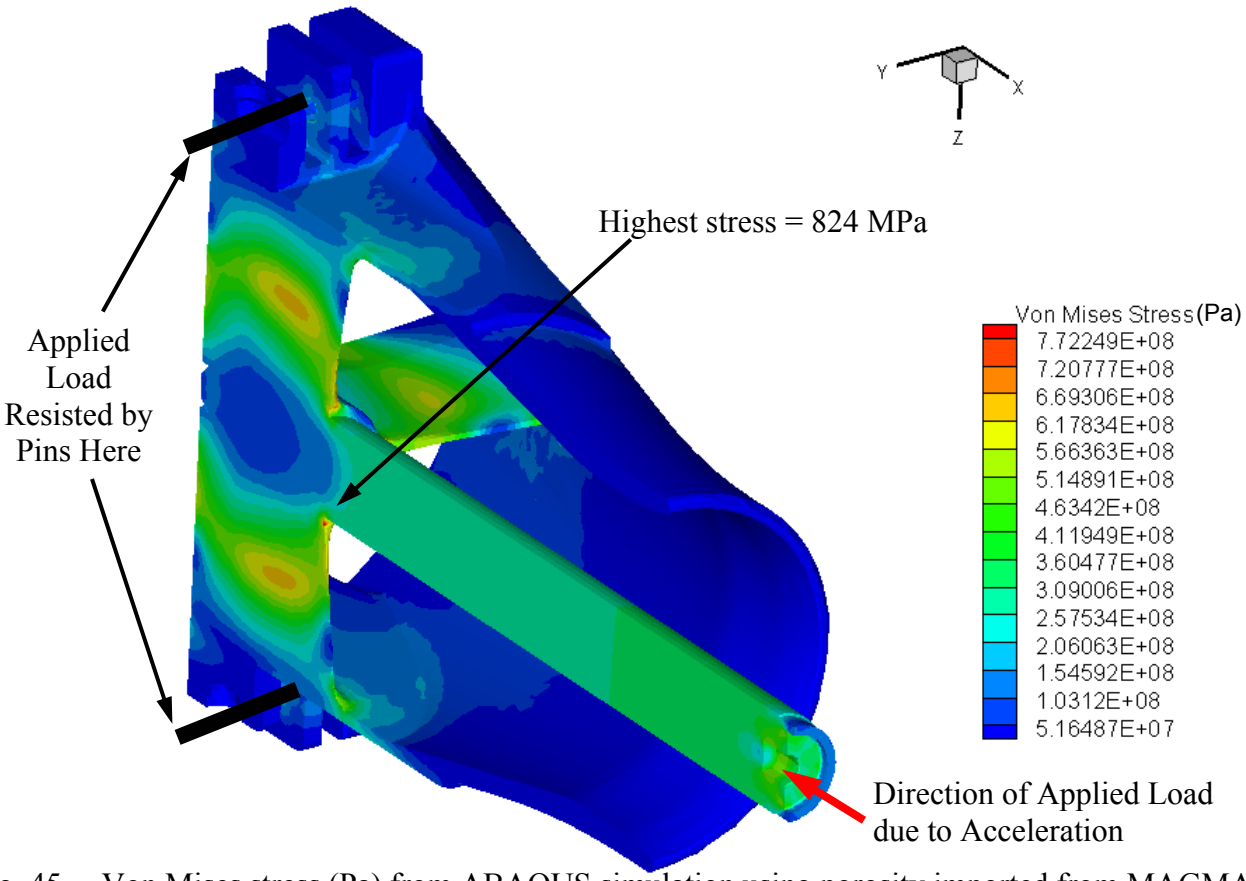

Fig. 45 —Von Mises stress (Pa) from ABAQUS simulation using porosity imported from MAGMAsoft with elastic properties dependent on porosity. No appreciable change in stress field observed vs. porosity free model.

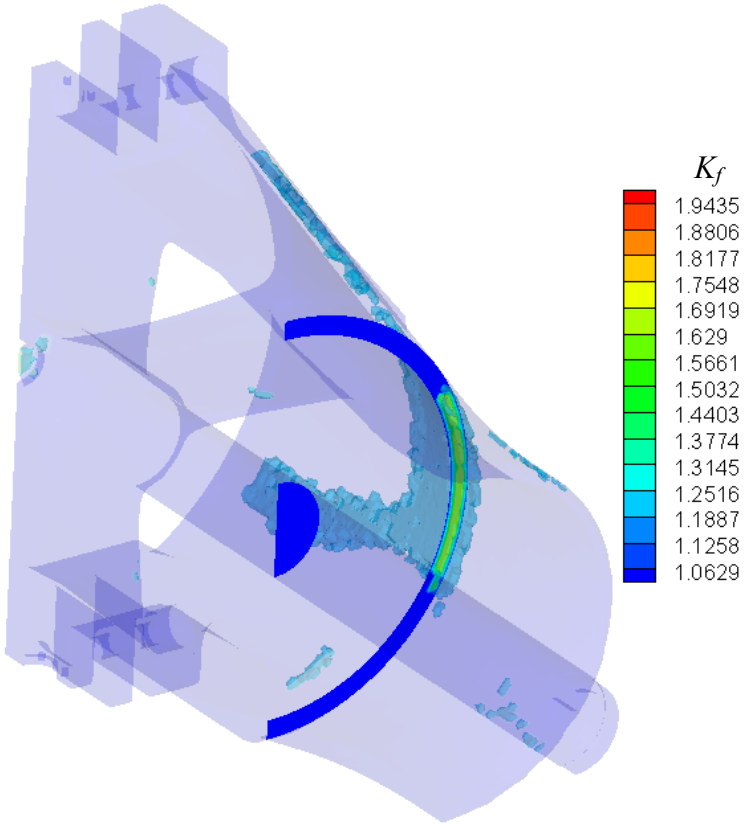

Fig. 46 — Fatigue notch factor data used in *fe-safe* multiaxial strain-life calculations.

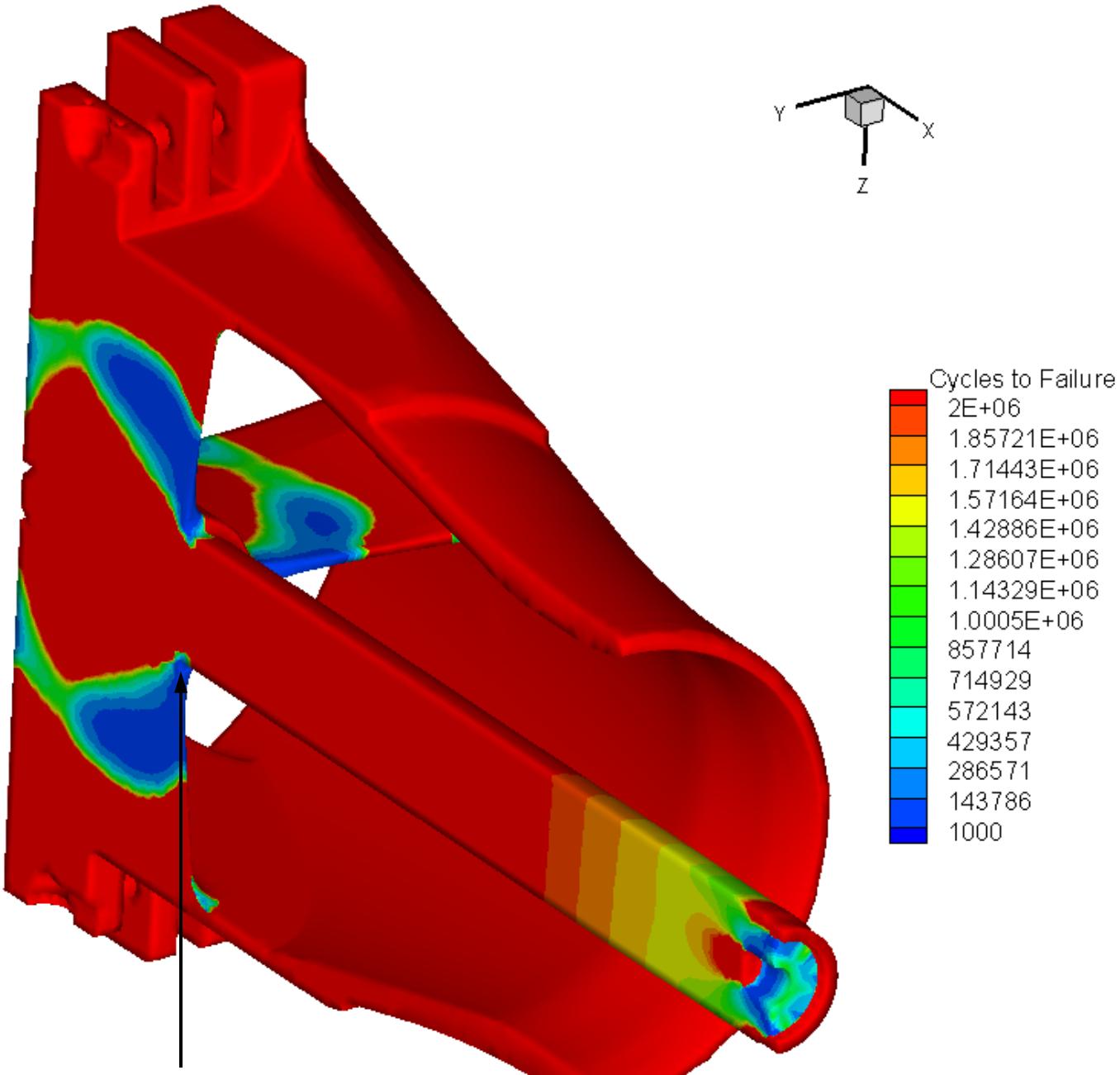

Fig. 47 — Strain-life fatigue calculations from *fe-safe* using ABAQUS stress results and porosity field imported from MAGMAsoft. Fatigue properties used were for 8630 steel developed from specimens with porosity from AMC project.